UNIVERSITÀ DEGLI STUDI DI PALERMO

Dottorato in Fisica
Dipartimento di Fisica e Chimica
FIS/05

Spectral analysis and orbital evolution of Low mass X-ray Binaries at high inclination

DOTTORE
dott.ssa Carmela Galiano

COORDINATORE
Prof. Antonio Cupane

TUTOR
Prof.ssa Tiziana Di Salvo

CO-TUTOR
Prof. Rosario Iaria

CICLO XXVI
ANNO ACCADEMICO 2016/2017

A tutti coloro che, a vario titolo, mi hanno aiutato a raggiungere questo traguardo

Contents

Abstract

X-Ray binaries are gravitationally bound systems consisting of a compact object that accretes matter from a companion star; they are the most interesting objects of the sky, infact they allow to study the physics of matter in very extreme conditions of density, temperature or magnetic field. So the determination of spectral and temporal properties of X-ray binaries plays an important role in understanding the processes involved in these systems. This project aims to understand the properties of binary systems, at high inclination (*dipping and eclipsing sources*), containing neutron stars weakly magnetized. In the light curves of these systems it is possible to identify a variety of modulations with orbital periodicity that are caused by the high inclination of the orbital plane with respect to the line of sight. Using data from several X-ray satellites such as Chandra, XMM-Newton and Suzaku, we analized the spectral properties of the source X1822-371 and temporal evolution of the source XB1916-053.

A short introduction about X-ray binary systems and basics about accretion is presented in **chapter 1**, while in **chapter 2** I describe briefly the formation and evolution of binary systems.

The results we obtained analizing the source X1822-371 are described in **chapter 3**. Our aim was to understand the nature of the residuals between 0.6 and 0.8 keV previously observed in the XMM/EPIC-pn data by Iaria et al. (2013). We interpreted the Gaussian feature in absorption as a cyclotron resonant scattering feature (CRSF) produced close to the neutron star surface and derive the magnetic field strength at the surface of the neutron star. If our interpretation is correct this is the very first detection of a CRSF below 1 keV in a LMXB.

In the source XB 1916-053 the known orbital period derivative is extremely large

and can be explained by invoking an extreme, non-conservative mass transfer rate that is not easily justifiable. The results of our analysis of a large sample of data are presented in **chapter 4**. We had found that both in a conservative and non-conservative mass transfer scenario we have to invoke the presence of a third body to explain the observed sinusoidal modulation. We proposed that XB 1916-053 forms a hierarchical triple system.

Chapter 1

Binary systems

1.1 Introduction

One third of 339 X-ray sources listed in the fourth Uhuru catalogue (Forman et al., 1978) [1], compiled with data collected from the *Uhuru* satellite launched in 1970, have been classified as binary systems. X-ray binaries were identified since the sixties of the twentieth century [1] when space technology allowed to place X-ray detectors outside the Earth's atmosphere that, being opaque to x-rays, prevents the radiation from astronomical sources to be detected by ground devices. Since then numerous satellites that have been launched have explored the sky looking for X-ray sources and, to date, a few hundreds X-ray binary systems in our Galaxy and in nearby galaxies have been spotted (Liu et al, 2007) [3]

1.2 Basics about accretion

X-Ray binaries are among the brightest X-ray sources, their luminosities vary in the range of $10^{33} \div 10^{38} erg\, s^{-1}$ [2]. It became clear already few years after their discovery that the luminosity of X-ray binaries was due to accretion of matter onto a compact object (Shklovsky, 1967) [4]. The term accretion is the process of extraction of gravitational potential energy from matter that is captured by the gravitational field of a celestial body. Consider a body of mass M and radius

[1] In 1962 the discovery of Scorpius X-1 (Giacconi et al., 1962) [2], identified today as a binary system containing a neutron star

[2] The luminosity of the Sun is on the order of $10^{33} erg\, s^{-1}$

R*, the potential energy released from a mass m accreting on the surface of the object is:

$$\Delta E_{acc} = \frac{GMm}{R_*} = \xi mc^2$$

where G is the universal gravitational costant [3], $\xi = \frac{GM}{c^2 R_*}$ is the *efficiency* and the ratio $\frac{M}{R_*}$ is called *compactness*.
Assuming you have a white dwarf with radius $R_* = 10^3\, Km$ and mass $M = 1M_\odot$ ($\frac{M}{R_*} \approx 10^{24}\, g\, cm^{-1}$) you get for a gram of accreted mass: $\Delta E_{acc} = 1.3 \times 10^{17} erg$; while for a neutron star, whose radius is R*=10 Km and mass is $M = 1.4M_\odot$ ($\frac{M}{R_*} \approx 10^{27}\, g\, cm^{-1}$), we have: $\Delta E_{acc} = 1.9 \times 10^{20}\, erg$. On the other hand the energy extracted during nuclear fusion of one gram of hydrogen into helium is equal to:

$$\Delta E_{nucl} = 6.3 \times 10^{18}\, erg$$

Then the process of accretion onto a neutron star is about 30 times more efficient of the process of nuclear fusion and its efficiency depends from the compactness of the object that accretes matter.
The luminosity of a system that accretes matter is:

$$L_{acc} = \frac{GM\dot{m}}{R_*}$$

therefore, for given value of compactness, luminosity depends on the rate at which the matter accretes, denoted by $\dot{m}$. The luminosity that you can get in this way is not unlimited; there is a maximum luminosity, called *Eddington's limit*. Consider a spherical accretion flow in a steady state accretion regime and assume that the accreting matter is fully ionized hydrogen. Under these assumptions the radiation produced by the compact object surface due accretion of matter, exerts an outward pressure force mainly on free electrons, because the cross section for protons is a factor $(\frac{m_e}{m_p})^2$ smaller, where $\frac{m_e}{m_p} \sim 5 \times 10^{-4}$ is the ratio of the mass of the electron and the proton[4]; while the force of gravity directed inwards, acts mainly on protons, which are about 1860 times more massive than electrons. Due to the Coulomb attractive force which is exerted between protons and electrons

[3] $G = 6.67 \times 10^{-8}\, cm^3\, g^{-1}\, s^{-2}$.
[4] with $m_e \sim 0.9 \times 10^{-27}\, g$ and $m_p \sim 1.672 \times 10^{-24}\, g$.

the effects of these two forces will be transmitted to both types of particles. These two forces will equilibrate at the Eddington's luminosity limit value:

$$L_{Edd} = \frac{4\pi G M m_p c}{\sigma_T} \approxeq 1.3 * 10^{38} \Big(\frac{M}{M_\odot} \Big) ergs^{-1} \ [5]$$

For a luminosity higher than the Eddington limit, the radiation pressure will overcome the gravity attractive force, and this limits the accretion rate to the Eddington value.

1.3 X-ray binaries

A binary system is a set of two astronomical objects that, following the laws of Kepler, revolve around a common center of mass under mutual attraction due to gravity. X-ray binaries consist of a main sequence (or slighty evolved) star, called the companion star (or donor star), and a compact object, that is the end product of stellar evolution. During their life cycle, stars are systems in equilibrium in which thermonuclear reactions that occur in the nucleus generate radiation pressure needed to balance the gravity force that bring the star to gravitational collapse. During its evolution the star runs out of nuclear fuel inside, so the radiation pressure will not be able to contrast the collapse of the star. If the collapsed object has a mass less than the Chandrasekhar's limit ($1.44 M_\odot$), the outward pressure of the electron-degenerate gas in its nucleus can restore a balance. For compact objects with a mass between $1.44 \div 3.8 M_\odot$, the outward pressure is given by a degenerate neutron gas formed by inverse β^- decay: $p^+ + e^- \rightarrow n + \nu$. Finally for stars whose mass is greater than the Tolman-Oppenheimer-Volkoff ($3.8 M_\odot$) value no force is able to counteract the collapse and a singularity of spacetime is created, more commonly known as *black hole*.

In X-ray binary systems the compact object is a neutron star or a black hole; a possible classification of these systems can be made considering the mass of the companion star: we speak, then, of High Mass x-ray Binaries and Low Mass x-ray Binaries (White et al., 1995) [5].

[5] where $\sigma_T = 6.7 \times 10^{-25} cm^2$ is the Thomson cross section.

1.3.1 High Mass X-Ray Binaries

High Mass X-ray Binaries (HMXBs) have companions of mass greater than $5M_{\odot}$ [6] of spectral type O or B with an intense stellar wind (about $10^{-10}M_{\odot}yr^{-1}$)[7]. The X-ray luminosity vary between $10^{33} \div 10^{36} erg\, s^{-1}$, while the ratio between X-ray and optical brightness, defined as:

$$\text{R}= \frac{L_x(2 \div 10keV)}{L_{opt}(3000 \div 7000\mathring{A})} \quad [8]$$

is between 10^{-5} e 10 (Bradt e McClintock, 1983) [7]. The HMXBs are young binary systems (about 10^7 yr) where the compact object has a strong magnetic field (10^{12} G) [9], often have eccentric orbits ($0.1 < e < 0.4$) and orbital period ranging from 4.8 hours to 187 days (Staubert, 2008) [8].

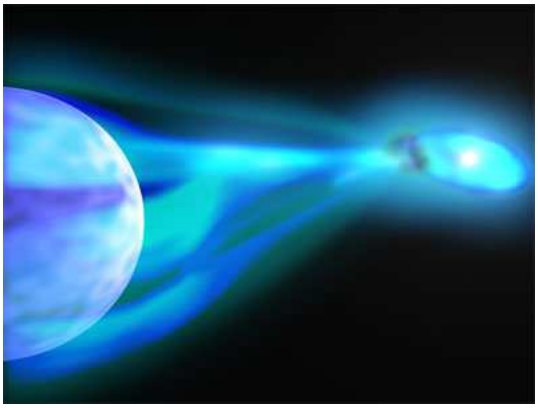

Figure 1.1: An High Mass X-Ray Binary: the compact object attracts the strong stellar wind of the companion (left) and accretes matter. (*Credits:* www.physorg.com/news8222.html)

1.3.2 Low Mass X-Ray Binaries

In Low Mass X-Ray binaries (LMXBs) (see figure 1.2) the companion star has a mass $M < 1M_{\odot}$ and is, generally, of spectral type G or K with stellar wind

[6] $M_{\odot}$ refers to the mass of the Sun approximately $2 \times 10^{30}\, Kg$.

[7] The loss of mass of the Sun because of the solar wind is about $10^{-14}M_{\odot}yr^{-1}$ (Gibson, 2001) [6]

[8] Where $L_x(2 \div 10keV)$ is the luminosity in the energy band between 2 and 10 keV and $L_{opt}(3000 \div 7000\mathring{A})$ is the luminosity in the wavelenght band between 3000 and 7000 angstrom

[9] The intensity of Sun's magnetic field is about one Gauss.

rather weak. Moreover the binary system is not very bright in optical band so the ratio $\frac{L_X}{L_{opt}}$ has values ranging from 100 to 1000, except in those systems where an high inclination angle of the plane of the orbit with respect to the line of sight hides the X-ray source by reducing the ratio to about 20. The LMXBs are old systems (about 10^9 yr) and this allowed the circularization of the orbit due to tidal effects; the compact object has a relatively low magnetic field (10^8 G) and the system has an orbital period ranging from 0.19 hours to 17 days (Staubert, 2008) [8].

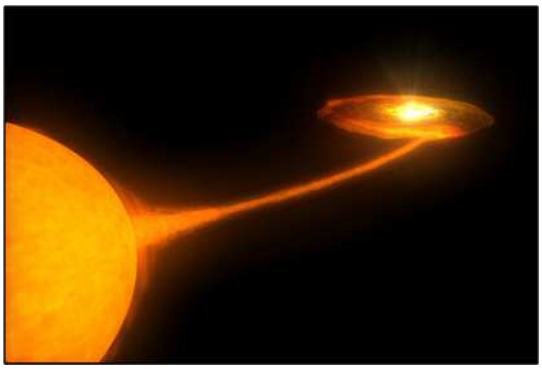

Figure 1.2: A Low Mass X-Ray Binary: the matter flows from the the inner Lagrangian point and accrete onto the compact object forming an accretion disk. (*Credits:* *http//:xraypulsars.aip.de:8180/xraypulsars*)

Observing light curves of Low Mass x-ray binaries a variety of modulations are noticed that can be ascribed to different inclination angle of the plane of the orbit with respect to the line of sight (see figure 1.3) and this allows a further classification of Low Mass x-ray Binaries. If the source is observed at an angle i$<$ 60° there will not be any modulations in light curve. At higher inclinations for 60° $<$i$<$ 75°, it is possible to observe a partial reductions of flux emitted by the source due to a bulge of matter on the outer rim of the accretion disk where the impact with accreting matter occurs, known as *dip*; in this case, as it is not possible to observe the eclipse, we speak of *pure dippers*. Increasing the angle of inclination, for 75° $<$i$<$ 80°, it is possible to see both dip and eclipse. For angle i$>$ 80° it is not possible to see dip and eclipses will become partial. LMXBs sources of this type are called *Accretion Disk Corona*(ADC); in these X-ray sources radiation produced in the inner regions light up the inner part of the disk causing evaporation of the superficial layers that form a corona that spreads up, generally, to the outer radius of the disk. This corona diffuses radiation from

the central source making the eclipse partial (White and Holt, 1982) [9]. In the event that the line of sight makes a big angle with the normal to the orbital plane it will not be possible to observe directly the radiation coming from the source, but it is observed a fraction of it diffused by the corona (Frank et al., 1987) [10].

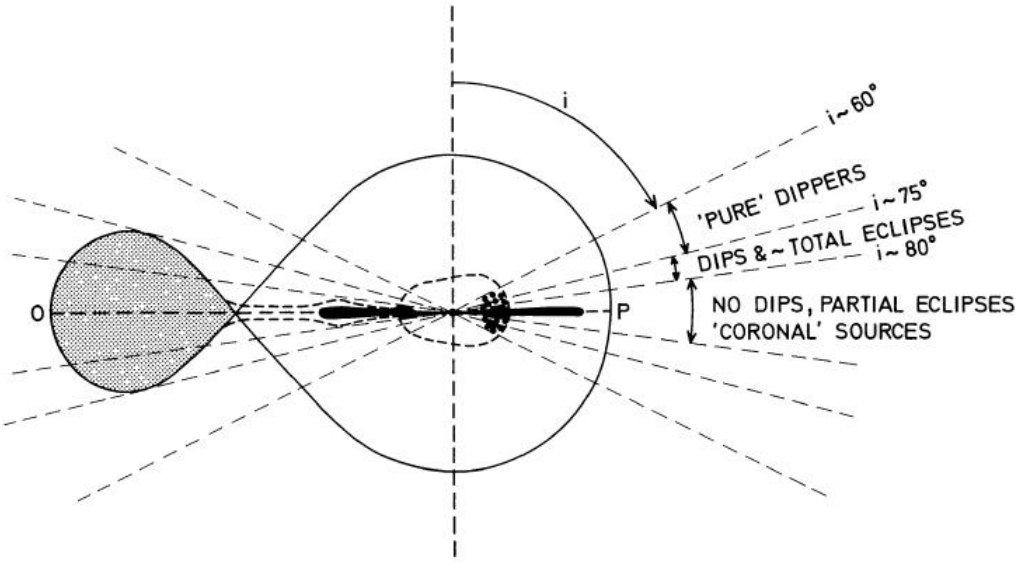

Figure 1.3: A Low Mass x-ray Binary system seen from different angles. The angle i is 0° along the direction perpendicular to the plane of the orbit (*Credits: Frank, King and Lasota (1987)*).

1.4 Accretion onto X-ray binaries

The mass transfer in X-ray binaries can be done in two different ways depending on the nature of the system:

- in High Mass x-ray Binaries using the capture of the wind emitted from the companion star by compact object (1.4.1);

- in Low Mass x-ray Binaries using the capture of matter of the companion star which flows through the inner Lagrangian point that connects the two Roche lobes[10] (1.4.2).

[10] A Roche lobe is the equipotential surface tear-drop-shaped around a star in a binary system (see figure 1.6)

1.4.1 Accretion by capture of stellar wind

We have seen that (see 1.3.1) the stars of spectral type O or B have an intense stellar wind. In systems where the companion star is of this type, the accretion (see paragraph 1.2) occurs through the capture of such a wind by the compact object (see figure 1.1) at a rate of about $10^{-6} M_{\odot} yr^{-1}$ [11] during its motion around the common center of mass. (see figure 1.4).

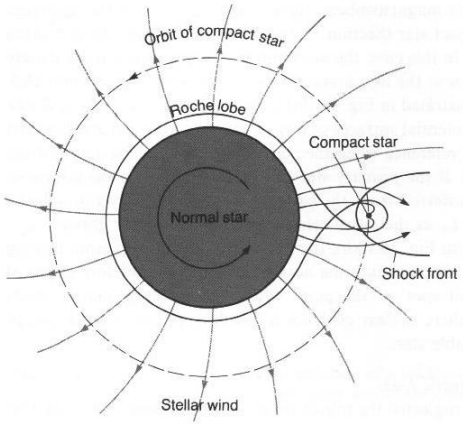

Figure 1.4: Accretion by capture of stellar wind (*Credits: Shapiro and Teukolsky (1983) - Black holes, white dwarfs and neutron stars: the physics of compact objects*).

It is possible to calculate the radius beyond which the matter ejected from the companion star cannot escape the compact object. In fact, let M_* be the mass of the compact object and v_* be its orbital speed. Assuming that the emission of stellar winds occurs radially at a speed v_{wind}, then the stellar wind speed relative to the compact object, v_{comp}, will simply be the vector sum of two speeds, or $v_{comp}^2 = v_*^2 + v_{wind}^2$. We compute now the momentum of a stellar wind moving in a gravitational field. The gravitational force per unit mass at a distance b from the compact object is $\frac{GM_*}{b^2}$ and the duration of this force is $\frac{2b}{v_{comp}}$; then the variation of momentum will be $\Delta p = \frac{2GM_*}{bv_{comp}}$. The result will be that the stellar wind will be deflected toward the axis of flow. As you can see in figure 1.5 at a distance l from the compact object stellar wind particles will be on flow axis: at this point the perpendicular component to the compact object of their speed will vanish.

Therefore the condition for the stellar wind from being captured by the compact object is that at distance l, the gravitational potential energy of matter is

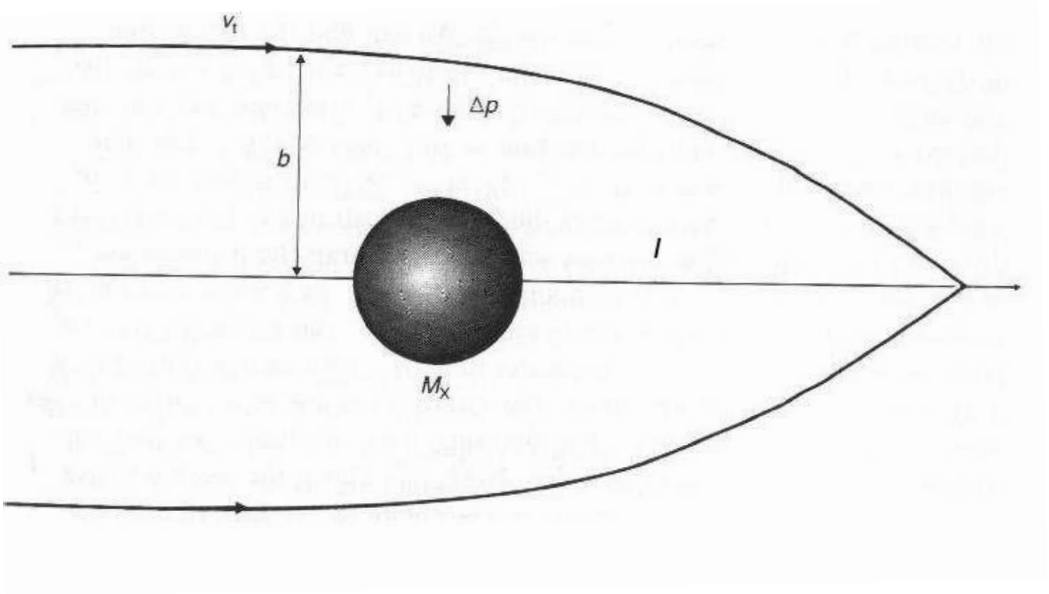

Figure 1.5: Accretion mechanism of a compact object of mass M_* through the capture of stellar winds. In the figure stellar wind speed with respect to the compact object is indicated with v_t, where b is the distance of the stellar wind from the compact object, l the distance along the axis of the flow where the stellar wind particles meet the axis of flow and Δp is the momentum of the particles of the stellar wind. (*Credits: M.S.Longair (2002) - High energy astrophysics - vol. II*).

greater than its kinetic energy. The kinetic energy per unit mass is about $\frac{1}{2}v_{comp}^2$, the distance $l = \frac{bv_{comp}}{v_\perp}$, where $v_\perp = \Delta p$, since we considered all quantities per unit mass. From this we deduce that *capture radius* is:

$$R_{capt} = \frac{2GM_*}{v_{comp}^2}$$

1.4.2 Accretion via *Roche lobe* overflow

Consider a binary system with a circular orbit. In a rotating reference frame equipotential surfaces can be described by the following expression:

$$\phi_R = -\frac{GM_1}{|\vec{r} - \vec{r_1}|} - \frac{GM_2}{|\vec{r} - \vec{r_2}|} - \frac{1}{2}(\vec{\omega} \times \vec{r})^2$$

where $\vec{\omega}$ is the angular velocity of the system orbital motion, while $\vec{r_1}$ and $\vec{r_2}$ are position vectors of the two stars, of mass M_1 and M_2, considered to be point-like.

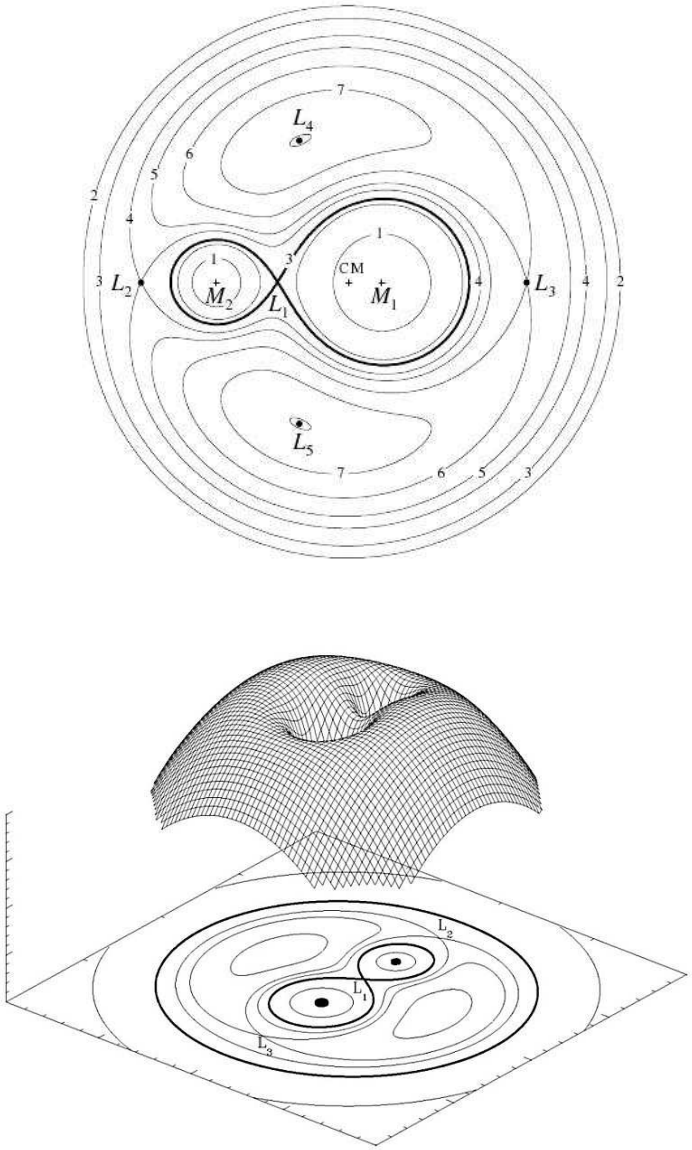

Figure 1.6: Equipotential surfaces for a system consisting of two point-like masses M_1 and M_2. The figure above shows the sections of the equipotential surface in the orbital plane such that $\phi_R = cost$. The surfaces are marked with numbers from 1 to 7 in order of increasing potential. The Roche lobe for the two stars is the "eight shape" highlighted in bold in figure and indicated with the number 3. The bottom figure shows a three-dimensional representation of the potential ϕ_R (*Credits:* *http://it.wikipedia.org/wiki/Lobo_di_Roche*; *Frank, King and Raine - Accretion power in astrophysics.*)

The *Roche lobes* are the smallest among the equipotential surfaces describing the gravitational potential of two objects that rotate around the center of mass of

the system (see figure 1.6). Their contact point is called *inner Lagrangian point*, denoted by L_1 .
The shape of the Roche lobes are determined only by the mass ratio of the two stars, $q = \frac{M_2}{M_1}$, whereas the binary separation a can be expressed from the third Kepler's law as:

$$a = \left(\frac{G\,(M_1 + M_2)\,P_{orb}^2}{4\pi^2} \right)^{1/3} \tag{1.1}$$

where G is the gravitational constant, M_1 and M_2 are the masses of the two stars and P_{orb} is the orbital period of the system. A useful approximated expression of the radius of the Roche lobe of a star, valid for $q \leq 0.8$, is given by Paczynski (1967) [12]:

$$R_L = 0.46\,a \left(\frac{M_2}{M_1 + M_2} \right)^{1/3} \tag{1.2}$$

All LMXB accrete through transfer of matter from the inner Lagrangian point at a rate between $10^{-10} \div 10^{-8} M_\odot yr^{-1}$ [11]. In fact if one of the stars expands, for istance due to stellar evolution and fills its Roche lobe up to the inner Lagrangian point, L_1, a point of unstable equilibrium, due to the pressure of the gas the matter tends to pass into the Roche lobe of the compact object. In this way it is captured by the gravitational field of the other star and, since it possesses a specific angular momentum, it does not fall directly on the compact object, but begins to rotate around and forms an *accretion disk*. Due to viscous friction, matter in the disk loses angular momentum (which is transported outward) until it reaches the surface of the star. In the case of accretion from stellar wind, accretion disks may not form because the average angular momentum of the stellar wind is lower.

1.4.3 Accretion onto magnetized neutron stars

In the event that the compact object has an intense magnetic field, the accreting matter does not manage to directly reach the surface of the neutron star, but at a certain radius, called *Alfvén (or magnetospheric) radius*, the pressure exerted by the accreting matter, called *ram pressure*, equals the magnetic pressure and the flow is channelled along the magnetic field lines until reaches the polar caps (the magnetic field of neutron stars is of dipolar type). The resulting emission

of radiation, if the magnetic axis is not aligned with the axis of rotation of the compact object, is observed as a coherently pulsed signal (see figure 1.7).

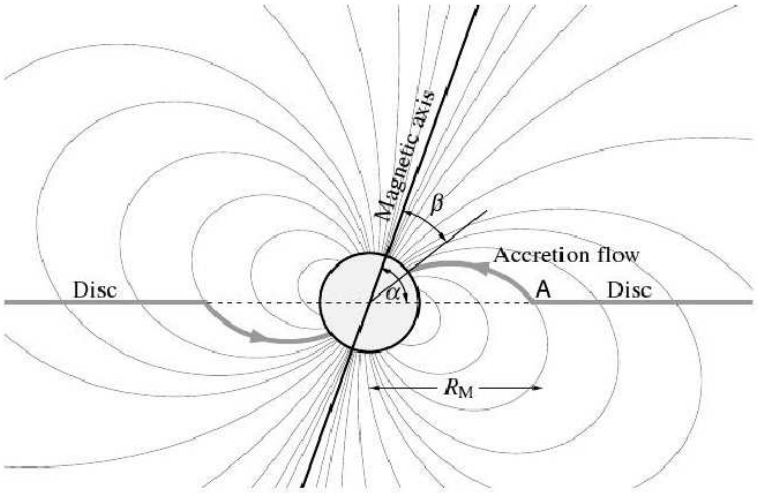

Figure 1.7: Accretion onto a neutron star with a strong magnetic field. R_M is the radius at which accreting matter is channeled along the lines of the magnetic field. (*Credits: Frank, King and Raine - Accretion power in astrophysics.*)

We calculate the magnetospheric radius as a function of the rate of accretion. We assume that the accretion flow has spherical symmetry, or $\dot{m} = 4\pi r^2 \rho v$ and the compact object magnetic field at the surface is dipolar, namely $B_s = \frac{\mu}{R_*^3}$. The magnetic field at a certain radius r from the object can be written in the form $B = \left(\frac{R_*}{r}\right)^3 B_s$. Magnetic pressure at distance r is $p_{mag} = \frac{B^2}{8\pi} = \frac{\left(\frac{R_*}{r}\right)^6 B_s^2}{8\pi}$. The *ram pressure* is $p_{ram} = \rho v_{ff}^2$, where v_{ff} is the free fall speed. Then, by equating the two terms, you get:

$$\rho v_{ff}^2 = \frac{\left(\frac{R_*}{r_M}\right)^6 B_s^2}{8\pi}$$

With appropriate calculations and expressing the free fall energy density in terms of rate of accretion, or $\rho v_{ff} = \frac{\dot{m}}{4\pi r_M^2}$ we have:

$$r_M = \left(\frac{B_s^4 R_*^{12}}{8GM_*\dot{m}^2}\right)^{\frac{1}{7}}$$

Assuming you have a solar mass neutron star that accretes matter at the Eddington luminosity limit you get $r_M = 1000km$, which is approximately 100

times the radius of the compact object. Hence the accreting matter does not fall directly on the surface of the star, but is channeled along the magnetic field lines and reaches the polar caps.

1.5 The radiation from X-ray binaries

To evaluate the wavelength of radiation emitted by X-Ray binary systems one should consider that the continuous spectrum of the emitted radiation can be characterized by a temperature, T_{rad}. In order to find an accretion luminosity (see paragraph 1.2) we can define the black body temperature as that temperature that the source should have if it emits radiation as a black body spectrum, i.e.:

$$T_b = \left(\frac{L_{acc}}{4\pi R_*^2 \sigma}\right)^{\frac{1}{4}} \text{ [11]}$$

You can also define the temperature, T_{th}, that would have the accreting matter if its gravitational potential energy is converted entirely into thermal energy:

$$T_{th} = \frac{2GMm_p}{3K\,R_*} \text{ [12]}$$

which is obtained by equating the gravitational potential energy of an accreting proton, $\frac{GMm_p}{R_*}$, with the thermal energy $\frac{3kT}{2}$ for each particle.

At this point we need to assess the nature of matter expanding on the surface of the neutron star:

- If it is optically thick, radiation reaches thermal equilibrium with accreting matter, then: $T_{rad} \sim T_b$;
- If it is optically thin, radiation will not interact with the accreting matter, and will not loose its energy, which will be converted into thermal energy, namely $T_{rad} \sim T_{th}$.

In the general case the temperature of the radiation will be between these two values:

[11] Where $\sigma = 5.67 \times 10^{-5}\, erg\, cm^{-2}\, s^{-1}\, K^{-4}$ is Stefan-Boltzmann costant, while with R_* indicates the radius of neutron star.

[12] $m_p = 1.672 \times 10^{-24}\, g$ indicates the mass of proton and with K= $1.38 \times 10^{-16}\, erg\, K^{-1}$ the Boltzmann costant.

$$T_b < T_{rad} < T_{th}$$

In the case of a solar mass neutron star, the temperature of this radiation is between $0.5\,keV < T_{rad} < 40\,MeV$. Typically the accreting matter is optically thick with a $T_{rad} \sim 1\,keV$, that lies in the X-Ray band of the electromagnetic spectrum.

1.6 Spectral analysis

The observed spectra of LMXBs consist of a black-body component which is the emission from the neutron star and the inner parts of accretion disk (see left panel of figure 1.8) and a Comptonized component, that when the angle between the orbital plane and the line of sight prevents to directly observe the central source, is produced in the accretion disk corona partially absorbed by interstellar medium and by neutral local matter (see right panel of figure 1.8).
The instruments on X-ray satellites do not measure directly the spectrum of a source, what they register are photon counts (C) within specific instrument channels, (I). This observed spectrum is related to the actual spectrum of the source (f(E)) by:

$$C(I) = \int_{-0}^{+\infty} f(E)R(I,E)\,dE \tag{1.3}$$

where R(I,E) is the instrumental response and is proportional to the probability that an incoming photon of energy E will be detected in channel I. To obtain the actual spectrum of a source, f(E), it is not possible to invert the equation 1.3. Usually it is assumed a model for the spectrum of the source (that can be described in terms of some parameters) and a predicted count spectrum (Cp(I)) is calculated and compared to the observed data (C(I)) using a fitting procedure to minimize the difference between the model and the data. The goodness of the fit is quantified with the χ^2-test, defined as follows:

$$\chi^2 = \sum \frac{(C(I) - C_p(I))^2}{\sigma^2(I)}$$

where $\sigma(I)$ is the error for channel I. For a given number of degrees of freedom ν , which is calculated as the number of channels minus the number of model parameters, it is possible to calculate the reduced χ^2, i.e. $\chi^2_\nu = \chi^2/\nu$. This provides a criterion for the goodness of the fit. In general $\chi^2 \sim \nu$, so if $\chi^2_\nu \gg 1$

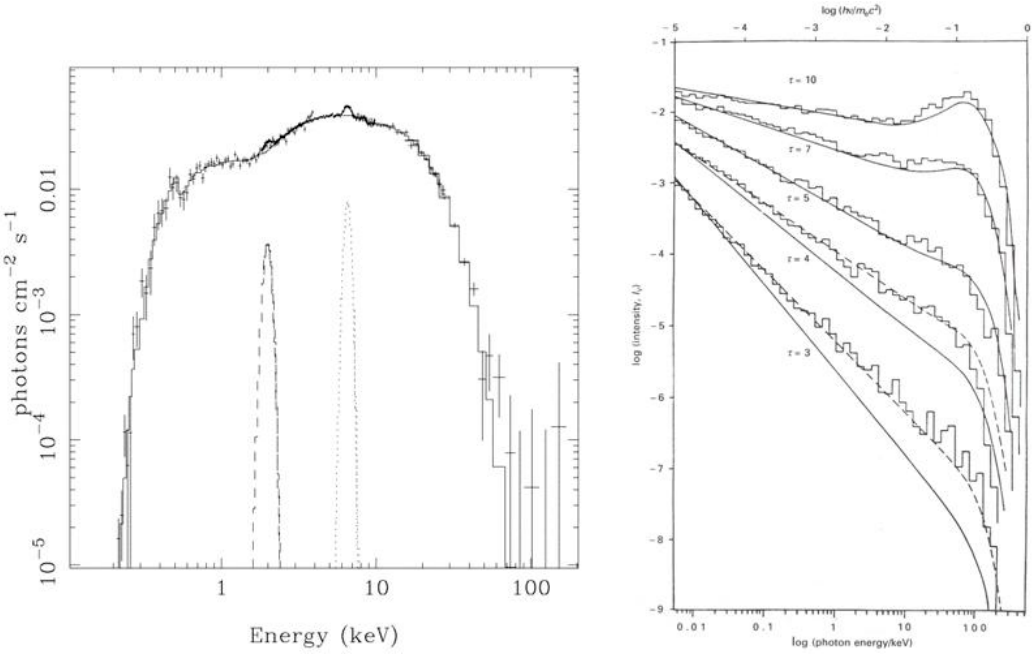

Figure 1.8: Low Mass X-ray binaries spectrum. Left panel: The spectrum of the source X1822-371 from BeppoSAX data: a blackboy component partially absorbed by neutral local matter; there are also visible two emission lines. (*Credits: Iaria et al., (2001)*). Right panel: The variation of the comptonized component as a function of τ, the optical depth of the corona. (*Credits:M.S.Longair (2002) - High energy astrophysics - vol. I*).)

indicates that the model is not the correct one, but might also indicate that the errors on the data have been under-estimated; conversely also a $\chi^2_\nu \ll 1$ may indicate that the errors on the data have been over-estimated.

1.6.1 Cyclotron lines

Young Neutron stars have magnetic fields of the order of 10^{12} Gauss, while in old neutron star it is about 10^8 Gauss. The only way to determine the magnetic field of a neutron star directly is to measure the energy of electron cyclotron resonance lines sometimes present in their X-ray spectra, because the resonance energy is proportional to the intensity of the magnetic field. In fact, an electron, in the presence of a strong magnetic field B, uniform and directed along z, moves along the field lines in a spiral trajectory of radius r_g (See fig.1.9):

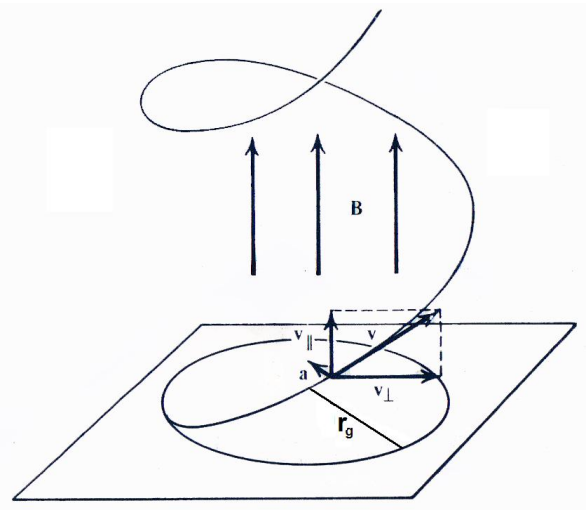

Figure 1.9: Motion of an electron in a magnetic field B. (*Credits:M.S.Longair (2002) - High energy astrophysics - vol. I*).)

$$r_g = c\frac{v_\perp m_e}{eB} \tag{1.4}$$

where $v_\perp$ is the velocity of the electron in a direction perpendicular to the field, m_e its rest mass, e its charge and c the speed of light. We need to introduce quantum mechanics if r_g is smaller than or comparable to the De Broglie wavelength associated with the electron:

$$\lambda = \frac{\hbar}{m_e v_\perp} \tag{1.5}$$

that is, for:

$$c\frac{v_\perp m_e}{eB} < \frac{\hbar}{m_e v_\perp} \tag{1.6}$$

then:

$$B > \frac{m_e^2 v_\perp^2 c}{e\hbar} = \left(\frac{v_\perp}{c}\right)^2 \frac{m_e^2 c^3}{e\hbar} = \left(\frac{v_\perp}{c}\right)^2 B_{cr} \tag{1.7}$$

where $B_{cr} = 4.41 \times 10^{13} G$ and $v_\perp$ is typically of the order of 0.01 c. In that case the kinetic energy of an electron in the direction perpendicular to B is quantized in the Landau energy levels. The n-th level of Landau has energy $E_n = nE_a$ (n = 0,1,2, ...) where:

$$E_a = \frac{eB\hbar}{m_e c} = 11.6 \times 10^{-12} B \ keV \tag{1.8}$$

is the energy of the fundamental cyclotron line. This result is valid in the non-relativistic limit, i.e. for $E_a < m_e c^2$ or $B < B_{cr}$. The average lifespan of the electrons in excited level is very small ($\sim 10^{-16}$ s) so the collisional decay rate is much smaller than the rate of radiative decay. Then an excited electron falls immediately on the fundamental level by emitting a photon of the same energy. This process is very similar to a scattering and the electrons are located most of the time in the ground state (n = 0). For typical values of neutron star magnetic field it is necessary to take into account the quantum effect, but the non-relativistic approximation should be valid for small values of the quantum number n.

Chapter 2

Evolution of close binary systems

2.1 Introduction

In the Galaxy about two thirds of stars are members of binary or multiple systems (Garmany, Conti & Massey, 1980 [13]; Abt, 1983 [14]). There are three possible mechanisms to form a binary system (Tohline, 2002) [15]: by **capture**, when stars become grouped together in bound pairs through dynamical encounters; by **fission**, when the gas cloud where stars are forming spontaneously break into pieces that are in orbit about one another and by **delayed breakup**, when the process of fission happens, due to an instability, after the cloud has formed a stable configuration. Binary systems can be classified as (see figure 2.1):

- Detached, when the distance between the two stars is much greater than their radii;
- Semi-detached, when one star of the system has filled its Roche lobe and mass transfer takes place (see 1.4.2);
- Contact, when both stars fill their Roche lobes.

2.2 Formation of neutron stars

In a binary system, where the components are well separated, the stars can be considered to evolve indipendently; therefore, in detached binary systems the evolution can be studied considering that the stars of the system do not affect

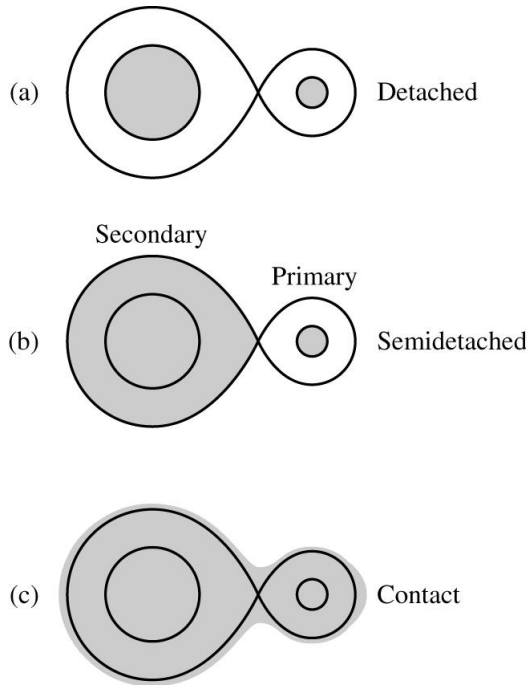

Figure 2.1: Types of close binary systems: a) Detached, b)semi-detached, c)Contact (*Credits: Kopal, Z., 1959 - Close Binary Systems, The International Astrophysics Series, vol.5*)[16].

each other so much during the main sequence phase (case a-Detached) because the radius of the stars does not change much and they do not fill their Roche lobes. However, when hydrogen is exhausted in the most massive of the two stars, the stellar core rapidly shrinks, external layers expand and mass transfer begins (case b-Semi-detached) (Postnov & Yungelson, 2014 [17]).

Mass trasfer between the two stars allows to understand some processes at the base of binary systems evolution. In fact, depending on principles of stars's evolution, in close binary systems, the neutron star or black hole can hardly exist. This because the progenitor of neutron star must have been a massive star that should evolve first and explode as a supernova, but in this way the system should be distroyed if more than half of the total mass of the binary is suddenly ejected (see e.g. Blaauw, 1961 [18] and Batthracharya et al., 1991 [19]). Furthermore, another problem is about the separation between the two stars; in fact the progenitor star must have had a radius much larger than the current separation. So these systems must have lost a large amount of orbital angular

momentum. (Tauris& van den Heuvel, 2006)[20].
A scenario that may explain the presence of neutron stars in binary systems is that of the "spiral-in+kick velocity". When a massive star evolves off the main sequence, it expands its radius. However, in close binary systems, the gravitational field sets a limit (Roche lobe, see 1.4.2) on the radial growth of each component. After having filled its Roche lobe, matter starts to flow from the donor star to the compact object, or in some case even lost from the system; this also results in angular momentum losses, in changes of the orbital parameters and possibly in merging of the stars. The transfer rate is so high that the companion star is eventually engulfed by the massive primary and a common envelope is formed around the low-mass star and the core of the primary. Friction and tidal torques cause the secondary to spiral-in to the envelope releasing orbital energy. This energy is deposited in the common envelope that is ejected from the system. This phase of the evolutionary process of binary systems is called: **common envelope** phase. In this way a closer binary, consisting of the low-mass secondary and the helium core of the primary, is formed, which can survive the supernova explosion since the most of the mass is lost prior to the explosion with the ejection of the envelope and if a kick velocity, in the right direction, is imparted to the newly born compact star (Kalogera & Webbing, 1998 [21]). Another scenario was suggested in 1973 by Whelan & Iben in 1973 ([22]). They showed that an **accretion-induced collapse** of a massive white dwarf may lead to the formation of a neutron star. In fact, after the core emerges from the spiral-in it evolves into a massive white dwarf and avoids the supernova explosion. When mass transfer is initiated, either by loss of angular momentum or by expansion of the secondary, the white dwarf accretes mass until it overcomes the Chandrasekhar limit, at which point it implodes with little mass losses. In this way the binary system may survive and a neutron star is formed. Furthermore, the process just described may explain also the presence of young neutron stars in old binaries. It is known that the magnetic field of a neutron star decays on a time scale of a few million years and this mechanism may explain why radio pulsars in old binary system own magnetic field $> 10^8$ G (Verbunt et al., 1993 [23]).

2.3 Formation of Low Mass X-Ray Binaries

Before analyzing a possible scenario that leads to the formation of a Low Mass X-Ray Binary system, it is useful to remeber the time scales in which the evolutionary processes in stars take place.

First the *nuclear time scale*, t_n, or the time in which a star radiates away all the energy that can be released by nuclear reactions

$$t_n \simeq \frac{M/M_\odot}{L/L_\odot} \times 10^{10} yr,$$

then the *thermal time scale*, t_{th}, or the time in which a star would radiate away all its thermal energy if the nuclear production were suddenly turned off

$$t_{th} \simeq \frac{(M/M_\odot)^2}{(R/R_\odot)(L/L_\odot)} 3.1 \times 10^7 yr,$$

and in the end the *dynamical time scale*, t_d, or the time in which a star would collapse if the pressure supporting it against gravity were suddenly removed

$$t_d \simeq 0.04 \frac{(M_\odot/M)^{1/2}}{(R/R_\odot)^{3/2}} days$$

In reference to figure 2.2 and following Postnov & Yungelson, 2014 [17], the step leading to the formation of Low Mass X-Ray binaries are:

1- A pair of high-mass OB main-sequence stars is detached and are inside their Roche lobes. The more massive star burns out hydrogen in its central parts and forms a dense central helium core, while the tidal interactions remove the possible eccentricity of the orbit. The duration of this stage is determined by the hydrogen burning time of the primary, that is nuclear time scale.

2- After core hydrogen exhaustion, the primary leaves the main-sequence and starts to expand rapidly. When its radius approaches the Roche lobe, mass transfer onto the secondary, less massive star, which still resides on the main-sequence, begins. This stage proceeds on the thermal time scale of the donor.

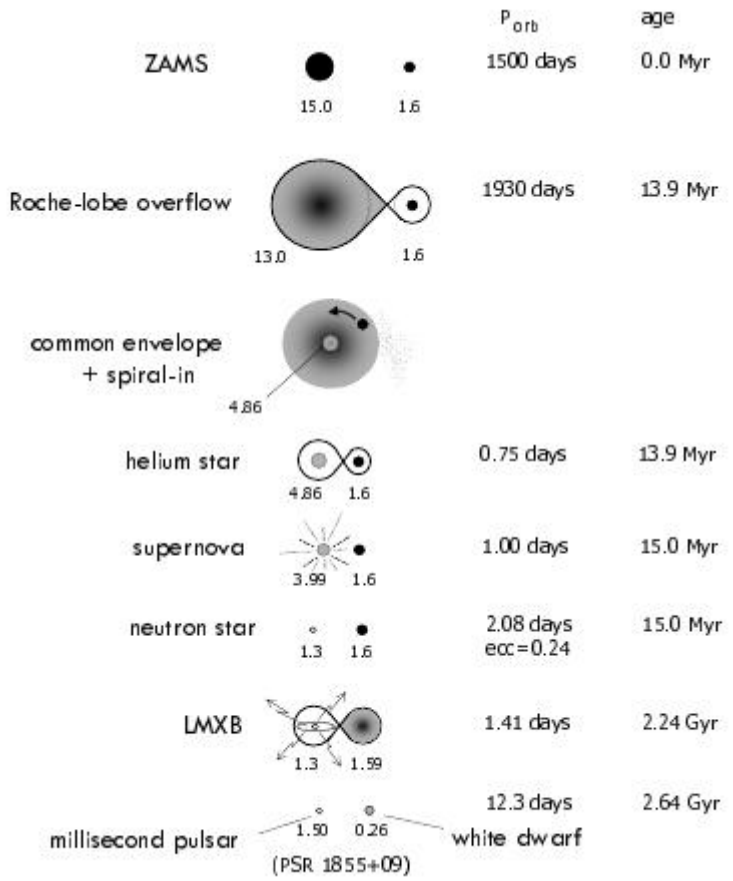

Figure 2.2: The evolution of a binary system eventually leading to an LMXB and finally the formation of a binary millisecond pulsar. Parameters governing the specific orbital angular momentum of ejected matter, the common envelope and spiral-in phase, the asymmetric supernova explosion and the stellar evolution of the naked helium star all have a large impact on the exact evolution. Parameters are given for a scenario leading to the formation of the observed binary millisecond pulsar PSR 1855+09. The stellar masses given are in solar units.(*Credits:Tauris & Van den Heuvel, 2003 [20]*).

3- Common envelope phase. In this phase the companion of the mass-losing star may find itself engulfed by the envelope of the donor. The envelope removes angular momentum from the orbital motion and releases energy, so the companion star starts to spiral-in, while the orbit shrinks and envelope heats. The process continues until the envelope gains enough energy that is expelled or the companion star merges with the core of the donor star. Mass transfer ends when most of the primary's hydrogen envelope is lost, so a naked helium core is left.

4- Now there are two possible scenario that lead to the formation of a neutron star. In the first scenario the helium core that remains after the spiral-in phase eventually explodes as supernova. This may lead to the destruction of the system, but a properly oriented kick velocity can keep the system bound. In the second scenario the helium star evolves into a massive white dwarf and avoids the supernova explosion. Then a secondary mass transfer is initiated, either by loss of angular momentum or by expansion of the secondary, so the white dwarf accretes mass until it overcomes the Chandrasekhar limit, at which point it implodes with little mass losses and a neutron star is formed.

5- Now the companion star evolves and starts to transfer matter onto the compact object via the inner Lagrangian point. The matter that accretes onto the neutron star has a specific angular momentum so it does not fall directly onto the neutron star but forms an accretion disk that reprocess the radiation originating from the central object and emits X-Ray. The system has become a Low Mass X-Ray Binary.

It must be noted that the scenario just sketched applies only to close binaries and that low-mass binaries with neutron stars can be dynamically formed in dense stellar environments, for example in globular clusters.

2.4 Orbital evolution

Roche lobe overflow, and the consequent orbital evolution of the binary system, can happen due to mass exchange or due to orbital shrinkage caused by angular momentum losses. Mass transfer can happen in conservative way or in a non conservative way, while angular momentum loss can take place by gravitational radiation or by magnetic braking (Verbut, 1993 [23]).

2.4.1 Conservative and non-conservative mass transfer

The mass transfer is **conservative** when there are no mass losses from the binary system. In this case all the mass lost by one star is gained by the other, so:

$$\dot{M}_1 = -\dot{M}_2 \tag{2.1}$$

where the dot indicates a time derivative, consequently the conservation of mass may be written as:

$$M_1 + M_2 = costant \tag{2.2}$$

When mass is lost from the binary, the mass trasfer is called **non-conservative**; the equations become more complicated and the equations 2.1 becomes:

$$\dot{M_1} = -\beta \dot{M_2} \tag{2.3}$$

that we can write as:

$$\dot{M_1} + \dot{M_2} = (1 - \beta)\, \dot{M_2} \tag{2.4}$$

i.e. a fraction β of the mass lost by the donor star is accreted onto its companion, while the rest leaves the system.

2.4.2 Angular momentum loss

In the case of conservative mass transfer the conservation of angular momentum of the binary assuming a circular orbit is:

$$J_b = M_1 M_2 \sqrt{\frac{Ga}{M_1 + M_2}} = costant \tag{2.5}$$

where G is the universal gravitational costant and a is the binary separation (see eq.1.1). Of course we are assuming that both the spin angular momentun of the single stars and that of the rotation of the accretion disk are negligible with respect to the angular momentum of the orbital revolution. The time derivative of the equation 2.5 can be written:

$$\frac{\dot{a}}{a} = 2\frac{\dot{J_b}}{J_b} - 2\left(1 - \frac{M_2}{M_1}\right)\frac{\dot{M_2}}{M_2} \tag{2.6}$$

where the subscript 1 indicates the mass of the compact object and subscript 2 indicates the mass donor star. Consider first a binary system whose angular momentum is conserved: the donor star loses matter, that is $\dot{M_2} < 0$ and, according to equation 2.6, we have that if $M_2 > M_1$, $\dot{a} < 0$, namely the distance between the star decreases. This is a situation that we can find in HMXBs, where the process of accretion keeps the system bound. Conversely if $M_2 < M_1$, $\dot{a} > 0$, the distance between the star increases and the binary detaches, stopping the mass transfer

and accretion of matter onto the compact object. This is a typical case of LMXB, where the companion star has $M < 1M_{\odot}$. Thus to prevent the destruction of the binary system it is required that the system loses angular momentum. In the case of non-conservative mass transfer, the mass lost from the system will carry angular momentum. If we write the specific angular momentum of the mass that is lost as α times the specific angular momentum of the mass-losing star, the Equation 2.5 becomes:

$$\frac{\dot{J}_{\dot{M}}}{J} = \alpha(1-\beta)\frac{M_1}{M_1+M_2}\frac{\dot{M}_2}{M_2} \tag{2.7}$$

where with $\dot{J}_{\dot{M}}$ we indicate the loss of angular momentum due to loss of matter.

2.4.2.1 Angular momentum loss by gravitational radiation

In compact binaries the orbital periods are short, so the orbital velocities must be high. For this reason it is possible that these systems lose angular momentum due to gravitational quadrupole radiation. The loss of angular momentum via gravitational radiation may be written, using the Kepler's law, as (see King, 1988 [24]):

$$-\left(\frac{\dot{J}}{J}\right)_{GR} = \frac{32G^3}{5c^5}\frac{M_1M_2(M_1+M_2)}{a^4} \tag{2.8}$$

This formula holds for circular orbit, while for an eccentric orbit, this should be multiplied by a function of the eccentricity. The strong dependence on the size of the orbit (a^4) means that this process is dominant in very close binaries (for binary system of orbital period less than 2 hours).

2.4.2.2 Angular momentum loss by magnetic braking

The rotation of single stars is observed to slow down with age. This because there is a loss of angular momentum via their stellar winds. In fact, although the amount of mass lost in the wind is very small, due to the presence of the magnetic field, that forces the wind matter to corotate to a large distance from the stellar surface, the angular momentum's losses may be important. The result in a close binary system is that the losses of angular momentum of the donor star are transferred to the entire system due to the tidal forces which force the star to corotate with it. The formula describing the orbital angular momentum loss due to magnetic braking is (see King, 1988 [24]):

$$-\left(\frac{\dot{J}}{J}\right)_{MB} \approx 4 \times 10^{-30} scm^{-2} \frac{G(M_1 + M_2)^2 R_1^4}{M_2 a^5} \tag{2.9}$$

This kind of mechanism become dominant for binary systems with orbital periods greater than 2 hours. This is because, for short orbital periods, the companion mass should be quite small. In particular for orbital periods less that about 3 hours the main sequence stellar companion should have a mass below $0.3 M_\odot$. In this case the companion star becomes fully convective and cannot sustain anymore a dipole magnetic field (see Verbunt et al.,(1981) [25]).

Chapter 3

Direct measure of the magnetic field of X1822-371

This chapter is adapted from the paper: *A possible cyclotron resonance scattering feature near 0.7 keV in X1822-371*, by R.Iaria et al., 2015 ([26]).

3.1 Abstract

The aim of this work is to address the origin of the large residuals below 0.8 keV previously observed in the XMM/EPIC-pn spectrum of the source X1822-371, a low-mass X-ray binary system (LMXB) viewed at a high inclination angle. We analyse all available X-ray observations of X1822-371 made with XMM-Newton, Chandra, Suzaku and INTEGRAL satellites. The Suzaku and INTEGRAL broad band energy coverage allows us to constrain the spectral shape of the continuum emission well. We use the model already proposed for this source, consisting of a Comptonised component absorbed by interstellar matter and partially absorbed by local neutral matter, and we added a Gaussian feature in absorption at ~ 0.7 keV. This addition significantly improves the fit and flattens the residuals between 0.6 and 0.8 keV. We interpret the Gaussian feature in absorption as a cyclotron resonant scattering feature (CRSF) produced close to the neutron star surface and derive the magnetic field strength at the surface of the neutron star, $(8.8 \pm 0.3) \times 10^{10} G$ for a radius of 10 km. We derive the pulse period in the EPIC-pn data to be 0.5928850(6) s and estimate that the spin period derivative of X1822-371 is $(-2.55 \pm 0.03) \times 10^{-12} s/s$ using all available pulse

period measurements. Assuming that the intrinsic luminosity of X1822-371 is at the Eddington limit and using the values of spin period and spin period derivative of the source, we constrain the neutron star and companion star masses. We find the neutron star and the companion star masses to be $1.69 \pm 0.13 M_{\odot}$ and $0.46 \pm 0.02 M_{\odot}$, respectively, for a neutron star radius of 10 km.

3.2 Introduction

Neutron stars (NS) are thought to be born with magnetic fields (B-fields) above $10^{12}G$. Direct measurements of the strength of these fields come from the detection of cyclotron resonant scattering features (CRSFs). In accreting NS, X-ray pulsations and CRSFs are common in systems containing a young high-mass companion (HMXBs), with typical strengths of the NS B-field between $10^{12}G - 10^{13}G$, whereas in binary systems containing a low-mass companion (LMXBs) pulsations are detected only in a small fraction of systems, and no CRSF has been detected to date. The most likely explanation is that in such systems, the NS B-field is sufficiently decayed in the course of its evolution (see chapter 2) to a value that, at accretion rates corresponding to a luminosity of $10^{35} - 10^{38} erg\ s^{-1}$, the corresponding magnetospheric radius becomes smaller than the NS radius.
In LMXBs when pulsations are detected, the inferred NS B-fields are of the order of $10^{8}G - 10^{9}G$, which is about three orders of magnitude less than the typical values for HMXBs. Intermediate values of the NS B-field, between these two ranges, are uncommonly observed, most probably for evolutionary reasons. However, some notable exceptions exist, such as (i) the 11 Hz pulsar IGR J17480-2446 (Papitto et al., 2011) [27], whose NS B-field was estimated in the range $2 \times 10^{8} - 2.4 \times 10^{10}G$; (ii) the 2.1 Hz X-Ray pulsar GRO J1744-28, with an estimated B-field of $\sim 2.4 \times 10^{11}G$ (Cui, 1997) [28]; and, finally (iii) the 1.7 Hz X1822-371 (Jonker & Van der Klis, 2001) [29].
Despite the small sample that it belongs to, the peculiarity of X1822-371 still stands out. Analysing the RXTE data of X1822-371, Jonker & Van der Klis, 2001 [29] detected for the first time a coherent pulsation at 0.593 s associated with the NS spin period and inferred a spin period derivative of $(-2.85 \pm 0.04) \times 10^{-12} s\ s^{-1}$.

Analysing RXTE data from 51976 to 52883 MJD, Jain et al. (2010) [30] constrained the spin period derivative better, finding $(-2.481 \pm 0.004) \times 10^{-12} s\ s^{-1}$. The ephemerides of X1822-371 has recently been updated by Iaria et al. (2011)

[31], who estimated an orbital period of 5.5706124(7) h and an orbital period derivative of $(1.51 \pm 0.08) \times 10^{-10} s\ s^{-1}$ when analysing X-ray data spanning 30 years. A similar sample of data was analysed by Burderi et al. (2010) [32] who obtained an orbital period derivatice of $(1.50 \pm 0.07) \times 10^{-10} s\ s^{-1}$. In an independent paper, Jain et al. (2010) [30], obtained an orbital period derivative of $(1.3 \pm 0.3) \times 10^{-10} s\ s^{-1}$, from X-ray data and, studying the optical and UV data of X1822-371,Bayless et al. (2010) [33] derived the new optical ephemeris for the source finding an orbital period derivative of $(2.1 \pm 0.2) \times 10^{10} s\ s^{-1}$. Burderi et al. (2010) [32] show that the orbital-period derivative is three orders of magnitude larger than what is expected from conservative mass transfer driven by magnetic braking and/or gravitational radiation. They conclude that the mass transfer rate from the companion star is between 3.5 and 7.5 times the Eddington limit ($\sim 1.1 \times 10^{18} erg\ s^{-1}$) for a NS mass of $1 M_{\odot}$ and NS radius of 10 km), suggesting that the mass transfer has to be highly non-conservative, with the NS accreting at the Eddington limit and the rest of the transferred mass expelled from the system by the radiation pressure. Bayless et al. (2010) [33] show that the accretion rate onto the NS should be $\sim 6.4 \times 10^{-8} M_{\odot} yr^{-1}$ in a conservative mass transfer scenario, again suggesting a highly non-conservative mass transfer. The large orbital period derivative is a clear clue that the intrinsic luminosity of X1822-371 is at the Eddington limit, which is almost two orders of magnitude higher than the observed luminosity (i.e. $\sim 10^{36} erg\ s^{-1}$, see e.g. Hellier& Mason, 1989 [34], Heinz& Novak, 2001 [35],Parmar et al.,2000 [36], Iaria et al., 2001 [37]).

This is also supported by the ratio L_x/L_{opt} of X1822-371. Hellier & Mason (1989)[34] showed that the ratio L_x/L_{opt} for X1822-371 is $\sim$ 20, a factor 50 smaller than the typical value of 1000 for the other LMXBs. This suggests that the intrinsic X-ray luminosity is underestimated by at least a factor of 50. Finally, Jonker & van der Klis (2001) [29] show that for a luminosity of $10^{36} erg\ s^{-1}$, the NS B-field strength assumes an unlikely value of $8 \times 10^{16} G$, while for a luminosity of the source of $\sim 10^{38} erg\ s^{-1}$, it assumes a more conceivable value of $8 \times 10^{10} G$. Recently when analysing an XMM-Newton observation of X1822-371 and using RGS and EPIC-pn data, Iaria et al. (2013) [38] fitted the X-ray spectrum of this source to a model consisting of a Comptonised component `CompTT`[1], absorbed by

[1]The names of the cited spectral models are consistent with those adopted in the spectral fitting package XSPEC (Arnaud, 1996). The models are described in http://heasarc.gsfc.nasa.gov/xanadu/xspec/manual/XspecModels.html

interstellar neutral matter and partially absorbed by local neutral matter. The authors took the Thomson scattering of the local neutral matter into account by adding the `cabs`[2] component and imposed that the equivalent hydrogen column density of the `cabs` component is the same as the local neutral matter. The adopted model is similar to the one previously used by Iaria et al. (2001) [37] to fit the averaged BeppoSAX spectrum of X1822-371. Iaria et al. (2013) [38] suggest that the Comptonised component is produced in the inner regions of the system, which are not directly observable. The observed flux is only 1% of the total intrinsic luminosity, the fraction scattered along the line of sight by an extended optically thin corona with an optical depth $\tau \simeq 0.01$. This scenario explains why the observed luminosity of the source is $\sim 10^{36} ergs^{-1}$, while the orbital period derivative suggests an intrinsic luminosity of X1822-371 at the Eddington limit. Furthermore, Iaria et al. (2013) [38] found that large residuals are present in the EPIC-pn spectrum below 0.9 keV and fitted those residuals by adding a black-body component with a temperature of 0.06 keV, although they suggest that further investigations were needed to understand the physical origin of this component. Recently, Sasano et al. (2014) [39] have analysed a Suzaku observation of X1822-371 in the $1 \div 45$ keV energy range. The authors detect the NS pulsation in the HXD/PIN instrument at 0.5924337(1) s and inferred a spin period derivative of $(-2.43 \pm 0.05) \times 10^{-12} s/s$; they also suggest the presence of a CRSF at 33 keV and inferred from this value a NS B-field of $\sim 2.8 \times 10^{12} G$ and a luminosity of the source of $\sim 3 \times 10^{37} erg\ s^{-1}$. In this work we determine the NS spin period of X1822-371 during the XMM-Newton observation and derive a new estimation of the spin period derivative, also taking all the measurements of the spin period reported in literature into account, including our derived value. We analyse the combined spectra of X1822-371 obtained with XMM-Newton, Chandra (the same data sets as analysed by Iaria et al. 2013 [38]), Suzaku (the same data set as analysed by Sasano et al. 2014 [39]), and INTEGRAL. We show the presence of large residuals close to 0.7 keV, while we do not find evidence of a cyclotron feature at 33 keV, unlike what has been suggested by Sasano et al. (2014) [39]. Moreover, we show that a CRSF at 33 keV would not be consistent with the evidence that the NS in X1822-371 is spinning up. Fitting the residuals near 0.7 keV with a CRSF centered at 0.72 keV, we determine a NS B-field

[2]The models are described in http://heasarc.gsfc.nasa.gov/xanadu/xspec/manual/XspecModels.html

(surface) strength between $7.8 \times 10^{10} G$ and $9.3 \times 10^{10} G$ for a NS radius ranging between 9.5 and 11.5 km.

3.3 Observations

3.3.1 The Suzaku observation

The X-ray satellite *Suzaku* observed X1822-371 on 2006 October 2 with an elapsed time of 88 ks. Both the X-ray Imaging Spectrometers (0.2?12 keV, XISs; Koyama et al., 2007 [40]) and the Hard X-ray Detector (10?600 keV, HXD; Takahashi et al. 2007 [41]) instruments were used during these observations. There are four XIS detectors, numbered as 0 to 3. XIS0, XIS2, and XIS3 all use front-illuminated CCDs and have very similar responses, while XIS1 uses a back-illuminated CCD. The HXD instrument includes both positive intrinsic negative (PIN) diodes working between 10 and 70 keV and the gadolinium silicate (GSO) scintillators working between 30?600 keV. Both the PIN and GSO are collimated (non-imaging) instruments. During the observation, XIS0 and XIS1 worked in 1/4 Window option, while XIS2 and XIS3 worked in full window. The effective exposure time of each XIS CCD is nearly 38 ks, and the HXD/PIN exposure time is nearly 31 ks.

We reprocessed the data using the `aepipeline` tool provided by *Suzaku* FTOOLS version 20 [3] and applying the latest calibration available as of 2013 November. We then applied the publicly available tool `aeattcor.sl` [4] by John E. Davis to obtain a new attitude file for each observation. This tool corrects the effects of thermal flexing of the Suzaku spacecraft and obtains a more accurate estimate of the spacecraft attitude. For our observation, the above attitude correction produces sharper point-spread-function (PSF) images. With the new attitude file, we updated the XIS event files using the FTOOLS `xiscoord` program. We estimated the pile-up fractions using the publicly available tool `pileup_estimate.sl` [5] by Michael A. Nowak. The pileup fraction refers to the ratio of events lost via grade or energy migration to the events expected in the absence of pile-up. The unfiltered pile-up fractions integrated over a circular region centred on the brightest

[3] For more details see: http://heasarc.gsfc.nasa.gov/docs/suzaku/analysis/suzaku_ftools.html
[4] see: http://space.mit.edu/ASC/software/suzaku/aeatt.html
[5] see: http://space.mit.edu/ASC/software/suzaku/pile_estimate.sl

pixel of the CCD and with a radius of 105" are 4.6%, 3.9%, 10.4%, and 9.9% for XIS0, XIS1, XIS2, and XIS3, respectively. The large pile-up fraction in XIS2 and XIS3 is due to the two CCDs working in full window during the observation. To mitigate the pile-up effects in the spectra extracted from XIS2 and XIS3, we used annular regions, while we adopted circular regions with a radius of 105" to extract the spectra from XIS0 and XIS1. Adopting annulus regions with inner and outer radii of 28 and 105 , respectively, the pile-up fractions are 4.8% for XIS2 and 4.6% for XIS3. The background spectra were extracted using the same regions as were adopted to extract the source spectra and centred where the influence of the source photons is weak (or absent) in the CCDs. The response files of the XIS for each observation were generated using the `xisrmfgen` Suzaku tool, and the corresponding ancillary files were extracted using the `xisarfgen` Suzaku tool, suitable for a point-like source. Because the responses of XIS0, XIS2, and XIS3 are on the whole very similar, we combined their spectra and responses using the script addascaspec. The XIS spectra were rebinned to have 1024 energy channels. We also extracted the PIN spectra using the Suzaku tool `hxdpinxbpi`. The non X-ray and cosmic X-ray backgrounds were taken into account. The non X-ray background (NXB) was calculated from the background event files distributed by the HXD team. The cosmic X-ray background (CXB) is from the model by Boldt (1987) [42]. The response files provided by the HXD team were used. The GSO data were not used, considering the low signal-to-noise ratio above 40 keV.

3.3.2 The XMM-Newton observation

The region of the sky containing X1822-371 was observed by *XMM-Newton* between 2001 March 07 13:12:48 UT and March 08 03:32:53 UT (Obs. ID. 0111230101) for a duration of 53.8 ks. The European Photon Imaging Camera (EPIC) on-board XMM-Newton consists of three coaligned high-throughput X-ray telescopes. Imaging charge-coupled-device (CCD) detectors were placed in the focus of each telescope. Two of the CCD detectors are Metal Oxide Semiconductor (MOS) CCD arrays (see Turner et al. 2001), while the third camera uses pn CCDs (hereafter EPIC-pn, see Strüder et al. 2001 [43]). Behind the two telescopes that have the MOS cameras in the focus, about half of the X-ray light is utilised by the reflection grating spectrometers (RGSs). Each RGS consists of an array of reflection gratings that diffracts the X-rays to an array of dedicated

CCD detectors (see Brinkman et al. 1998 [44]; den Herder et al. 2001 [**?**]). During the observation, MOS1 and MOS2 camera were operated in fast uncompressed mode and small window mode, respectively. The EPIC-pn camera was operated in timing mode with a medium filter during the observation. The faster CCD readout results in a much higher count rate capability of 800 cts/s before charge pile-up become a serious problem for point-like sources. The EPIC-pn count rate of the source was around 55 cts/s, thereby avoiding telemetry and pile-up problems. Although the RGS and EPIC-pn data products were extracted and analysed by Iaria et al. (2013) [38], we extracted the data products of the RGS and EPIC-pn camera again using the very recent science analysis software (SAS) version 13.5.0 and the calibration files available on 2013 Dec.17. We used the SAS tools `rgsproc`, `emproc`, and `epproc` to obtain the RGS, MOS, and EPIC-pn data products. Since the EPIC-pn was operated in timing mode during the observation, we extracted the EPIC-pn image of RAWX vs.PI to select appropriately the source and background region. The source spectrum is selected from a box region centred on RAWX = 38 with a width of 18 columns. The background spectrum was selected from a box region centred on RAWX = 5 with a width of two columns. We extracted only single and double events (patterns 0 to 4) for the source and background spectra and applied the SAS tool `backscale` to calculate the different areas of the source and background regions. We extracted the MOS1 source spectrum, adopting a box region centred on RAWX = 317 having a width of 50 pixels. The MOS1 background spectrum is extracted from a source-free region selected in one of the outer CCDs that collect photons in imaging mode during the observation. We extracted the MOS1 spectrum and the corresponding redistribution matrix and ancillary files using the standard recipe [6]. We also extracted the source+background light curve, observing that the average count rate during the observation is 15 c/s. The MOS2 source spectrum was extracted from a circular region centred on the pixel showing the largest number of photons; the radius of the region is 640 pixels. A circle with radius of 640 pixels was placed in a source-free region to extract the background spectrum. We extracted the MOS2 spectrum and the corresponding redistribution matrix and ancillary files using the standard recipe [7]. We also extracted the background-subtracted light curve using the SAS tool `Epiclccorr`, and the average count rate is 15 c/s. Since

[6] see: http://xmm.esac.esa.int/sas/current/documentation/threads/MOS_spectrum_timing_thread.shtml
[7] see: http://xmm.esac.esa.int/sas/current/documentation/threads/MOS_spectrum_thread.shtml

the count-rate limit for avoiding pile-up for the MOS cameras is 100 c/s and 5 c/s for a point-like source in timing uncompressed and small window modes [8], respectively, we expect that the pile-up effects are present in the MOS2 spectrum. The RGS1, RGS2, MOS1, MOS2, and EPIC-pn spectra have an exposure time of 53, 51, 51, 51, and 51 ks, respectively.

3.3.3 The INTEGRAL observation

The INTErnational Gamma-Ray Astrophysics Laboratory (INTEGRAL Winkler et al., 2003 [45]) has repeatedly observed the X1822-371 region. We searched the whole IBIS (Ubertini et al., 2003 [46]) and JEM-X (Lund et al., 2003 [47]) public catalogues, selecting only pointings (science windows, SCW) with sources within six degrees of the centre of the field of view and with exposures longer than 500 s to reduce the calibration uncertainties of the IBIS/ISGRI (Lebrun et al., 2003 [48]) spectral response. The available IBIS data set covers the period starting from 2003 March 21 until 2013 March 21 for a total usable on-source time of 1271 ks and an effective dead-time corrected exposure of 874 ks. Because of the smaller field of view, the total exposure of JEM-X1 (camera 1) is 330 ks, while the dead-time-corrected exposure is 283 ks. The INTEGRAL data analysis uses standard procedures within the offline science analysis software (OSA10.0) distributed by the ISDC (Courvoisier et al., 2003 [49]). In the catalogue used for the extraction of the IBIS spectra, we have included all the sources significantly detected in the total image obtained by mosaicking the individual pointings. We exploited a custom spectral binning optimised in the energy range 20?100 keV, and in the detection of spectral features around 30 keV, weighted the time-evolving response function according to the available data and excluded the data below 21 keV due to the evolving detector?s low threshold. For JEM-X, we adopted the standard 16 bins spectrum provided by the analysis software and excluded the data below 5 keV and above 22 keV, which are affected by calibration uncertainties [9].

[8] see: http://xmm.esac.esa.int/external/xmm_user_support/documentation/uhb_2.1/node28.html

[9] The JEM-X2 unit was active only during a limited part of the mission, so the exposure time is not enough to provide a significant spectral constraint.

3.4 Search for the spin period in the XMM data

We used the EPIC-pn events to search for the spin period. We applied the barycentric correction with respect to the source coordinates, given by Iaria et al. (2011) [31], using the SAS tool `barycen`; subsequently, we corrected the data for the orbital motion of the binary system using the recent X-ray ephemeris of X1822-371 derived by Iaria et al. (2011) [31] (see eq.2 in that work) and the projected semimajor axis $a\sin i$ of 1.006 lt-s (see Table 1 in Jonker & van der Klis, 2001 [29]). We selected the EPIC-pn events in the 2-5.4 keV energy range and explored the period window between 0.592384 and 0.593384 s using the FTOOL `efsearch` in the XRONOS package [10]. We adopted eight phase bins per period (a bin time close to 0.074 s) for the trial folded light curves and a resolution of the period search of $1 \times 10^{-6} s$. We observed a χ^2 peak of 41.89 at 0.592884 s, as shown in Fig.3.1 (see appendix B).

We fitted the peak with a Gaussian function, assumed the centroid of the Gaussian as the best estimation of the spin period, and associated the error derived from the best fit. We find that the spin period during the XMM observation is 0.5928850(6)s, and the associated error is at the 68% confidence level.

Considering that we have seven degrees of freedom, the probability of obtaining a χ^2 value greater than or equal to 41.89 by chance is 5.47×10^{-7}. In our search we adopted 10^3 trials (we span 10^{-3} s with a resolution of the period search of $1 \times 10^{-6} s$), consequently we expect a number of $\simeq 5.5 \times 10^{-4}$ periods with a χ^2-value greater than or equal to 41.89. This implies that our detection is significant at the 99.945% confidence level. Then, we folded the $2 \div 5.4$ keV EPIC-pn light curve using the spin period of 0.5928850(6) s and adopting 16 phase bins per period. We used the arbitrary value of 51 975.85 MJD as epoch of reference. The folded light curve is almost sinusoidal (see Fig.3.2).

Fitting the folded light curve with a constant plus a sinusoidal function with period fixed at one, we obtain a $\chi^2_{d.o.f.}$ of 13.9(13). Since the constant is 23.92(2) c/s, the background count rate is close to 1.3 c/s and the amplitude of the sinusoidal function 0.17(3) c/s, we estimate that the pulse fraction is 0.75 ± 0.13 % compatible within 3σ to the value of 0.25 ± 0.06% reported by Jonker& van der Klis (2001) [29] using RXTE/PCA data in the same energy band.

We report in Table 3.1 the 13 values of the spin period of X1822-371 and the

[10] see: http://heasarc.gsfc.nasa.gov/ftools/xronos.html

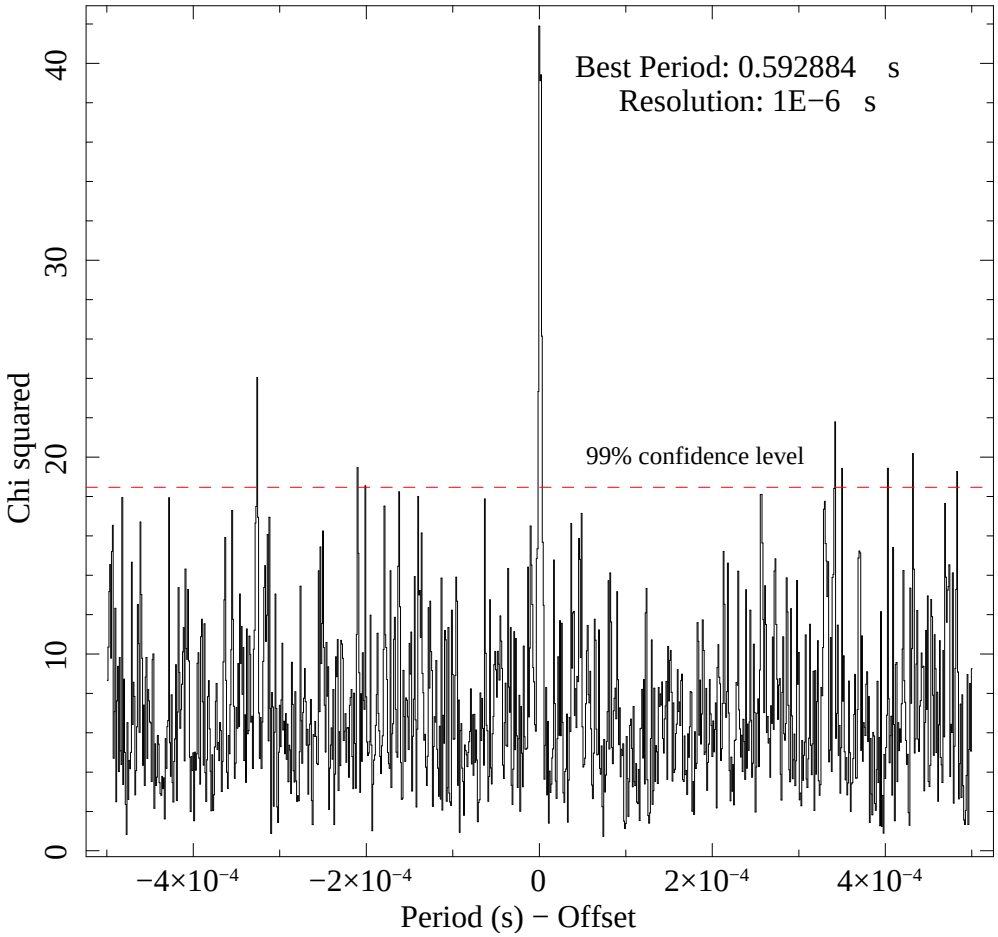

Figure 3.1: Folding search for periodicities in the $2 \div 5.4$ keV EPIC-pn light curve. We adopt 8 phase bins per period for the trial-folded light curves and a resolution of period search of $1 \times 10^{-6} s$. The peak of χ^2 is detected at 0.592884 s. The horizontal dashed line indicate the χ^2 value of 18.47 at which we have the 99% confidence level for a single trial.

corresponding errors previously estimated, together with the value found in the present work. The corresponding times are the mean values between the start and stop time of the observations in which the spin period was detected, the associated errors are one half of the duration of the corresponding observation. After deriving the geometric mean of the times in Table 3.1 (Col. 1) obtaining $T_{mid} = 52,257.78 MJD$, we fitted the spin periods with respect to the times with T_{mid} subtracted using a linear function to estimate the spin period derivative.

Unlike Jain et al. (2010) [30], we did not obtain a good fit, since the $\chi^2_{d.o.f.}$ was close to $10^5(12)$; however, we obtained a very high value of -0.9992 of the Pearson

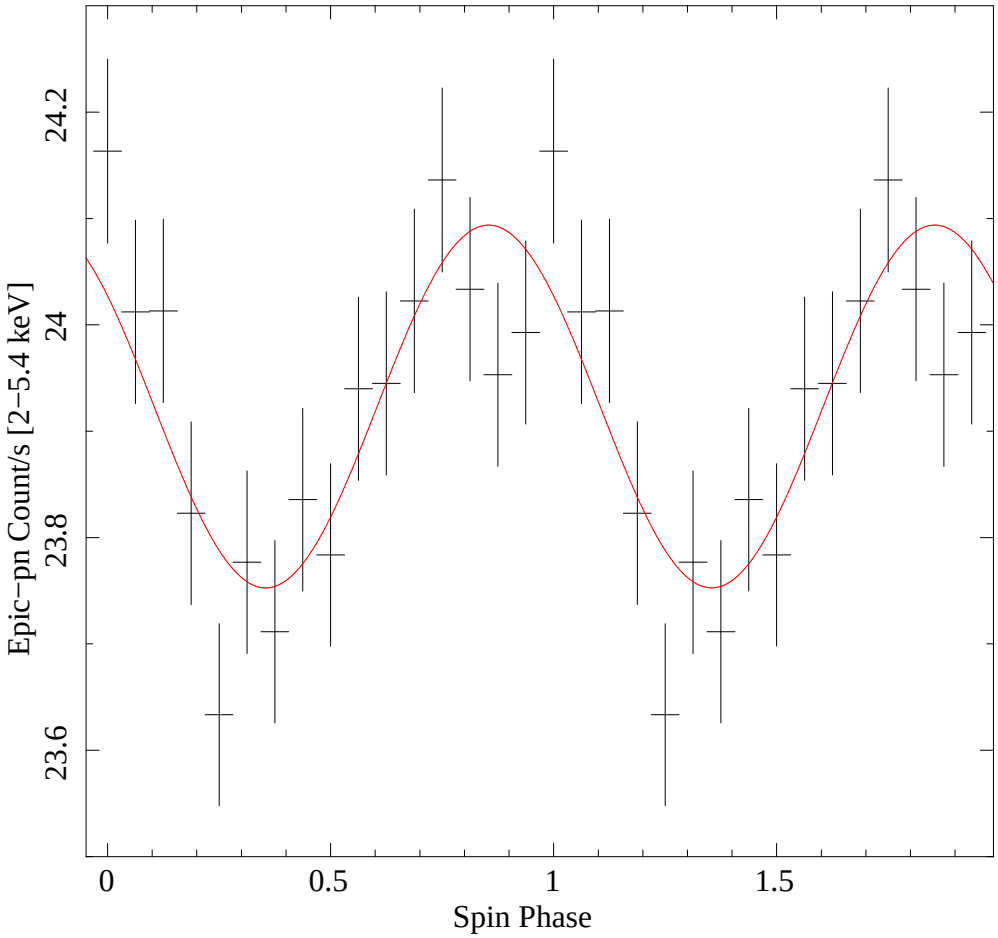

Figure 3.2: EPIC-pn folded light curves of X1822-371 using the folding period 0.5928850(6) s. The folded light curve is obtained using 16 phase bins per period.

correlation coefficient. The reason for the high χ^2 value is not clear to us, but it could be due to an underestimation of the errors (e.g. small differences in the orbital ephemeris used to correct the data) or model complications (e.g. caused by small fluctuations around an average linear trend), or other issues. The detailed investigation of this aspect goes beyond the aim of this thesis. Considering the high value of the χ^2 for the linear fit and to estimate the error associated to the spin period derivative, we fitted the 14 points without the estimated errors and attributed the post-fit errors to the best-fit parameters under the assumption that the model is reliable. In this way we at least get an estimation of the averaged linear trend of the measured spin period with respect to time. Fitting the data again with a linear function, we obtain $a = 0.592826(6)s$ and $b = -2.20(3) \times 10^{-7} s/d$, with the errors at 68% confidence level. This implies that

Times (MJD)	Spin period (s)	Ref.
50352.9(6)	0.59325(2)	1
50,993.4(6)	0.59308615(5)	1
51975.9(3)	0.5928850(6)	2
51976.04(6)	0.59290132(11)	3
52094.80(6)	0.59286109(8)	3
52095.73(6)	0.59286421(12)	3
52432.62(18)	0.5927922(13)	3
52489.7(9)	0.5927790(6)	3
52491.61(15)	0.5927795(11)	3
52503.45(12)	0.5927737(10)	3
52519.41(18)	0.5927721(8)	3
52882.15(9)	0.5926793(15)	3
52883.15(9)	0.5926852(21)	3
54010.0(6)	0.5924337(10)	4

Table 3.1: Times and corresponding. (**References**:1 Jonker& van der Klis (2001)[29], 2 this work, 3 Jain et al. (2010) [30] e Sasano et al. (2014) [39]).

the spin period derivative, $\dot{P}_s$, is $-2.55(3) \times 10^{-12} s/s$; this is compatible within three sigmas with the previously reported values of $-2.481(4) \times 10^{-12} s/s$ and $-2.43(5) \times 10^{-12} s/s$ given by Jain et al.(2010) [30] and Sasano et al. (2014)[39], respectively. We show in Fig.3.3 (top panel) the 14 points and the corresponding linear best fit. The corresponding residuals are shown in Fig.3.3 (bottom panel).

Furthermore, we search for the same periodicity in the MOS1 data (taken in *timing* mode); unfortunately, the lower statistics with respect to the EPIC-pn data do not allow us to detect the periodicity in this data set. We note that the spin period obtained from the EPIC-pn events is inconsistent with the value reported by Jain et al.(2010)[30] using RXTE/PCA observations simultaneous to the XMM observation that we analyse in this work (see Table 3.1 and Fig.3.3). To confirm the robustness of our results, we reanalysed the simultaneuous RXTE/PCA observations (P50048-01-01-00, 50048-01-01-01, P50048-01-01-02, P50048-01-01-03, P50048-01-01-04, P50048-01-01-05, P50048-01-01-06) spanning 2001 March 7 10:29:26 UT to 2001 March 8 4:47:44 UT. We applied the

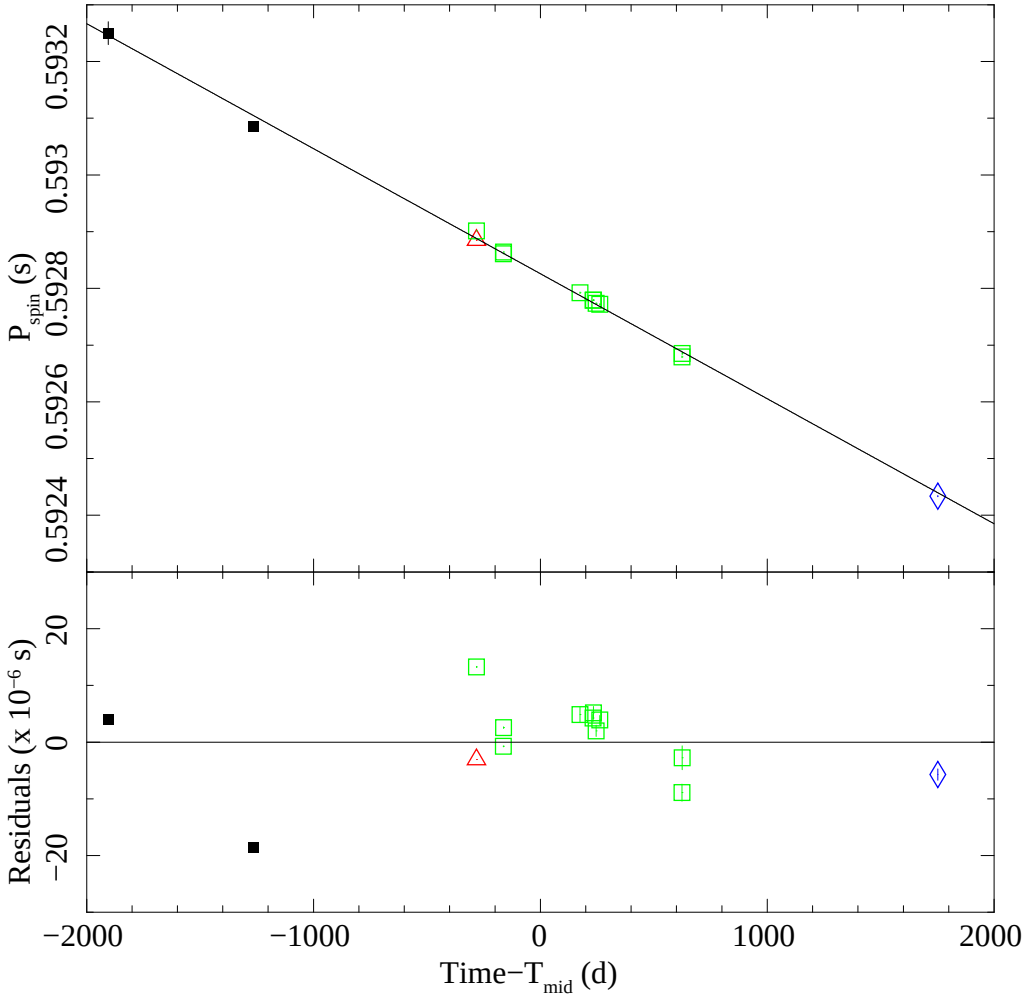

Figure 3.3: *Top panel*: spin period values shown in Table 3.1 vs. time in units of days (see the text). The linear best fit is also plotted. The black squares, open green squares, blue diamond, and red triangle indicate the spin period values reported by Jonker & van der Klis (2001)[29], Jain et al. (2010)[30], Sasano et al.(2014)[39], and this work, respectively. *Bottom panel*: the corresponding residuals in units of $10^{-6}s$.

barycentric correction with respect to the source coordinates and corrected the data for the orbital motion of the binary system as done for the EPIC-pn data. No energy selection was applied to the RXTE/PCA events file. We explored the period window between 0.592384 and 0.593384 s using the FTOOL `efsearch` in the XRONOS package. We adopted eight phase bins per period for the trial-folded light curves and a resolution of the period search of $1 \times 10^{-6}s$. We observe a χ^2 peak of 150 at 0.592884 s, as shown in Fig.3.4.

We fitted the peak with a Gaussian function, assumed the centroid of the

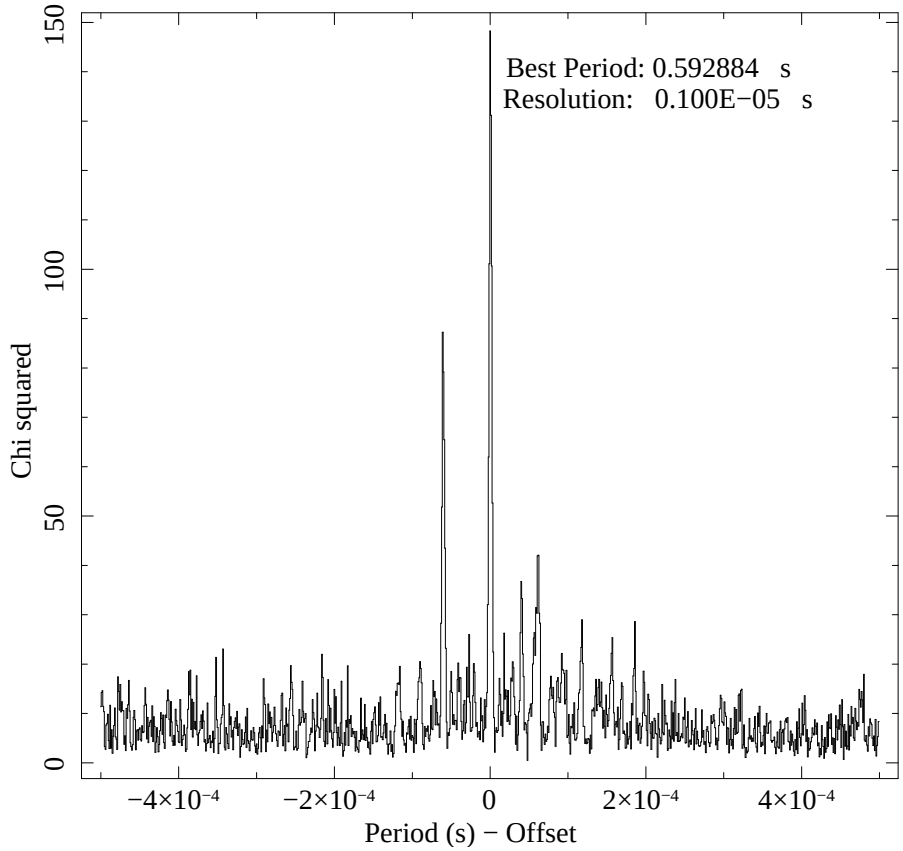

Figure 3.4: Folding search for periodicities in the RXTE/PCA observations. The peak of χ^2 is detected at 0.592884 s.

Gaussian as the best estimation of the spin period, and associated the error derived from the best fit. We find that the spin period during the RXTE/PCA observations is 0.5928846(3) s and that the associated error is at the 68% confidence level. This result confirms our detection in the XMM/Epic-pn data. Finally, we note that the value of the spin period derivative obtained above does not significantly change when using our value instead of the one reported in Table 3.1.

3.5 Energy range selection for the XMM-Newton, Suzaku, Chandra, and INTEGRAL spectra

We rebinned the MOS1 and MOS2 spectra using the SAS tool `specgroup` to have at least 25 counts per energy channel and with an over-sample factor of 5.

To verify that the spectra are similar and see how the pile-up effects influence the MOS2 spectrum, we fitted the two MOS spectra in the 0.6-10 keV energy range using XSPEC (version 12.8.1). We adopted a very simple model consisting of `phabs*pcfabs*CompTT`, similar to the model used by Iaria et al. (2001)[37] to fit the BeppoSAX broad-band spectrum of X1822-371. The `phabs` component takes the photoelectric absorption by the interstellar neutral mat- ter into account, it is a multiplicative component defined as $M(E) = exp[-N_H * \sigma(E)]$, where $\sigma(E)$ is the photo-electric cross-section (not including Thomson scattering). The free parameter, N_H, is the equivalent hydrogen column density in units of $10^{22} atoms\, cm^{-2}$. The `pcfabs` component takes the photoelectric absorption into account owing to the neutral matter near the source, and it is a multiplicative component defined as $M(E) = f * exp[-N_H * \sigma(E)] + (1 - f)$, where N_H and f is a dimensionless free parameter ranging between 0 and 1 that takes the fraction of emitting region occulted by the local neutral matter into account.

The `CompTT` component (Titarchuk, 1994 [50]) is a Comptonisation model of soft photons in a hot plasma. For this component, the soft photon input spectrum is a Wien law with a seed-photon temperature, KT_0 that is a free parameter. The other free parameters of the component are the plasma temperature, KT_e, the plasma optical depth τ, and the normalisation N_{CompTT}. We used a slab geometry for the Comptonising cloud. We fitted the 0.6-10 keV MOS1 and MOS2 spectra simultaneously with the aim of estimating the pile-up effects in the MOS2 spectrum. We obtained a large $\chi^2_{d.o.f.}$ of 1716(540). The two spectra are consistent with each other between 0.6 and 7 keV. Above 7 keV the pile-up distortion is evident in the MOS2 spectrum. Furthermore, the presence of two emission lines in the residuals at 6.4 and 6.97 keV is evident; finally, both the spectra are not well fitted between 0.6 and 1 keV and show large residuals. We show the MOS1 and MOS2 residuals in Fig.3.5.

We sum the MOS1 and MOS2 spectra using a new recipe [11]. In the following the summed spectrum is called MOS12 spectrum. The MOS12 spectrum is rebinned with an over-sample factor of 5. We added the first-order spectrum of RGS1 and RGS2 together using the SAS tool `rgscombine`; hereafter, the summed spectrum is called RGS12. We rebinned the RGS12 to have at least 200 counts per energy channel. In the following, we analyse the RGS12 spectrum in the

[11] see: http://xmm.esac.esa.int/sas/current/documentation/threads/Epic_merging.shtml

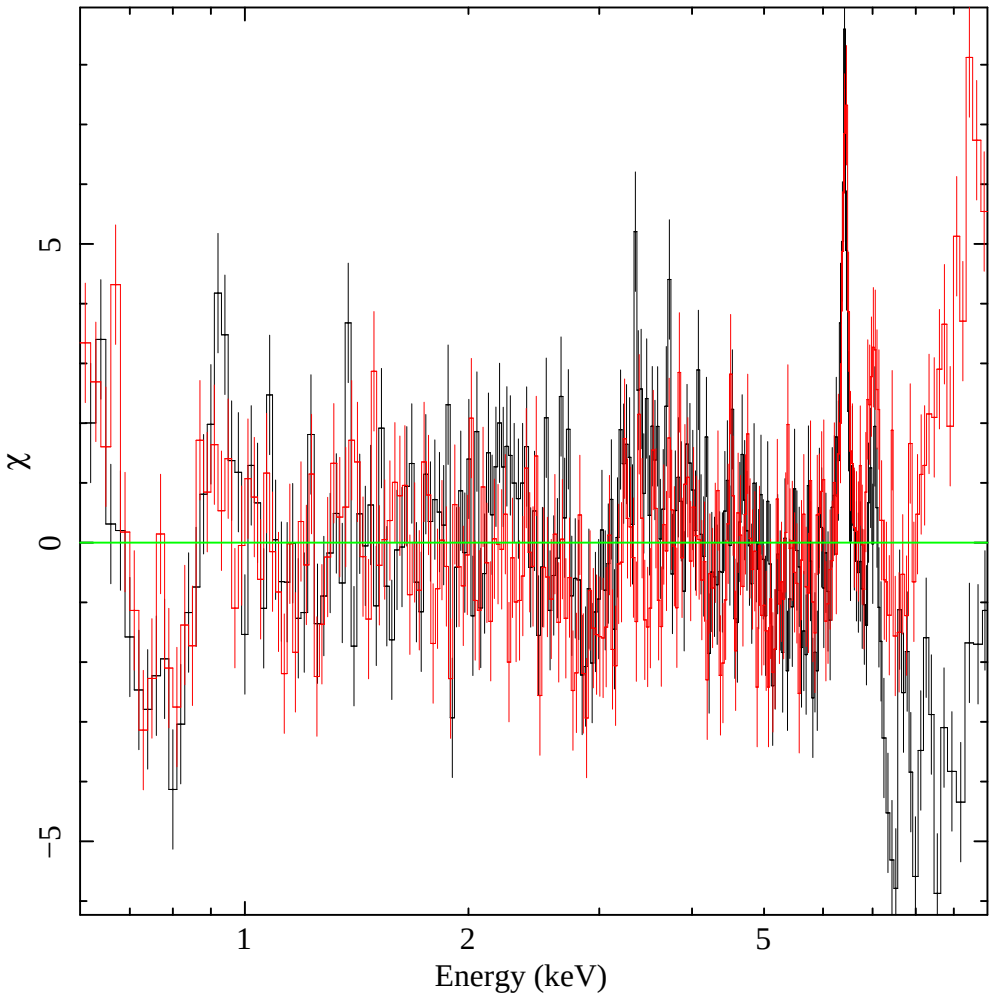

Figure 3.5: MOS1 (black) and MOS2 (red) residuals with respect to the model described in the text.

0.35-2 keV energy range. The EPIC-pn spectrum is rebinned using the SAS tool `specgroup` imposing at least 25 counts per energy channel and an over-sample factor of 5. To check the consistency of the EPIC-pn and MOS12 spectra, we fit them simultaneously adopting the same model described above. We obtain a large $\chi^2_{d.o.f.}$ value of 3228(466). We show the two spectra (MOS12 and EPIC-pn spectra) and the corresponding ratio (data/model) in Fig.3.6.

We observe a large absorption feature in both spectra at 0.7 keV. A mismatch between the two spectra is evident below 1.5 keV; the EPIC-pn residuals show an instrumental feature at 2.2 keV owing to the neutral gold M-edge. Finally, we detect the presence of strong emission lines in the Fe-K region. The causes of the mismatch between the EPIC-pn and MOS12 are not clear. However, we note

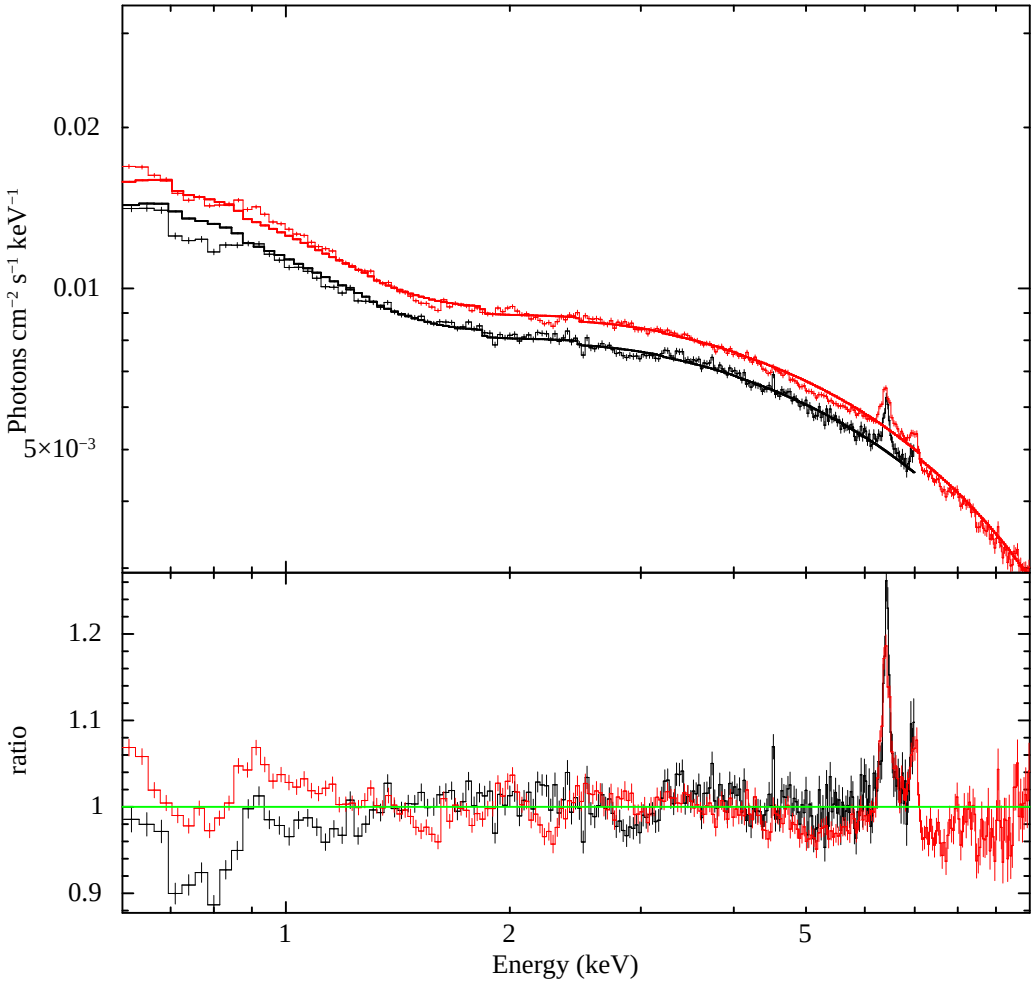

Figure 3.6: MOS12 (0.6?7 keV; black) and EPIC-pn (0.6?10 keV; red) spectra (*top panel*) and ratio (data/model; *bottom panel*) with respect to the model described in the text.

that the residuals close to 0.7 keV are present in both the EPIC-pn and MOS12 spectra (see Fig.3.6, lower panel). We adopt the 0.6-10 keV energy range for the EPIC-pn spectrum. To fit the instrumental feature at 2.2 keV in the EPIC-pn spectrum, we use an absorption Gaussian line with the centroid and the width fixed at 2.3 and 0 keV, respectively. We fit MOS12 spectrum using the 0.6-7 keV or the 1.5-7 keV energy band. For the Suzaku/XIS data, we adopt a 0.5-10 keV energy range for the XIS0+XIS2+XIS3 (hereafter XIS023) and XIS1 spectra. We exclude the energy interval between 1.7 and 2.4 keV in the XIS023 and XIS1, because of systematic features associated with neutral silicon and neutral gold edges. We group the HXD/PIN spectrum to have 25 photons per chan-

nel and use the energy range between 15 and 36 keV. We show in Fig.3.7 the HXD/PIN source spectrum and the summed HXD/PIN NXB and CXB spectra (hereafter NXB+CXB spectrum). The NXB+CXB spectrum dominates the source spectrum at energies higher than 36 keV. We analyse the Chandra/MEG in the 0.5-7 keV energy range. Finally, we analyse the JEM-X and IBIS spectrum in the 5-22 and 21-60 keV energy band, respectively. The IBIS spectrum is background-dominated above 60 keV.

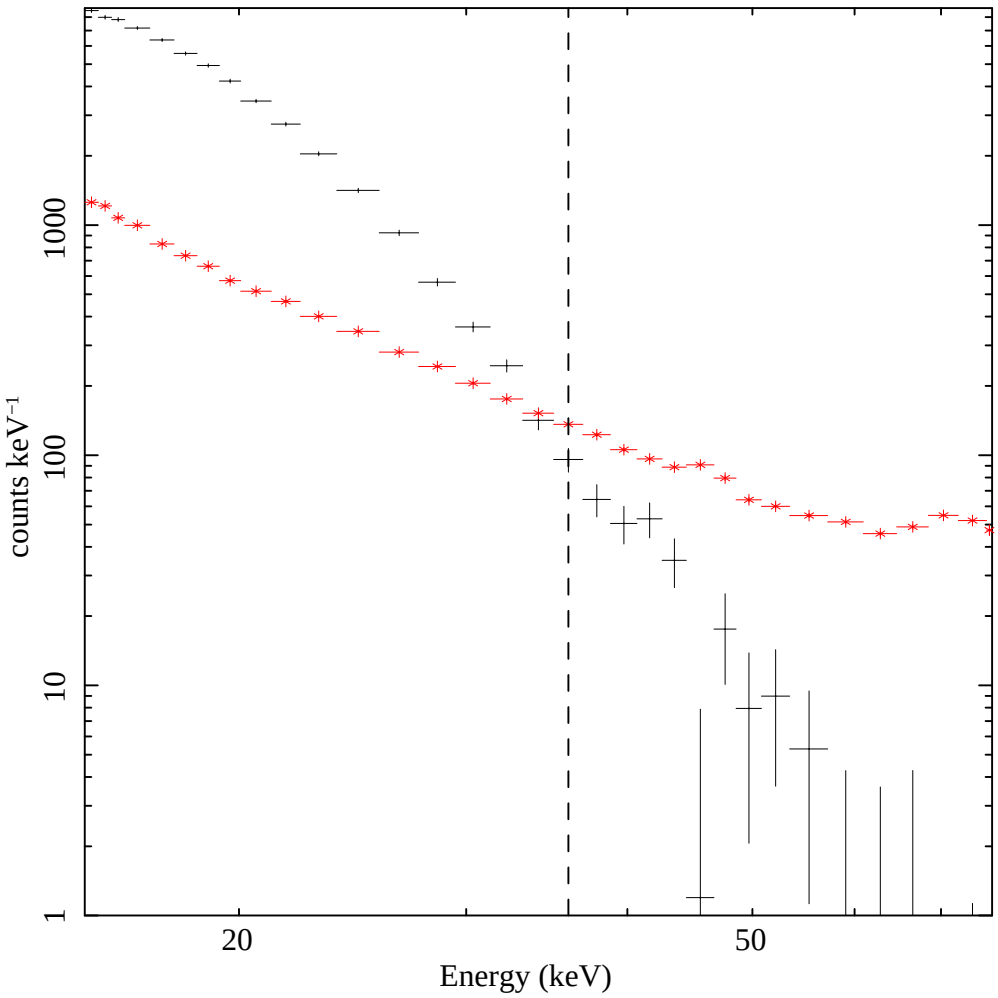

Figure 3.7: HXD/PIN source spectrum (black) and NXB+CXB spectrum (red) are shown. The NXB+CXB spectrum overwhelms the source spectrum at energies larger than 36 keV, the energy threshold is indicated with a dashed vertical line.

3.6 Spectral analysis

We simultaneously fitted the XMM-Newton, Suzaku, Chandra and INTEGRAL spectra. We added a systematic error of 1% to take into account that the observations are not simultaneous. Initially, we fitted spectra using 0.6-7 keV energy range for the MOS12. We fitted the spectra using XSPEC version 12.8.1 (see Arnaud, 1996 [51]). Initially, to fit the continuum emission, we adopted the model used by da Iaria et al. (2013) [38].
It is `Ed*phabs*(f*cabs*phabs*(LN+CompTT)+(1-f)*(LN+CompTT))`, which is a Comptonised component (`CompTT` in XSPEC) absorbed by neutral interstellar matter (the first `phabs` component) and partially absorbed by local neutral matter (the second `phabs` component). We used the abundances provided by Asplund et al. (2009) [52] and the photoelectic cross section given by Verner et al. (1996)[53]. We took the Thomson scattering of the local neutral matter into account by adding the cabs component and imposed that the equivalent hydrogen column density of the `cabs` component is the same as the local neutral matter. The constant `f` gives the percentage of emitting region occulted by the local neutral matter. Finally, `LN` and `Ed` in the model indicate all the Gaussian components added to the model to fit the several emission lines observed in the spectrum and the added absorption edges, respectively.

Since the XMM-Newton, Suzaku, Chandra, and INTEGRAL observations are not simultaneous we left the values of the electron temperature and of the optical depth of the CompTT component free to vary independently. The depths of the absorption edges added above 7 keV were free to vary independently for the XMM-Newton, Suzaku, and INTEGRAL spectra, whilst they were tied in the Chandra spectrum to the values of the XMM-Newton spectrum because the Chandra spectrum extends up to 7 keV. Several emission lines are detected and identified with N_{VII}, O_{VII} intercombination line, O_{VIII}, Ne_{IX} intercombination line, Ne_X, Mg_{XI} intercombination line $Mg_{XII}, Si_{XIV}, Fe_I eFe_{XXVI}$. The emission lines are fitted with Gaussian components. We fixed the energies and widths of the emission lines below 6 keV at their best-fit values because their analysis is not the aim of this work; a detailed analysis of these lines is reported by Iaria et al. (2013)[38]. Finally, we added two absorption edges at 7.2 and 8.4 keV. Fitting the spectra we obtain a $\chi^2_{d.o.f.}$ of 3024(2496) and large residuals between 0.35 and 1 keV are visible. We show the residuals in Fig.3.8 (top panel), the

best-fit values of the continuum emission and absorption edges in Table 3.2, and the best-fit parameters associated with the emission lines in Table 3.3.

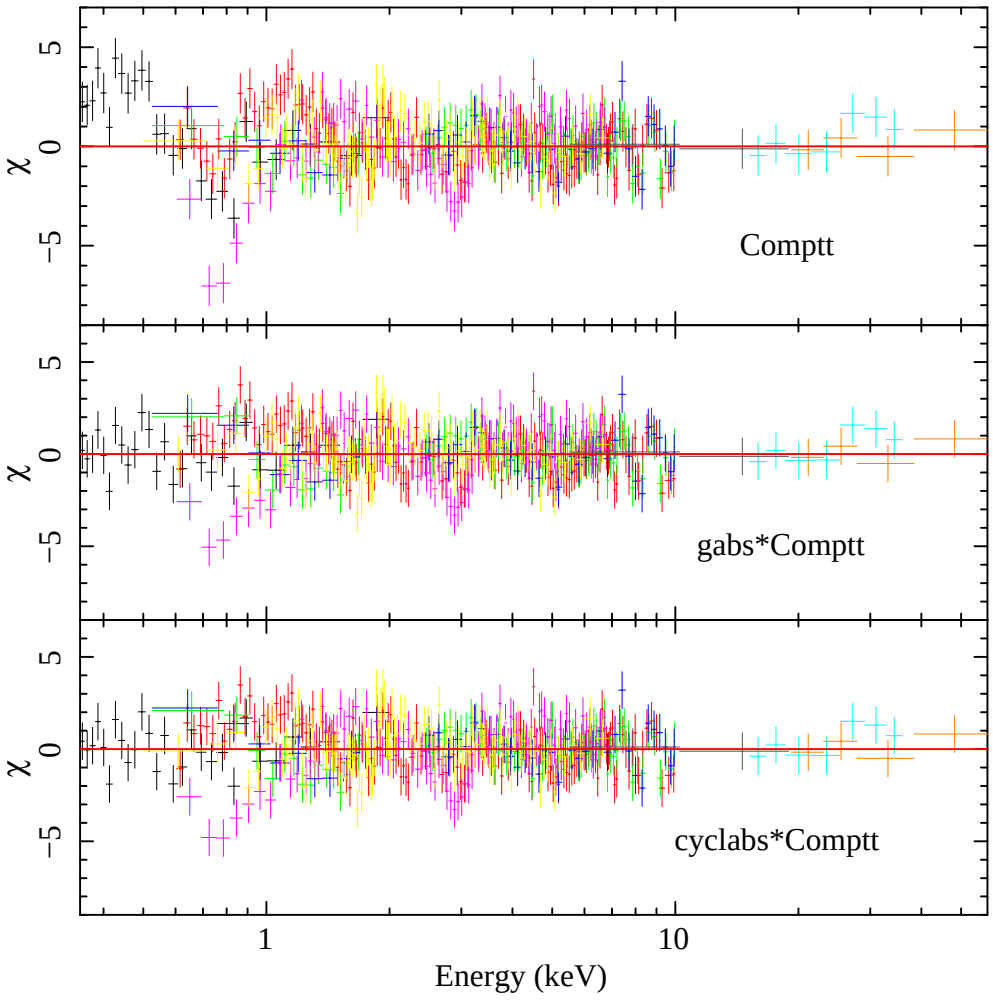

Figure 3.8: Residuals with respect to the best-fit models shown in Tables 3.2 and 3.3. The RGS12, EPIC-pn, XIS023, XIS1, MOS12, HXD/PIN, MEG, JEM-X, and IBIS spectra are shown in black, red, green, blue, magenta, light-blue, yellow, grey, and orange, respectively. The data are graphically rebinned. From top to bottom, the residuals with respect to the continuum consist of: 1) a `Comptt` partially absorbed by local neutral matter (large residuals are evident at 0.7 keV); 2) `gabs*Comptt` with the energy of the `gabs` component close to 0.73 keV; 3) `cyclabs*Comptt`.The MOS12 spectrum covers the $0.6 \div 7$ keV energy band.

To fit the large residuals between 0.4 and 1 keV, we added a Gaussian absorption line (`gabs` in XSPEC) that is a multiplicative component. The component `gabs` is defined by three parameters, and its functional form is

$$M(E) = exp[-(\tau/\sqrt{2\pi\sigma})exp(-((E - E_0)/4\sigma)^2)]$$

where τ, σ e E_0 are the line depth, the line width in keV, and the line energy in keV, respectively. We interpret this component as a CRSF in the spectrum. The model becomes : `Ed*phabs*(f*cabs*phabs*(LN+gC)+(1-f)*(LN+gC))`, where `gC` is `gabs*CompTT` and `Ed` takes the absorption edges into account. The addition of the `gabs` component improves the fit. We obtain a $\chi^2_{(d.o.f.)}$ of 2798(2493) with a $\delta\chi^2$ of 226 and a *F-statistics* of 67.1. The residuals are shown in Fig.3.8 (the second panel from the top). The best-fit parametes are shown in Tables 3.2 and 3.3.

We also fitted the residuals between 0.4 and 1 keV using, instead of a Gaussian absorption line, an absorption line with a Lorentzian shape (Mihara et al., 1990 [54]). This multiplicative component (`cyclabs` in XSPEC) is defined by three parameters, and its functional form is:

$$M(E) = exp[-\tau(\sigma E/E_0)^2/[(E - E_0)^2 + \sigma^2]]$$

where τ, σ and E_0 are the line depth, the line width in keV, and the line peak energy in keV, respectively. We fixed the second harmonic depth to zero in the model. In this case the adopted model is:
`Ed*phabs*(f*cabs*phabs*(LN+cC)+(1-f)*(LN+cC))`, where `cC` is the component `cyclabs*CompTT`. The addition of the `cyclabs` component instead of the `gabs` component gives an equivalent fit with a $\chi^2_{(d.o.f.)}$ of 2795(2493). The best-fit values are shown in Tables 3.2 and 3.3. The residuals are shown in Fig.3.8 (bottom panel).

The residuals in Fig.3.8 show that the RGS12, XIS1, XIS023, MEG, and EPIC-pn spectra are in good agreement below 1.5 keV, unlike in the MOS12 spectrum. For this reason we repeated the analysis described above excluding the $0.6 \div 1.5$ keV energy range in the MOS12 spectrum. Fitting the spectra using the initial model, we find a $\chi^2_{(d.o.f.)}$ of 2713(2466) and large residuals between 0.35 and 1 keV are visible (see Fig.3.9, top panel).

Using the model that includes the `gabs` component, we obtain a $\chi^2_{(d.o.f.)}$ of 2565(2463) with a $\delta\chi^2$ of 148 and a F-statistics value of 47.4. The residuals are shown in Fig.3.9 (middle panel). Using the model including the `cyclabs` component, we obtain a $\chi^2_{(d.o.f.)}$ of 2565(2463). The residuals are shown in Fig.3.9

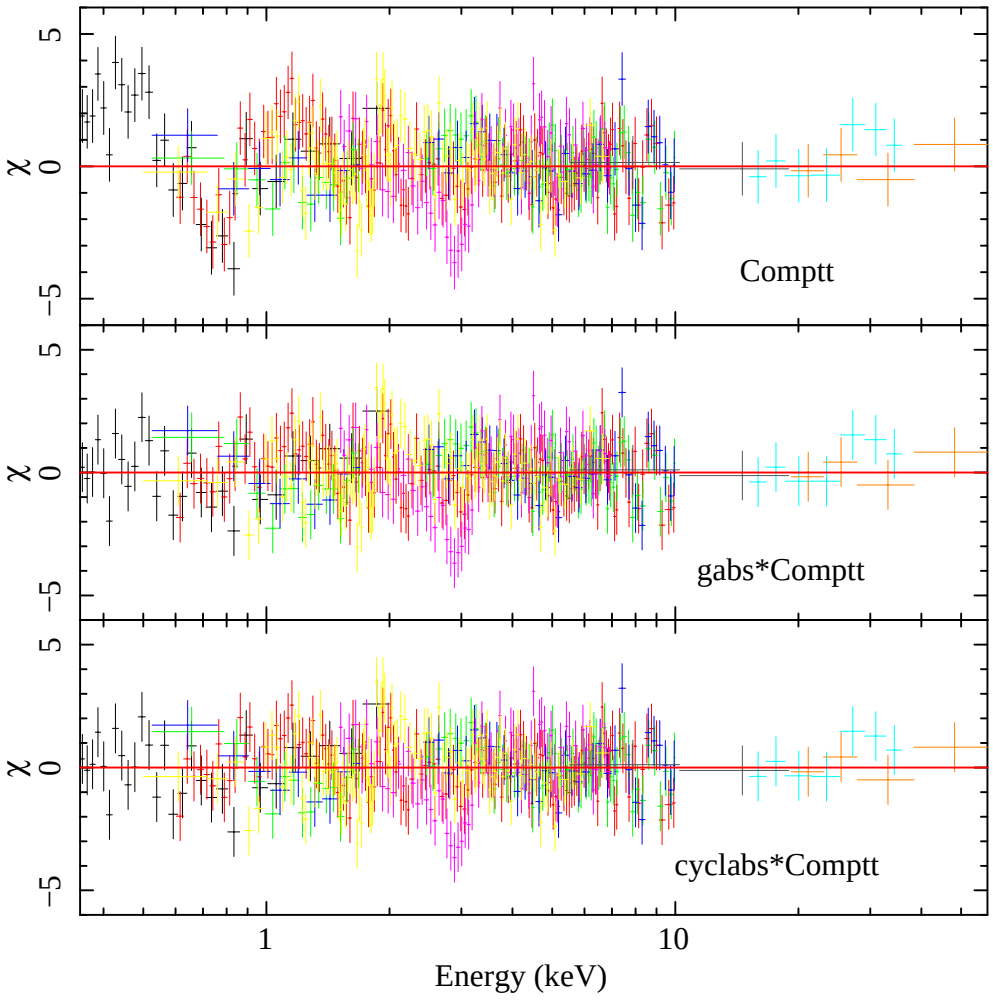

Figure 3.9: Residuals with respect to the best-fit models shown in Tables 3.2 and 3.3. The colours are defined as in other figures. The data are graphically rebinned. From top to bottom, the residuals with respect to the continuum consist of: 1) a `Comptt` partially absorbed by local neutral matter (large residuals are evident at 0.7 keV); 2) `gabs*Comptt` with the energy of the `gabs` component close to 0.72 keV; 3) `cyclabs*Comptt`. The MOS12 spectrum covers the $1.5 \div 7$ keV energy band.

(bottom panel). The unfolded spectra relative to the model including the `gabs` component is shown in Fig.3.10. We show the data/model ratio with respect to the best-fit model, but excluding the `gabs` component in Fig.4.1.

Furthermore, using the initial model with the MOS12 spectrum between $1.5 \div 7$ keV, we look for the presence of CRSF at high energies, as suggested by Sasano et al. (2014)[39], exploiting the availability of the JEM-X and IBIS spectra. Adding to the model a `cyclabs` component with width and centroid fixed to 5 keV and

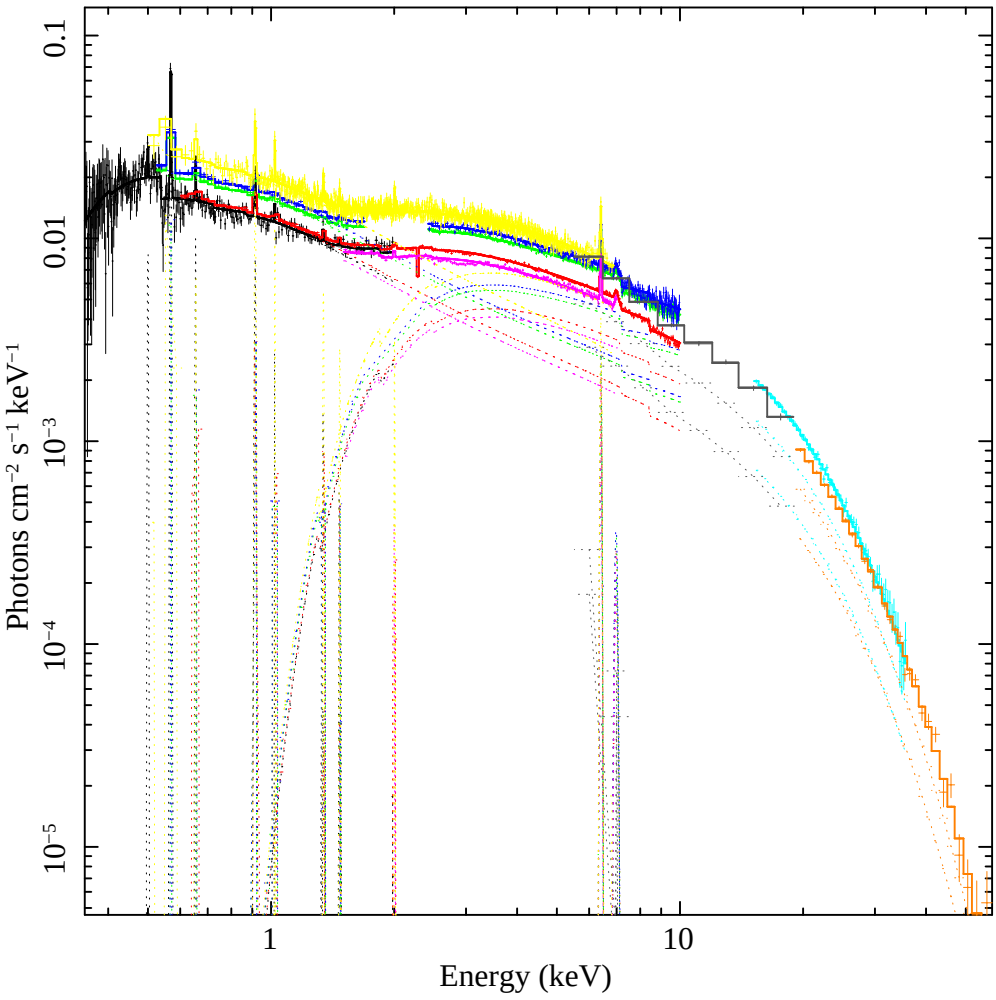

Figure 3.10: Unfolded spectra relative to the model including the `gabs` component. The MOS12 spectrum ranges between 1.5 and 7 keV. Colours as above.

33 keV (see Sasano et al., 2014 [39]), respectively, we find an upper limit on the depth of 0.10 at 99.7% confidence level (3σ). This value is not consistent with the $0.4^{+0.2}_{-0.1}$ obtained by Sasano et al. (2014 [39]).

We find that the energy and width of the CRSF at 0.7 keV are consistent for the Lorentzian and the Gaussian shapes. The depth values of the absorption edges at 7.2 keV are compatible for the XMM-Newton and INTEGRAL spectra, while they are higher in the Suzaku spectrum. Finally, the optical depth of the 0.1 Comptonised component assumes similar values close to nine in the XMM-Newton, Chandra, and Suzaku spectra, while it is 6.0 ± 0.2 in the INTEGRAL spectrum. Finally, we note that including MOS12 spectrum between 0.6 and 1.5

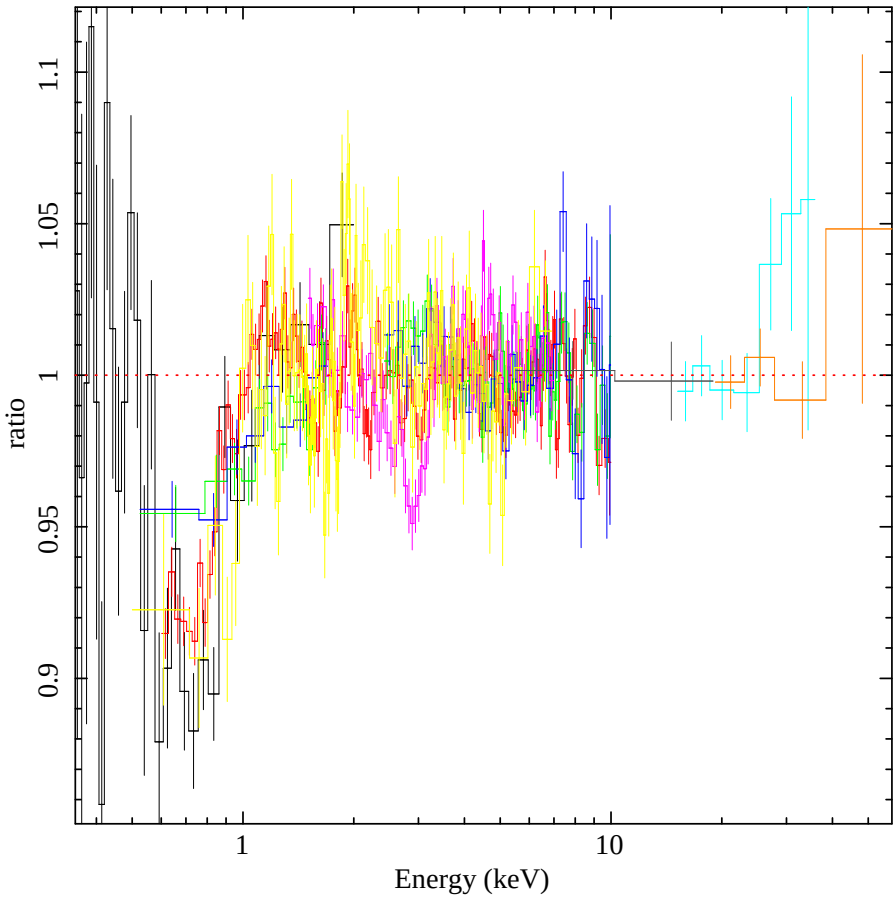

Figure 3.11: Data/model ratio with respect to the best-fit model shown in Tables 3.2 and 3.3, but excluding the `gabs` component. The data are graphically rebinned. Colours as above. The MOS12 spectrum ranges between 1.5 and 7 keV.

keV only marginally affects the fit results. In the following we use the best-fit values obtained when excluding the 0.6-1.5 keV energy range of MOS12.

3.7 Discussion

We used three non-simultaneous pointed X-ray observations of X1822-371: a XMM-Newton observation (using RGS, MOS, and EPIC-pn spectra), a Suzaku observation (using XIS and HXD/PIN spectra), and finally, a Chandra observation (using the first-order MEG spectrum). Moreover, we used all the available INTEGRAL/JEM-X and INTEGRAL/ISGRI observations of X1822-371 and extracted the corresponding spectra to confirm or disprove a claimed CRSF at 33

keV in the Suzaku/PIN spectrum (see Sasano et al. 2014)[39] [12]. We adopted the same model as proposed by those authors to fit the continuum emission (see chapter 3.6). Iaria et al. (2013) found residuals in the EPIC-pn data between 0.6 and 0.8 keV and added a black-body component with temperature fixed to 0.06 keV, thereby improving the fit significantly. In this work we give a different interpretation of the residuals in the EPIC-pn data between 0.4 and 1 keV, modelling them with the addition of a CRSF close to 0.7 keV. The interpretation of residuals as a CRSF in the spectrum allows us to refine the scenario proposed by Iaria et al. (2013) [38] for X1822-371. The authors suggested that the Comptonised component originates in the inner region of the system, it is not directly observable because of the large inclination angle of the system, and only 1% of its flux arrives to the observer because of scattering by an extended optically thin corona with optical depth ~ 0.01. We now suggest that the Comptonised component could be produced in the accretion column onto the NS magnetic caps.

Our results show that a CRSF at 0.7 keV agrees with the non-conservative mass transfer scenario proposed for X1822-371 in the past three years by several authors (see, for example, Iaria et al.(2013 e 2011) [38] e [31]; Burderi et al.(2010) [32]; Bayless et al.(2010) [33]) and allows the NS mass of the binary system to be between 1.61 $M_{\odot}$ and 2.32 $M_{\odot}$ (Muñoz-Darias et al.(2005)[55]). Burderi et al.(2010) [32], Bayless et al.(2010) [33] e Iaria et al.(2011) [31] found a large orbital period derivative of X1822-371, and Burderi et al. (2010) [32] showed that this indicates that X1822-371 accretes at the Eddington limit and that the rest of the mass transferred by the companion star is expelled from the system.

Adopting the values for P_s e $\dot{P}_s$ derived in Sect.3.4 and assuming that X1822-371 accretes at its Eddington limit, we show that the CRSF energy obtained by our fits is consistent with a scenario in which the NS in X1822-371 is spinning up. Since $\dot{P}_s$ is negative, the corotation radius r_c, the radius at which the accretion disc has the same angular velocity as the NS, has to be larger than the magnetospheric radius r_m , the radius at which the magnetic pressure of the NS B-field equals the ram pressure of the accreting matter (see chapter 1.4.3). The corotation radius can be expressed as:

$$r_c = (GM_{NS}/4\pi^2)^{1/3} P_s^{2/3}$$

[12] See the paper for details 3

where M_{NS} is the NS mass and P_s is the NS spin period. Assuming a NS mass of $1.44M_\odot$, we obtain $r_c \simeq 1180km$; for a NS mass of $2M_\odot$, the corotation radius is $r_c \simeq 1300km$. The magnetospheric radius is given by the relation $r_m = \phi r_A$, where r_A is Alfvén radius and ϕ a constant close to 0.5 (see Ghosh & Lamb, 1991 [56]). We estimate r_A using the Eq. (2) in Burderi et al.,(1998) [57]:

$$r_A = 4.3 \times 10^3 \mu_{30}^{4/7} R_6^{-2/7} L_{37}^{-2/7} \epsilon^{2/7} m^{1/7} km \tag{3.1}$$

where μ_{30} is the magnetic moment in units of $10^{30} G\ cm^3$, R_6 the NS radius in units of $10^6 cm$, L_{37} the luminosity of the system in units of $10^{37} erg\ s^{-1}$, m the NS mass in units of solar masses, and finally, ϵ is the ratio between the luminosity and the total gravitational potential energy released per second by the accreting matter. Adopting the best-fit value of the CRSF energy, E_{keV}, obtained from the `gabs` component, and assuming that this is produced at (or very close to) the NS surface, we estimate the NS B-field using the relation $E_{keV} = (1+z)^{-1} 11.6 B_{12}$, where:

$$(1+z)^{-1} = \left(1 - \frac{2GM_{NS}}{R_{NS}c^2}\right)^{1/2}$$

and B_{12} is the NS B-field in units of $10^{12} G$. We arrange the term $(1+z)^{-1}$ in terms of m and R_6 and obtain:

$$B_{12} = \frac{E_{keV}}{11.6}\left(1 - 0.295\frac{M_{NS}}{R_6}\right)^{-1/2} G \tag{3.2}$$

We assume that the intrinsic luminosity of X1822-371 is the Eddington luminosity, $L = 1.26 \times 10^{38} (M_{NS}/M_\odot) erg\ s^{-1}$, which we rewrite as $L_{37} = 12.6 M_{NS}$, which is the Eddington luminosity in units of $10^{37} erg\ s^{-1}$. Substituting this expression of luminosity and the expression of B_{12} of Eq.3.2 into Eq.3.1 and assuming a NS radius of 10 km, we obtain:

$$r_A = 4.3 \times 10^2 (1 - 0.295 M_{NS})^{-2/7} M_{NS}^{-1/7} km$$

For NS masses of $M_{NS} = 1.4M_\odot$ and $M_{NS} = 2M_\odot$, we obtain $r_A \simeq 490km$ and $r_A \simeq 510km$ respectively. Since $r_m = \phi r_A$, with $\phi \simeq 0.5$ then for a NS mass of $M_{NS} = 1.4M_\odot$ and $M_{NS} = 2M_\odot$, we obtain $r_m \simeq 245km$ and $r_m \simeq 255km$, respectively. This means that, for a NS mass between 1.4-2 $M_\odot$, r_m is always smaller than r_c by a factor five. This implies that the accreting matter gives specific angular momentum to the NS, which increases its angular velocity and

spins it up.

Next we adopt the set of relations shown by Ghosh & Lamb, (1979) [58] (Eqs. from (15) to (18)) to establish a relation for the derivative of the spin period, the spin period, the luminosity, and the NS mass. This set of equations is valid for the fastness parameter $\omega_s = \Omega_s/\Omega_K(r_0) < \omega_{max} \simeq 0.95$, where Ω_s is the NS angular velocity, $\Omega_K(r_0)$ is the Keplerian angular velocity at r_0, and r_0 is the radius that separates the boundary layer from the outer transition zone (see discussion in Ghosh & Lamb, 1979 [58]). Using Eq.3.2 and assuming that the NS accretes at the Eddington limit ($L_{37} = 12.6 M_{NS}$), the parameter Ω_s of the Eq.(16) in Ghosh & Lamb, (1979)[58] becomes:

$$\omega_s \simeq 0.456 \Big(\frac{E_{keV}}{11.6}\Big)^{6/7} \Big(1 - 0.295 \frac{M_{NS}}{R_6}\Big)^{-3/7} R_6^{15/7} M_{NS}^{-5/7} P_s^{-1} \tag{3.3}$$

Using the value of E_{keV} shown in Table 3.2, the spin period value shown in chapther 3.4, and finally, imposing that $R_6 = 1$, we find that ω_s is between 0.063 and 0.083 for M_{NS} between 1 and 3 $M_\odot$. This implies that the values of NS B-field and luminosity satisfy the spin-up condition.

Using Eq. (15) of Ghosh & Lamb (1979)[58], we constrained the NS mass. We adopted the expression of the NS moment of inertia given by Lattimer & Schutz (2005)[59] in Eq. (16) of their work. The expression is valid for many NS equation of states and for a NS mass higher than $1 M_\odot$. Rewriting the expression in terms of M_{NS} and R_6 we obtain:

$$I_{45} \simeq (0.471 \pm 0.016) M_{NS} R_6^2 \Big(1 + 0.42 \frac{M_{NS}}{R_6} + 0.009 \frac{M_{NS}^4}{R_6^4}\Big) \tag{3.4}$$

where I_{45} is the NS moment of inertia in units of $10^{45} g\ cm^2$. The Eq.(15) of Ghosh & Lamb (1979)[58] can be rewritten as:

$$-\dot{P}_{-12} \simeq 29.51 R_6^{-2/7} M_{NS}^{-4/7} B_{12}^{2/7} \delta^{-1} P_s^2 n(\omega_s) \tag{3.5}$$

where $-\dot{P}_{-12}$ is the spin period derivative in units of $10^{-12} s/s$, δ is the term in parenthesis in Eq.3.4, B_{12} is given by Eq.3.2 and, finally, the function $n(\omega_s)$ in its useful approximate expression is (see Eq.10 in Ghosh & Lamb (1979)[58]):

$$n(\omega_s) \sim 1.391 - \omega_s [4.03(1 - \omega_s)^{0.173} - 0.878](1 - \omega_s)^{-1}$$

Initially, we impose that $R_6 = 1$ and find how $\dot{P}_{-12}$ changes in function of M_{NS}. The error associated with $\dot{P}_{-12}$ is mainly due to the term $n(\omega_s)$, that has an accuracy of 5% (see Ghosh & Lamb (1979)[58]); we also take the errors associated with I e E_{keV} into account. We adopt the 1σ error for E_{keV}. We show the values of $\dot{P}_{-12}$ vs. M_{NS} in Fig.3.12.

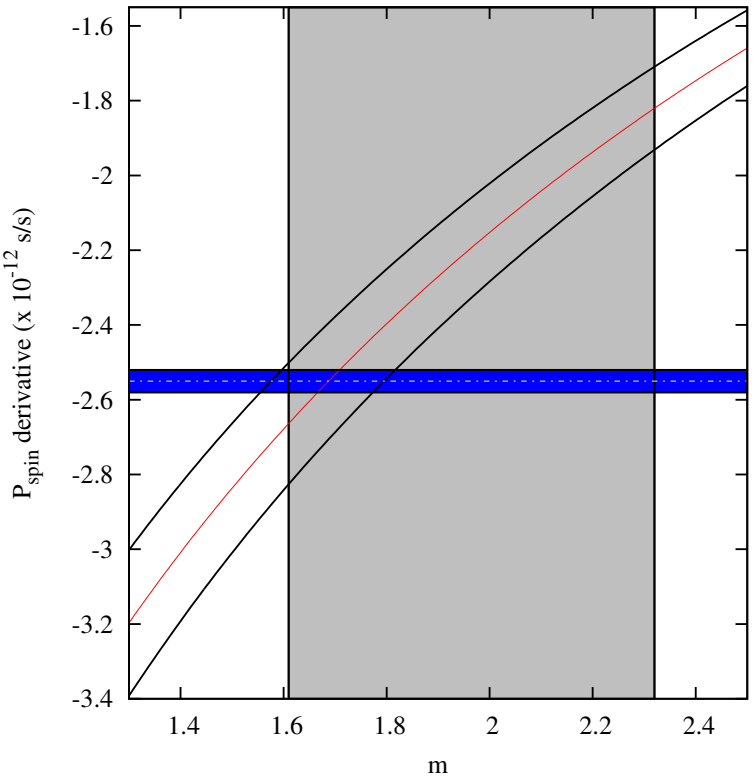

Figure 3.12: Spin period derivative, $\dot{P}_{-12}$ vs. M_{NS} for a NS radius of 10 km (red curve); the black curves represent the upper and lower limit values of the spin derivative. The grey box indicates the mass range allowed for X1822-371 according to Muñoz-Darias et al.(2005)[55]. The horizontal blue strip indicates the value of $\dot{P}_{-12}$ as derived in Sect.3.4

For a range of M_{NS} between 1.3 and 2.5 $M_{\odot}$, the $\dot{P}_{-12}$ changes from -3.4 up to -1.6. The grey box in Fig.3.12 limits the allowed NS mass between $1.61 \div 2.32 M_{\odot}$ according to ñoz-Darias et al.(2005)[55].

Furthermore, the value of the spin period derivative $\dot{P}_{-12} = -2.55 \pm 0.03 s/s$ that we obtained in chapter 3.4, is shown, as are the uncertainties associated with $\dot{P}_{-12}$. We find a NS mass of $1.69 \pm 0.13 M_{\odot}$, assuming $R_6 = 1$, which is inside the range suggested by Muñoz-Darias et al.(2005)[55]. Consequently, using the

Eq.3.2, we find that the NS B-field is $(8.8 \pm 0.3) \times 10^{10} G$, a value that is very similar to the one suggested by Jonker & van der Klis (2001) [29] assuming a luminosity of$\sim 10^{38}$ for X1822-371. Using the mass function $(2.03 \pm 0.03) \times 10_{\odot}^{-2}$ and an inclination angle of X1822-371 of 82.5° (see Jonker et al., 2003 [60]), we infer the companion star mass, $M_c = 0.46 \pm 0.02 M_{\odot}$, which is close to the value of $0.5 M_{\odot}$ suggested by Muñoz-Darias et al.(2005)[55]. Using only optical observations, Somero et al. (2012) [61] estimate that the mass ratio of X1822-371 is $q = M_c/M_{NS} = 0.28$. Using this relation, we find that the companion star mass is $M_c = 0.47 \pm 0.04 M_{\odot}$ for a NS mass of $1.69 \pm 0.13 M_{\odot}$, and that value is compatible with the one inferred by us using the mass function.

Assuming different NS radii for Eq.3.5, we obtain different values of the NS mass. We show the NS masses for several values of the NS radius ranging from 8 to 11.5 km in Table 3.4. The NS radius in X1822-371 cannot be larger than 11.5 km because the NS mass would be lower than $1.61 M_{\odot}$ which is the lower limit given by Muñoz-Darias et al.(2005)[55]. This result further constrains the NS mass range between $1.46 M_{\odot}$ and $1.81 M_{\odot}$.

The NS B-field ranges between $7.8 \times 10^{10} G$ and $10.5 \times 10^{10} G$ and, finally, the companion star mass ranges between $0.41 M_{\odot}$ and $0.48 M_{\odot}$.

We compared the results in Table 3.4 with those obtained by Steiner et al.(2010)[62], which determined an empirical dense matter equation of state from a heterogeneous data set of six neutron stars: three Type-I X-ray busters with photospheric radius expansion and three transient low-mass X-ray binaries. Our comparison was done with the results reported in Table 7 by Steiner et al.(2010)[62]. They are valid for a NS radius equal to the photospheric radius of the NS. The authors find that for a NS mass $1.6 M_{\odot}$, $1.7 M_{\odot}$ and $1.8 M_{\odot}$ the corresponding radius is $10.8^{+0.6}_{-0.9} km$, $10.7^{+0.8}_{-1.2} km$ and $10.7^{+0.7}_{-1.1} km$, respectively, with the errors at 95%. If the NS in X1822-371 is similar to those of the sample studied by Steiner et al.(2010)[62], we can exclude from Table 3.4 the solutions for NS radii smaller than 9.5 km. This implies that the NS mass range is between $1.61 \pm 0.15 M_{\odot}$ and $1.70 \pm 0.13 M_{\odot}$, that the NS B-field in units of $10^{10} G$ is between $8.1 \pm 0.3 \times 10^{10} G$ and $9.0 \pm 0.3 \times 10^{10} G$ and finally that the companion star mass is between $0.44 \pm 0.03 M_{\odot}$ and $0.46 \pm 0.02 M_{\odot}$.

We note that the estimation of the CRSF energy is model dependent. The CRSF energy is 0.72 and 0.68 keV, adopting the `gabs` and `cyclabs` components,

respectively, to fit the averaged spectrum. However, the values of the NS mass, NS magnetic-field strength, and companion star mass at different NS radii are the same as shown in Table 3.4 even using the CRSF energy obtained from the `cyclabs` component, since this energy and the NS magnetic-field strength, B_{12}, are linearly dependent (see Eq.3.2) and because the spin period derivative weakly depends on B_{12} (see Eq.3.5). The `gabs` component allows us to estimate the temperature of the plasma where the CRSF originates, assuming that the broadening of the line has a thermal origin. At the cyclotron resonance frequency ω_c, electrons at rest absorb photons of energy $\hbar\omega_c$. For thermal Doppler broadening, $\Delta\omega_D$ is predicted to be (see Mészáros (1992)[63]):

$$\frac{\Delta\omega_D}{\omega_c} = \left(\frac{2kT_e}{m_e c^2}\right)^{1/2} |cos\theta|$$

where $\hbar\Delta\omega_D = \sigma_{gabs}$, $\hbar\omega_c = E_{gabs}$, KT_e is the electron temperature and $m_e c^2$ is the rest electron energy.

The angle θ measures the direction of the magnetic field with respect to the line of sight. Outside the range $\omega_c \pm \Delta\omega_D$, the cyclotron absorption coefficient decays exponentially, and other radiative processes become important. Substituting the values of σ_{gabs} and E_{gabs} shown in Table 3.2 (for MOS12 spectrum ranging between 1.5 and 10 keV), we obtain a lower limit on the plasma temperature of $kT = 8 \pm 2keV$ with the error at 68% confidence level, which is a factor of two or three larger than the electron temperature of the `Comptt` component, but the values are consistent at the 2σ level. This suggests that the Comptonised component is probably produced in the accretion column onto the NS magnetic caps-

We do not observe cyclotron harmonics in the spectrum. To date, the lowest energy measured for a CRSF produced by electron motion around the NS magnetic-field lines is 9 keV in the source XMMU J054134.7-682550 (Manousakis et al.(2009)[64]); also in that case, harmonics are not visible in the spectrum. The cyclotron line observed in the spectrum of the Be/X-Ray Binary Swift J1626.6-5156 has an energy of 10 keV and only a weak indication of a harmonic at 19 keV (see DeCesar et al.(2013)[65]). The source KS 1947+300 has been recently observed with Nuclear Spectroscopy Telescope Array (NuSTAR) and Swift/XRT in the 0.8-79 keV energy range (Fürst et al.(2014)[66]); a CRSF at 12.5 keV has been observed but no harmonics have been detected. Finally, the anomalous X-ray pulsar SGR 0418+5729 shows a CRSF produced by proton motion, with

centroid at 1 keV, and no harmonics are observed (see Tiengo et al.(2013)[67]). To now, only the isolated NS CCO 1E1207.4-5209 shows a CRSF also and its first harmonic at 0.7 and 1.4 keV, respectively (Sanwal et al.(2002)[68]; Mereghetti et al.(2002)[69]). These results show that, although peculiar, it is possible to observe only the fundamental harmonic of the CRSF.

Finally, we note that the presence of a CRSF at 0.7 keV shown in this work contrasts with the recent result suggested by Sasano et al. (2014)[39], who find a CRSF at 33 keV when analysing the same Suzaku data as presented in this work. First of all, we note that a CRSF at 33 keV is detectable including the HXD/PIN data up to 40 keV. However, we have shown that the HXD/PIN source spectrum is overwhelmed by the NXB+CXB spectrum at energies higher than 36 keV (see Fig.3.7). Furthermore, we note that, at 33 keV, the HXD/PIN effective area is nearly $50cm^2$, while the HPGSPC and PDS instruments on-board BeppoSAX had an effective area of $\sim 200cm^2$ and $\sim 500cm^2$, respectively. Iaria et al. (2001)[37] analysed a broad band spectrum of X1822-371 using the narrow-field instruments on-board BeppoSAX and did not find any evidence of a CRSF at 30 keV with a PDS exposure time of 18.7 ks. The HXD/PIN spectrum has an exposure time of 37.7 ks, which is a factor of two longer than the PDS exposure times, but it has an effective area a factor of 10 smaller at 33 keV. The presence of a CRSF at 33 keV in the Suzaku data is therefore unrealistic when assuming that it does not change in time.

To verify the presence of a CRSF at 33 keV, we have also analysed the IBIS and JEM-X spectra for an effective dead-time-corrected exposure of 874 ks and 283 ks, respectively. We fitted both the spectra, adopting the same model as used to fit the XMM-Newton/Suzaku data and found no evidence of CRSF at 33 keV. We also note that a CRSF at 33 keV is not consistent with the observed spin-up of the NS. Assuming that the NS is spinning-up and using the NS B-field value inferred by a CRSF at 33 keV, Sasano et al. (2014)[39] obtain an intrinsic luminosity of the system of $\sim 3\times10^{37} erg\ s^{-1}$ needed to have the measured spin-up rate.

In case of spin-up, we expect that the corotation radius r_c has to be larger than the magnetospheric radius r_m. The values of r_c is 1180 km and 1300 km for a NS mass of $1.4M_\odot$ and $2M_\odot$, respectively, assuming the value reported by Sasano et al. (2014) [39] as spin period. To estimate the magnetospheric radius, we used

the Eq.3.1 assuming a NS radius of 10 km and a NS B-field of $2.8 \times 10^{12} G$ (vedi Sasano et al.(2014)[39]). we find that $r_A \simeq 5940 km$ and $r_m = \phi r_A \simeq 3000 km$, with $\phi = 0.5$. We infer that $r_m \simeq 3 r_c$, and this implies that matter cannot accrete onto the NS; this scenario corresponds to that discussed by Ghosh & Lamb (1979)[58] for $\omega_s \gg \omega_{max}$, with $\omega_{max} \simeq 0.95$. Infact:

$$\omega_s \simeq 1.35 B_{12}^{6/7} M_{NS}^{-2/7} P_s^{-1} L_{37}^{-3/7}$$

for a NS radius of 10 km (see Eqs. (16) and (18) in Ghosh & Lamb (1979)[58]). Using the values of luminosity, spin period, and NS B-field reported by Sasano et al.(2014)[39], we find that $\omega_s \simeq 3.2$, for a NS mass of $1.3 M_\odot$, and $\omega_s \simeq 2.5$ for $3 M_\odot$.

This result suggests that the scenario is not self-consistent because the values of luminosity and NS B-field would contradict the observed spin-up of the NS.

3.8 Conclusion

We analysed the broadband X-ray spectrum of X1822-371 to understand the nature of the residuals between 0.6 and 0.8 keV previously observed in the XMM/EPIC-pn data by Iaria et al. (2013)[38]. To fit the residuals between 0.6 and 0.8 keV, we added an absorption feature with Gaussian profile (`gabs` in XSPEC). Alternatively, we adopted an absorbing feature with Lorentzian profile (`cyclabs` in XSPEC). In both cases the addition of a CRSF to the model improved the fit. We found that the improvement does not depend sensitively on the exact shape used to model the absorption profile.

We also detected the spin period of X1822-371 in the EPIC-pn data. We obtained the value of 0.5928850(6) s. Using all the measurements known of the spin period of X1822-371, we estimated that the spin period derivative of the source is$-2.55(3) \times 10^{-12} s/s$, and this confirms that the neutron star is spinning up. Folding the EPIC-pn light curve, we derived a pulse fraction of 0.75% in the 2-5.4 keV energy band.

Using the best-fit values of the CRSF parameters, under the assumption that the system is accreting at the Eddington limit, we estimate a NS B-field between $(8.1 \pm 0.3 \times 10^{10}) G$ and $(9.0 \pm 0.3 \times 10^{10}) G$ for a NS radius ranging between 9.5 and 11.5 km.

We subsequently constrain the NS mass assuming that the CRSF is produced

at the NS surface. We find that, for a Gaussian profile of the CRSF, the NS mass is between $1.61 \pm 0.15 M_{\odot}$ and $1.70 \pm 0.13 M_{\odot}$. The companion star mass is constrained between $0.44 \pm 0.03 M_{\odot}$ and $0.46 \pm 0.02 M_{\odot}$.

Finally, we note that our conclusions contrast with the recent results reported by Sasano et al. (2014)[39], who report detecting a CRSF at 33 keV (and a corresponding NS-B field of $3 \times 10^{12} G$) in the Suzaku data also used in this work. To address this point, we have selected the whole IBIS and JEM-X public data set of the X1822-371 region. We extracted the JEM-X and IBIS spectra of X1822-371 having an exposure time of 330 and 874 ks, respectively. The INTEGRAL spectrum combined with the XMM, Suzaku, and Chandra spectra does not show a CRSF at 33 keV. Furthermore, we also show from theoretical arguments that a CRSF at 33 keV is not consistent with the evidence that the NS in X1822-371 is spinning up.

	MOS12 spectrum in 0.6-7 keV				MOS12 spectrum in 1.5-7 keV			
	XMM	Suzaku	Chandra/MEG	INTEGRAL	XMM	Suzaku	Chandra/MEG	INTEGRAL
Parameters			Model: CompTT					
N_H (x $10^{22} cm^{-2}$)		0.126 ± 0.003				0.121 ± 0.003		
$N_{H,PC}$ (x $10^{22} cm^{-2}$)		4.48 ± 0.08				4.57 ± 0.08		
f		0.633 ± 0.005				0.638 ± 0.005		
E_{Edge1} (keV)		$7.20^{+0.02}_{-0.03}$				$7.20^{+0.02}_{-0.03}$		
τ_{Edge1}	0.076 ± 0.013	0.130 ± 0.011	0.076 ± 0.013	< 0.084	0.072 ± 0.013	0.129 ± 0.011	0.072 ± 0.013	< 0.084
E_{Edge2} (keV)		8.42 ± 0.05				8.43 ± 0.05		
τ_{Edge2}	0.09 ± 0.02	0.084 ± 0.013	0.09 ± 0.02	$0.13^{+0.08}_{-0.10}$	0.10 ± 0.02	0.084 ± 0.013	0.10 ± 0.02	$0.12^{+0.08}_{-0.10}$
KT_0 (keV)		0.059 ± 0.006				0.058 ± 0.006		
KT_e (keV)	3.55 ± 0.11	4.32 ± 0.05	$3.2^{+0.4}_{-0.3}$	4.89 ± 0.08	3.63 ± 0.12	4.33 ± 0.05	$3.3^{+2.8}_{-0.3}$	4.89 ± 0.08
τ	9.60 ± 0.15	9.09 ± 0.09	$9.7^{+0.3}_{-0.5}$	6.0 ± 0.2	9.43 ± 0.15	9.04 ± 0.09	$9.6^{+0.4}_{-1.4}$	6.0 ± 0.2
$N_{CompTT}(10^{-2})$		$6.6^{+0.3}_{-0.2}$				6.5 ± 0.3		
χ^2_{red} (d.o.f)		1.21(2496)				1.10(2466)		
Parameters			Model: gabs*CompTT					
N_H (x $10^{22} cm^{-2}$)		0.100 ± 0.006				0.100 ± 0.006		
$N_{H,PC}$ (x $10^{22} cm^{-2}$)		4.54 ± 0.08				4.61 ± 0.08		
f		0.645 ± 0.005				0.647 ± 0.005		
E_{Edge1} (keV)		$7.20^{+0.02}_{-0.04}$				$7.20^{+0.02}_{-0.04}$		
τ_{Edge1}	0.075 ± 0.013	0.125 ± 0.011	0.075 ± 0.013	< 0.084	0.071 ± 0.013	0.126 ± 0.011	0.071 ± 0.013	< 0.084
E_{Edge2} (keV)		8.43 ± 0.05				8.43 ± 0.05		
τ_{Edge2}	0.10 ± 0.02	0.081 ± 0.013	0.10 ± 0.02	$0.12^{+0.08}_{-0.10}$	0.10 ± 0.02	0.081 ± 0.013	0.10 ± 0.02	$0.12^{+0.08}_{-0.10}$
E_{gabs} (keV)		0.73 ± 0.03				0.72 ± 0.03		
σ_{gabs} (keV)		0.14 ± 0.03				0.13 ± 0.03		
τ_{gabs}		$0.038^{+0.014}_{-0.009}$				$0.031^{+0.013}_{-0.009}$		
KT_0 (keV)		0.056 ± 0.010				0.052 ± 0.011		
KT_e (keV)	$3.61^{+0.12}_{-0.10}$	4.33 ± 0.05	$3.2^{+0.5}_{-0.3}$	4.89 ± 0.08	3.67 ± 0.12	4.33 ± 0.05	$3.2^{+0.6}_{-0.3}$	4.89 ± 0.08
τ	9.5 ± 0.2	9.00 ± 0.10	$9.6^{+0.4}_{-0.5}$	6.0 ± 0.2	9.3 ± 0.2	8.98 ± 0.09	$9.6^{+0.4}_{-0.6}$	6.0 ± 0.2
$N_{CompTT}(10^{-2})$		$6.7^{+0.5}_{-0.4}$				6.7 ± 0.6		
χ^2_{red} (d.o.f)		1.12(2493)				1.04(2463)		
Parameters			Model: cyclabs*CompTT					
N_H (x $10^{22} cm^{-2}$)		0.100 ± 0.006				0.104 ± 0.004		
$N_{H,PC}$ (x $10^{22} cm^{-2}$)		4.54 ± 0.08				$4.75^{+0.16}_{-0.10}$		
f		0.645 ± 0.005				0.643 ± 0.005		
E_{Edge1} (keV)		$7.20^{+0.02}_{-0.04}$				$7.20^{+0.02}_{-0.04}$		
τ_{Edge1}	0.075 ± 0.013	0.125 ± 0.011	0.075 ± 0.013	< 0.084	0.069 ± 0.013	0.122 ± 0.011	0.069 ± 0.013	< 0.084
E_{Edge2} (keV)		8.43 ± 0.05				8.43 ± 0.05		
τ_{Edge2}	0.10 ± 0.02	0.078 ± 0.013	0.10 ± 0.02	$0.12^{+0.08}_{-0.10}$	0.10 ± 0.02	0.079 ± 0.013	0.10 ± 0.02	$0.12^{+0.08}_{-0.10}$
$E_{cyclabs}$ (keV)		$0.69^{+0.03}_{-0.04}$				$0.68^{+0.04}_{-0.05}$		
$W_{cyclabs}$ (keV)		0.16 ± 0.04				0.15 ± 0.04		
$Dept_{cyclabs}$		0.13 ± 0.02				0.12 ± 0.02		
KT_0 (keV)		0.055 ± 0.010				0.051 ± 0.011		
KT_e (keV)	3.64 ± 0.13	4.34 ± 0.05	$3.2^{+0.5}_{-0.3}$	4.89 ± 0.08	$3.70^{+0.13}_{-0.11}$	4.34 ± 0.05	$3.2^{+2.8}_{-0.3}$	4.89 ± 0.08
τ	9.4 ± 0.2	8.91 ± 0.10	$9.5^{+0.4}_{-0.5}$	6.0 ± 0.2	9.2 ± 0.2	$8.91^{+0.10}_{-0.18}$	$9.6^{+0.4}_{-1.5}$	6.0 ± 0.2
$N_{CompTT}(10^{-2})$		6.8 ± 0.5				6.9 ± 0.6		
χ^2_{red} (d.o.f)		1.12(2493)				1.04(2463)		

Table 3.2: Best-fit values of the continuum emission. Uncertainties are at the 90% confidence level for a single parameter. The $\chi^2_{d.o.f.}$ values are obtained taking the emission lines shown in Table 3.3 into account.

	MOS12 spectrum in 0.6-7 keV			**MOS12 spectrum in 1.5-7 keV**		
Line	E(keV)	σeV	I($\times 10^{-4}$)	E(keV)	σeV	I($\times 10^{-4}$)
			`Model: CompTT`			
N_{VII}	0.5 (fixed)	1 (fixed)	2.8 ± 0.9	0.5 (fixed)	1 (fixed)	2.5 ± 0.9
O_{VII} (i)	0.5687 (fixed)	1.5 (fixed)	19 ± 2	0.5687 (fixed)	1.5 (fixed)	17 ± 2
O_{VIII}	0.6536 (fixed)	1 (fixed)	1.8 ± 0.5	0.6536 (fixed)	1 (fixed)	1.6 ± 0.5
Ne_{IX} (i)	0.915 (fixed)	3 (fixed)	2.5 ± 0.3	0.915 (fixed)	3 (fixed)	$2.6^{+0.9}_{-0.3}$
Ne_X	1.022 (fixed)	3 (fixed)	0.9 ± 0.2	1.022 (fixed)	3 (fixeda)	$0.9^{+0.5}_{-0.2}$
Mg_{XI} (i)	1.3434 (fixed)	3 (fixed)	0.72 ± 0.14	1.3434 (fixed)	3 (fixed)	$0.69^{+0.48}_{-0.13}$
Mg_{XII}	1.4726 (fixed)	3 (fixed)	0.40 ± 0.06	1.4726 (fixed)	3 (fixed)	$0.34^{+0.27}_{-0.09}$
Si_{XIV}	2.005 (fixed)	3 (fixed)	0.35 ± 0.10	2.005 (fixed)	3 (fixed)	$0.35^{+0.27}_{-0.08}$
Fe_I	6.408 (fixed)	20 ± 15	2.31 ± 0.15	6.408 (fixed)	22 ± 15	2.30 ± 0.15
Fe_{XXVI}	6.98 ± 0.03	50 (fixed)	0.59 ± 0.13	6.98 ± 0.03	50 (fixed)	0.60 ± 0.14
			`Model: gabs*CompTT`			
N_{VII}	0.5 (fixed)	1 (fixed)	1.7 ± 0.8	0.5 (fixed)	1 (fixed)	1.7 ± 0.8
O_{VII} (i)	0.5687 (fixed)	1.5 (fixed)	14.8 ± 1.5	0.5687 (fixed)	1.5 (fixed)	14.6 ± 1.5
O_{VIII}	0.6536 (fixed)	1 (fixed)	1.8 ± 0.5	0.6536 (fixed)	1 (fixed)	1.8 ± 0.5
Ne_{IX} (i)	0.915 (fixed)	3 (fixed)	2.6 ± 0.4	0.915 (fixed)	3 (fixed)	$2.6^{+1.1}_{-0.4}$
Ne_X	1.022 (fixed)	3 (fixed)	0.7 ± 0.2	1.022 (fixed)	3 (fixed)	$0.8^{+0.4}_{-0.2}$
Mg_{XI} (i)	1.3434 (fixed)	3 (fixed)	0.68 ± 0.14	1.3434 (fixed)	3 (fixed)	$0.66^{+0.36}_{-0.13}$
Mg_{XII}	1.4726 (fixed)	3 (fixed)	0.39 ± 0.06	1.4726 (fixed)	3 (fixed)	$0.34^{+0.21}_{-0.10}$
Si_{XIV}	2.005 (fixed)	3 (fixed)	0.40 ± 0.05	2.005 (fixed)	3 (fixed)	$0.36^{+0.25}_{-0.08}$
Fe_I	6.408 (fixed)	23 ± 10	2.4 ± 0.2	6.408 (fixed)	24 ± 15	2.3 ± 0.2
Fe_{XXVI}	6.98 ± 0.03	50 (fixed)	0.62 ± 0.13	6.98 ± 0.03	50 (fixed)	0.62 ± 0.14
			`Modello: cyclabs*CompTT`			
N_{VII}	0.5 (fixed)	1 (fixed)	1.6 ± 0.8	0.5 (fixed)	1 (fixed)	1.6 ± 0.8
O_{VII} (i)	0.5687 (fixed)	1.5 (fixed)	14.8 ± 1.5	0.5687 (fixed)	1.5 (fixed)	14.6 ± 1.5
O_{VIII}	0.6536 (fixed)	1 (fixed)	1.8 ± 0.5	0.6536 (fixed)	1 (fixed)	1.8 ± 0.5
Ne_{IX} (i)	0.915 (fixed)	3 (fixed)	2.6 ± 0.4	0.915 (fixed)	3 (fixed)	$2.6^{+1.0}_{-0.4}$
Ne_X	1.022 (fixed)	3 (fixed)	0.8 ± 0.2	1.022 (fixed)	3 (fixed)	$0.8^{+0.5}_{-0.2}$
Mg_{XI} (i)	1.3434 (fixed)	3 (fixed)	0.64 ± 0.14	1.3434 (fixed)	3 (fixed)	$0.63^{+0.37}_{-0.13}$
Mg_{XII}	1.4726 (fixed)	3 (fixed)	0.32 ± 0.10	1.4726 (fixed)	3 (fixed)	$0.32^{+0.21}_{-0.10}$
Si_{XIV}	2.005 (fixed)	3 (fixed)	0.37 ± 0.09	2.005 (fixed)	3 (fixed)	$0.37^{+0.27}_{-0.08}$
Fe_I	6.408 ± 0.005	26 ± 15	2.4 ± 0.2	6.408 ± 0.005	26 ± 15	2.4 ± 0.2
Fe_{XXVI}	6.98 ± 0.03	50 (fixed)	0.64 ± 0.14	6.98 ± 0.03	50 (fixed)	0.65 ± 0.14

Table 3.3: Best-fit values of the emission lines. Uncertainties are at the 90% confidence level for a single parameter. The line intensities are in units of $fotoni\ cm^{-2}\ s^{-1}$.

$R_{NS}(km)$	$M_{NS}(M_\odot)$	$B(10^{10}G)$	$M_c(M_\odot)$
8	1.70 ± 0.11	10.2 ± 0.3	0.46 ± 0.02
8.5	1.71 ± 0.12	9.7 ± 0.3	0.46 ± 0.02
9	1.71 ± 0.12	9.4 ± 0.3	0.46 ± 0.02
9.5	1.70 ± 0.13	9.0 ± 0.3	0.46 ± 0.02
10	1.69 ± 0.13	8.8 ± 0.3	0.46 ± 0.02
10.5	1.67 ± 0.14	8.5 ± 0.3	0.45 ± 0.03
11	1.64 ± 0.14	8.3 ± 0.3	0.45 ± 0.03
11.5	1.61 ± 0.15	8.1 ± 0.3	0.44 ± 0.03

Table 3.4: Values of R_{NS}, M_{NS}, $B10^{10}G$ and M_c obtained from the cyclotron line energy found adopting the `gabs` component (see chapter 3.6). Uncertainties are discussed in the text. For clarity we also show the values of M_{NS}, $B10^{10}G$ and M_c for R_{NS}=10 km. The errors are at 68% confidence level.

Chapter 4

A third body orbiting around XB 1916-053

This chapter is adapted from the paper: *Signature of the presence of a third body orbiting around XB1916-053*, by R.Iaria et al., 2015 ([70]).

4.1 Abstract

The aim of this work is investigate the nature of the orbital period derivative of the source XB 1916-053. This derivative was estimated to be $1.5(3) \times 10^{-11} s/s$ through analysing the delays associated with the dip arrival times obtained from observations spanning 25 years, from 1978 to 2002. This value is extremely large and can be explained by invoking an extreme, non-conservative mass transfer rate that is not easily justifiable. We extended the analysed data from 1978 to 2014, by spanning 37 years, to verify whether a larger sample of data can be fitted with a quadratic term or a different scenario has to be considered. From the analysis of the delays associated with the dip arrival times, we find that we have to invoke the presence of a third body to explain the observed sinusoidal modulation. We propose that XB 1916-053 forms a hierarchical triple system.

4.2 Introduction

The X-ray source XB 1916-053 is a low-mass X-ray binary (LMXB) showing dips and type-I X-ray bursts in its light curves. Using *OSO 8* data, Becker et

al., (1977) [71] observed type-I X-ray bursts, implying that the compact source in XB 1916-053 is a neutron star. Assuming that the peak luminosity of the X-ray bursts in XB 1916-053 is at the Eddington limit, Smale et al., (1988) [72] derived a distance to the source of 8.4 kpc or 10.8 kpc, respectively, depending on whether the accreting matter has cosmic abundances or is extremely hydrogen-deficient. Yoshida (1993) [73] inferred a distance to the source of 9.3 kpc studying the photospheric radius expansion of the X-ray bursts in XB 1916-053 (see also Barret et al., 1996 [74]). XB 1916-053 was the first LMXB in which periodic absorption dips were detected (Walter et al., 1982 [75]; White & Swank, 1982 [76]). These dips represent a decrease in the count rate in the light curve caused by periodic absorption of the X-ray emission produced in the inner region of the system. The photoelectric absorption occurs in a bulge at outer radius of the accretion disc where the matter streaming from a companion star impacts.

Accurate analysis of data sets from many X-ray satellites in the last 30 years have found different values for the X-ray period: Walter et al. (1982) [75] found a period close to 2985 s, using Einstein data; White & Swank (1982) [76] estimated a period of 3003.6 ± 1.8 s for the strongest dips, while Smale et al. (1989)[72], analysing GINGA data, derived a period of 3005.0 ± 6.6 s. Church et al. (1997)[77], analysing ASCA data, found an orbital period of 3005 ± 10 s. The X-ray light curve of XB 1916-053 also shows secondary dips occurring approximately half a cycle away from the primary dips with a certain variability in phase (see Grindlay 1989)[78]. No eclipses were found; this constrains the orbital inclination of the system between 60° and 80°.

The optical counterpart of XB1916-053 was discovered by Grindlay et al. (1987)[79], a star with a V magnitude of 21 already noted by Walter et al. (1982)[75]. Using thermonuclear flash models of X-ray bursts, Swank et al. (1984) [80] argued that the companion star is not hydrogen exhausted and suggested a companion star mass of $0.1 M_{\odot}$. Furthermore, Paczyński & Sienkiewicz (1981)[81] showed that X-ray binary systems with orbital periods shorter than 81 min cannot contain hydrogen-rich secondary stars.

A modulation in the optical light curve with a period of 3027.4 ± 0.4 s was discovered by Grindlay et al. (1988)[82]. The 1% discrepancy between the optical and X-ray period of XB 1916-053 was explained by Grindlay et al. (1988)[82] invoking the presence of a third body with a period of 2.5 d and a retrograde orbit that influences the matter streaming from the companion star. The same

authors also suggested the alternative scenario in which the disc bulge precesses around the disc with a prograde period equivalent to the beat period between the optical and X-ray period. White (1989)[83] suggested the possibility that a precessing elliptical disc exists in XB 1916-053, and that the variation in the projected area of this disc causes optical modulation. Callanan et al. (1995)[84] showed the stability of the optical period over seven years. Chou et al. (2001)[85], analysing Rossi X-ray Timing Explorer (RXTE) data taken in 1996, found several periodicities including one at 3026.23 ± 3.23 s, which was similar to the optical modulation at 3027 s. The centroid of these peaks in the periodogram associated with the 3000 s period implies that there is a modulation with a fundamental period close to 3.9 d, as already noticed by Grindlay (1992)[86] also in the optical band. The period of 3.9 d is interpreted as the beat period between the optical and X-ray periods. Furthermore, Chou et al. (2001)[85], folding the RXTE light curves at the 3.9 d period, found changes in the dip shape following this modulation. Those authors also indicated that the dip-phase change, with a sinusoidal period of 6.5 ± 1.1 d from Ginga 1990 September observations (Yoshida 1993 [73]; Yoshida et al. 1995 [87]), may be associated with the subharmonic of the 3.9 d period. Retter et al. (2002)[88] detected a further independent X-ray period at 2 979 s in the RXTE light curves of XB 1916-053, which was mistakenly identified by Chou et al.(2001)[85] with a 3.9 d sideband of the 3000 s period. Retter et al.(2002)[88] suggested that the period at 2979 s could be explained as a negative super-hump assuming the 3000 s period is the orbital period with a corresponding beat period of 4.8 d. The same authors suggested that the 3.9 and 4.8 d periods could be the apsidal and nodal precession of the accretion disc, respectively.

Finally, the source also showed a long-term 198.6 ± 1.72 d periodicity in X-rays (Priedhorsky & Terrel, 1984)[89], which has not been confirmed by further observations (see Retter et al. 2002)[88]. To date the spin period of the neutron star in XB 1916-053 is not known. Galloway et al. (2001)[90], analysing a Type-I X-ray burst, discovered a highly coherent oscillation drifting from 269.4 Hz up to 272 Hz. Interpreting the asymptotic frequency of the oscillation in terms of a decoupled surface burning layer, the neutron star could have a spin period around 3.7 ms. Hu et al. (2008)[91] inferred that $\dot{P}_{orb}/P_{orb} = (1.62 \pm \pm 0.34) \times 10^{-7} yr^{-1}$ by analysing archival X-ray data from 1978 to 2002 and adopting a quadratic ephemeris to fit the dip arrival times. In this work, we update the previously

determined ephemeris using data from 1978 to 2014. We show that the quadratic ephemeris does not fit the dip arrival times and find that a sinusoidal component is necessary to fit the delays. We suggest the presence of a third body that influences the orbit of the X-ray binary system XB 1916-053.

4.3 Observations and data reduction

We used all the available X-ray archival data of XB 1916-053 to study the long-term change of its orbital period. The last ephemeris of the source was reported by Hu et al. (2008) who used archival data from 1978 to 2002. We analysed more than 37 years of observational data from 1978 to 2014. The data have been obtained from the HEASARC (NASA's High Energy Astrophysics Science Archive Research Center) website and have been reduced using the standard procedures. In particular, we reanalysed the data used by Hu et al. (2008)[91], collected from 1998 to 2002, and added new data spanning up to 2014 (see Table 4.1). We obtained 27 points from all the analysed observations. The data collected by RXTE, Ginga, EXOSAT, Einstein, and OSO-8 were downloaded from HEASARC in light-curve format. We used the standard-1 RXTE/PCA background-subtracted light curves, which include all the energy channels and have a time resolution of 0.125 s. All the pointing observations were used except for P70034-02-01-01, P70034-02-01-00, and P93447-01-01-00 due to the absence of dips in the corresponding light curves.

The EXOSAT/ME light curves cover the energy range between 1 and 8 keV and have a time bin of 16 s. The Ginga/LAC light curves cover the 2-17 keV energy band. We only used the data from the top layer and the light curves binned at 16 s. We downloaded the ROSAT/PSPC events, and extracted the corresponding light curve using the FTOOLS `xselect`. The Medium Energy Concentrator Spectrometer (MECS) onboard the BeppoSAX satellite observed XB 1916-053 two times, in 1997 Apr 27-28 and 2001 Oct 01-02. Using `xselect`, we extracted the source light curves from a circular region centred on the source and with a radius of 4', no energy filter was applied to the data. The BeppoSAX/MECS light curves were obtained using a bin time of 2 sec. ASCA observed XB 1916-053 in 1993 May 02-03; we used the events collected by the GIS3 working in medium bit rate to extract the corresponding light curve. The OSO-8 light curve was obtained using the combined observation of the B and C detectors of the GSFC

Point	Satelite/Instrument	Observation	Start Time (UT)	Stop Time (UT)	T_{fold} (MJD,TDB)
1	OSO-8/GCXSE		1978 Apr 07 21:16:05	1978 Apr 14 22:20:37	43609.408575724435
2	Eistein/IPC		1979 Oct 22 04:52:01	1979 Oct 22 06:58:30	44168.24670380917
3	Eistein/IPC		1980 Oct 11 04:08:51	1980 Oct 11 09:07:19	44523.27644368849
4	EXOSAT/ME		1983 Sep 17 15:07:25	1983 Sep 17 21:29:49	45594.765324269885
5	EXOSAT/ME		1985 May 24 12:26:21	1985 May 24 21:30:23	46209.612747685185
6	EXOSAT/ME		1985 Oct 13 13:53:16	1985 Oct 13 22:34:04	46351.75944524423
7	Ginga/LAC		1988 Sep 09 15:47:56	1988 Sep 10 16:01:16	47414.165911835925
8	Ginga/LAC		1990 Sep 11 15:04:35	1990 Sep 13 09:18:11	48146.51075733274
9	ROSAT/PSPC	RP400274N00	1992 Oct 17 13:05:47	1992 Oct 19 15:24:20	48913.59379352164
10	ASCA/GIS3	40004000	1993 May 02 18:11:00	1993 May 03 09:46:17	49110.082393510115
11	RXTE/PCA	P10109-01-01-00, P10109-01-02-00, P10109-01-04-01, P10109-01-04-00, P10109-02-01-00, P10109-02-02-00, P10109-02-03-00, P10109-02-04-00, P10109-02-05-00, P10109-02-06-00, P10109-02-07-00, P10109-02-08-00, P10109-02-09-00, P10109-02-10-00, P10109-02-10-02	1996 Feb 02 00:14:56	1996 May 23 11:20:00	50174.74129123185
12	RXTE/PCA	P10109-01-05-00, P10109-01-06-00, P10109-01-07-00, P10109-01-08-00, P10109-01-09-00	1996 Jun 01 17:38:40	1996 Oct 29 11:00:34	50130.596956288645
13	BeppoSAX/MECS	20106001	1997 Apr 27 21:00:06	1997 Apr 28 19:51:02	50566.35264963594
14	RXTE/PCA	P30066-01-01-04, P30066-01-01-00, P30066-01-01-01, P30066-01-01-02, P30066-01-01-03, P30066-01-02-00, P30066-01-02-01, P30066-01-02-02, P30066-01-02-03	1998 Jun 23 23:06:40	1998 Jul 20 15:35:55	51001.306447481845
15	RXTE/PCA	P30066-01-02-04, P30066-01-02-07, P30066-01-02-08, P30066-01-03-00, P30066-01-03-01, P30066-01-03-02, P30066-01-03-03, P30066-01-03-04, P30066-01-03-05, P30066-01-04-00,	1998 Jul 21 07:11:44	1998 Sep 16 02:52:32	51043.70980975036
16	RXTE/PCA	P30066-01-05-01, P30066-01-05-00, P30066-01-06-00, P30066-01-06-01, P30066-01-07-00, P30066-01-07-01,	2001 May 27 08:14:47	2001 Jul 01 19:15:33	52074.07302734295
17	BeppoSAX/MECS	21373002	2001 Oct 01 03:40:16	2001 Oct 02 07:01:06	52183.72270184033
18	RXTE/PCA	P50026-03-01-00, P50026-03-01-01,	2001 Oct 01 10:35:44	2001 Oct 01 22:16:03	52183.684644754605
19	RXTE/PCA	P70034-02-02-01, P70034-02-02-00,	2002 Sep 25 00:43:12	2002 Sep 25 09:31:12	52542.21332826887
20	XMM/Epic-pn	0085290301	2002 Sep 25 04:18:29	2002 Sep 25 08:28:27	52542.266295747205
21	INTEGRAL/JEM-X		2003 Nov 09 09:04:11	2003 Nov 20 12:18:01	52957.945226848465
22	Chandra/HETGS	4584	2004 Aug 07 02:34:45	2004 Aug 07 16:14:53	53224.59478392645
23	Suzaku/XIS0	401095010	2006 Nov 08 06:09:51	2006 Nov 09 02:42:02	54048.3655207864
24	RXTE/PCA	P95093-01-01-00, P95093-01-01-01,	2010 Jun 19 13:41:52	2010 Jun 21 07:21:46	55367.43875650959
25	Chandra/LETGS	15271, 15657	2013 Jun 15 13:56:17	2013 Jun 18 05:13:17	56459.89915961875
26	Swift/XRT	00033336001	2014 Jul 15 08:04:57	2014 Jul 15 22:36:46	56853.63959388178
27	Suzaku/XIS0	409032010, 409032020	2014 Oct 14 16:49:56	2014 Oct 22 02:40:56	56949.56345974802

Table 4.1: Observation Log.

Cosmic X-ray Spectroscopy experiment(GCXSE). The light curve covers the 2-60 keV energy range. The Einstein light curve was obtained from events collected by the Image Proportional Counter (IPC) in the 0.2-3.5 keV energy range.

We applied barycentre corrections to the whole data set adopting the source position of XB 1916-053 shown by Iaria et al. (2006)[92]. For the RXTE/PCA light curves we used the ftools `faxbary`. The barycentre corrections for the ASCA and ROSAT data were obtained using the ftool `timeconv` and the tool `bct+abc`, respectively. All the other data sets were corrected using the ftool `earth2sun`.

Finally, we excluded the time intervals containing X-ray bursts from each analysed light curve.

The Chandra satellite observed XB 1916-053 three times. The first time was on 2004 Aug 07 from 2:34:45 to 16:14:53 UT (obsid 4584). The observation had a total integration time of 50 ks and was performed in timed graded mode. The spectroscopic analysis of this data set was discussed by Iaria et al. (2006)[92]. We reprocessed the data and applied the barycentre corrections to the event-2 file using the Chandra Interactive Analysis of Observations (CIAO) tool `axbary`. In addition, we extracted the summed first-order medium energy grating (MEG) and high energy grating (HEG) light curves filtered in the 0.5-10 keV energy range using the CIAO tool `dmextract`. The last two Chandra observations of XB 1916-053 (obsid 15271 and 15657) were performed between 2013 June 15 13:56 and June 18 5:13 UT and have exposure times of 60 and 30 ks, respectively. We reprocessed the data and applied the barycentre corrections to the event-2 file using `axbary`. Moreover, we extracted the first-order low energy grating (LEG) light curve in the 0.5-5 keV energy range using `dmextract`. We show the Chandra/LEG light curve in Fig. 4.1. Very intense dipping activity is present during the two observations. A type-I burst occurred during the obsid. 15271.

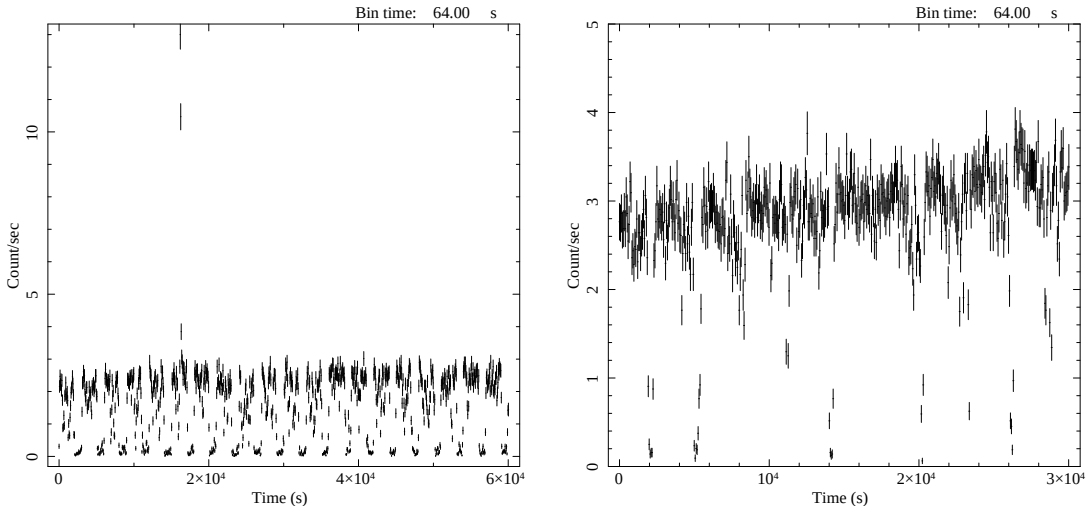

Figure 4.1: Chandra/LEG light curves of XB 1916-053 during the two observations performed in 2013, i.e. obsid. 15271 (left) and 15657 (right). The bin time is 64 s. A type-I X-ray burst that occurred during the obsid. 15271.

The X-ray Multi-Mirror Mission-Newton (XMM-Newton) observed XB 1916-053 on 2002 Sep 25 from 3:55 to 8:31 UT and the European Photon Imaging

Camera (Epic-pn) collected data, in timing mode, over $\sim$ 17 ks of exposure. An extensive study of this observation was performed by Boirin et al. (2004)[93]. We reprocessed the data, extracted the 0.5-10 keV light curve, and applied barycentre corrections to the times of the EPIC-pn events with the Science Analysis Software (SAS) tool barycen. Suzaku observed XB 1916-053 twice, the first time on 2006 Nov 8 (obsid. 401095010) and the second time from 2014 Oct 14 to 22 (obsid. 409032010 and 409032020). The first observation has already been analysed by Zhang et al. (2014)[94], while a study of the second observation has not been published yet. For both observations, we extracted the X-ray Imaging Spectrometer 0 (XIS0) events from a circular region centred on the source and with a radius of 130". We applied the barycentre corrections to the events with the Suzaku tool `aebarycen`. We do not show the light curve of the first Suzaku observation since it was already shown by Zhang et al. (2014) (Fig. 1 in their paper)[94], however, we show in Fig.4.10 the XIS0 light curve of the observation performed in 2014 Oct. The light curve indicates that a bursting activity is present in the first 200 ks of the observation and the persistent count rate decreases from 20 to 10 $counts\,s^{-1}$. In the second part of the observation, the persistent count rate is quite constant at 7 $counts\,s^{-1}$ and an intense dipping activity is present. For the aim of this work, we selected and used the events from 250 ks to the end of the observation.

Swift/XRT data were obtained as target of opportunity observations performed on 2014 Jul 15 from 07:55:53 to 22:27:58 UT (ObsID 00033336001) for a total on-source exposure of $\sim$ 6.3 ks and on 2014 Jul 21 from 07:32:00 to 16:11:5 UT (ObsID 00033336002) for a total on-source exposure of $\sim$ 9.0 ks. The count rate in the first observation reaches 15 $counts\,s^{-1}$, with a mean at about 10 $counts\,s^{-1}$, due to the dips seen down to 2 $counts\,s^{-1}$; the second observation shows no dips and has a mean count rate of 7 $counts\,s^{-1}$. Since the data from ObsID 00033336002 do not show dips we only used the first observation in our analysis. The XRT data were processed with standard procedures (`xrtpipeline` v0.13.1), and with standard filtering and screening criteria with FTOOLS (v6.16). Source events (selected in grades 0-2) were accumulated within a circular region with a radius of 20 pixels (1 pixel $\sim$ 2.36"). For our timing analysis, we also converted the event arrival times to the solar system barycentre with `barycorr`.

We selected a public data set of INTErnational Gamma-Ray Astrophysics Laboratory (INTEGRAL Winkler et al. 2003) [45] observations performed in

staring mode on XB 1916-053. Then, we analysed the data collected by the X-ray telescope JEM-X2 (Lund et al. 2003)[47]. A total amount of 87 pointings (the total observation elapsed time is $\sim$ 310 ks) covered the INTEGRAL revolutions 131, 133, and 134, which were carried out on 2003 November 9-20. We performed the JEM-X2 data analysis using standard procedures within the Offline Science Analysis software (OSA10.0) distributed by the ISDC (Courvoisier et al. 2003)[49]. We extracted the light curves with a 16 seconds binsize in the energy range 3-10 keV, and after that we applied the barycentre corrections to the events using the tool `barycent`.

4.4 Data analysis

We analysed 27 light curves and folded the barycentric-corrected light curves using a trial time of reference and orbital period, T_{fold} and P_0, respectively. For each light curve, the value of T_{fold} is defined as the average value between the corresponding start and stop time. We fitted the dips with a simple model consisting of a step.and-ramp function, where the count rates before, during, and after the dip are constant and the intensity changes linearly during the dip transitions. This model involves seven parameters: the count rate before, during, and after the dip, called C_1, C_2 and C_3, respectively; the phases of the start and stop time of the ingress (ϕ_1 and ϕ_2) and, finally, the phases of the start and stop time of the egress (ϕ_3 and ϕ_4). The phase corresponding to dip arrival time ϕ_{dip} is estimated as $\phi_{dip} = (\phi_4 + \phi_1)/2$. The corresponding dip arrival time is given by $t_{dip} = T_{fold} + \phi_{dip} P_0$. To be more conservative, we scaled the error associated with ϕ_{dip} by the factor $\sqrt{\chi^2_{red}}$ to take a value of χ^2_{red} of the best-fit model larger than 1 into account. To obtain the delays with respect to a constant period reference, we used the values of the period $P_0 = 3000.6511$ s and reference epoch $T_0 = 50123.00873$ MJD reported in Hu et al. (2008)[91]. We show the values of T_{fold} in Tab.1 (see 4). The best-fit parameters of the step-and-ramp function and the corresponding χ^2_{red} are shown in Tab. 4.2.

The inferred delays, in units of seconds, of the dip arrival times with respect to a constant orbital period are reported in Tab.4.3.

For each point we computed the corresponding cycle and the dip arrival time in days with respect to the adopted T_0 . We show the delays vs. time in Fig. 4.2.

Initially we fitted the delays with a quadratic function:

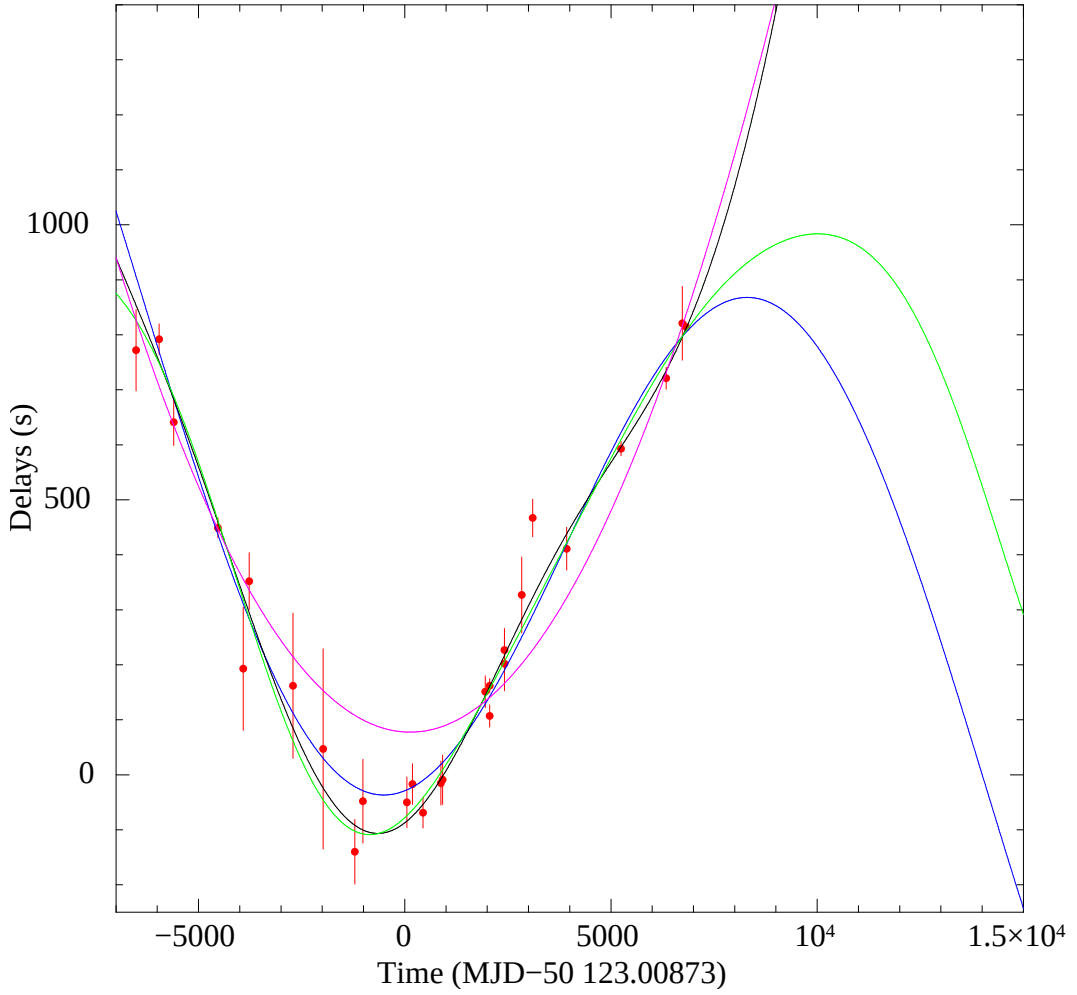

Figure 4.2: Dips's arrival time delays versus time. The magenta, blue, black and green curves are the best-fit curves obtained using the linear+quadratic (LQ), linear+sinusoidal (LS), linear+quadratic+sinusoidal (LQS), and linear+sinusoidal function taking into account a possible eccentricity (LSe), respectively.

$$y(t) = a + bt + ct^2$$

where t is the time in days with respect to T_0, a=ΔT_0 is the correction to T_0 in units of seconds, $b = \Delta P/P_0$ in units of sd^{-1} with ΔP the correction to the orbital period, and finally, $c = (1/2)\dot{P}/P_0$ in units of sd^{-1}, with $\dot{P}$ that is the orbital period derivative. The quadratic form does not fit the data, we obtained $\chi^2(d.o.f.)$ of 194.6(24). Here, and in the following, we scaled the uncertainties to take a value $\sqrt{\chi^2_{red}}$ to take a value χ^2_{red} of the best-fit model larger than 1 into account. The best-fit parameters are shown in the second column of Tab.4.4. The corresponding quadratic ephemeris (hereafter LQ ephemeris) is:

$$T_{dip}(N) = MJD(TDB)50123.0096(3) + \frac{3000.65094(14)}{86400}N + 2.37(12) \times 10^{-13}N^2 \tag{4.1}$$

where N is the number of cycles, 50123.0096(3) MJD is the new Epoch of reference, the revised orbital period is P =3000.65094(14) s, and the orbital period derivative obtained from the quadratic term is $\dot{P} = 1.36(7) \times 10^{-11} s/s$. The obtained quadratic ephemeris is compatible with that reported by Hu et al.(2008)[91].

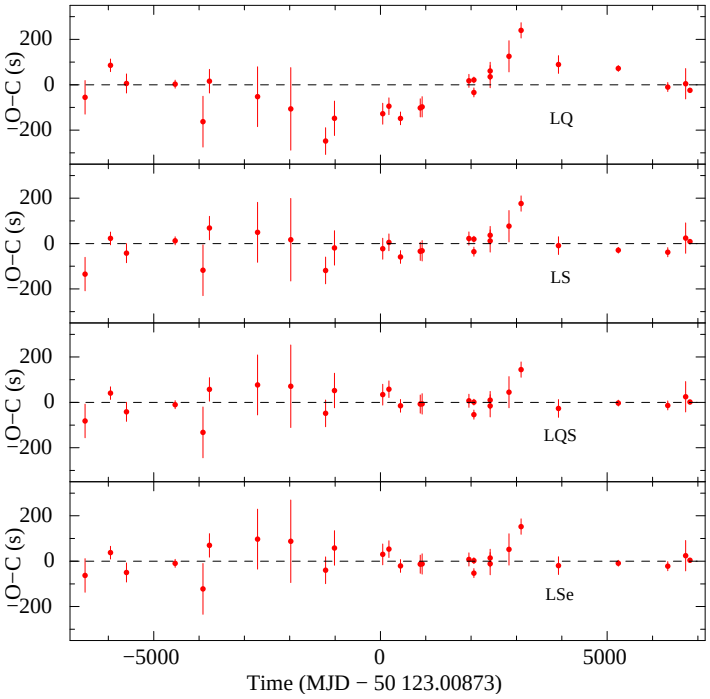

Figure 4.3: Observed minus calculated delays in units of seconds. The residuals, from the top to the bottom, correspond to the LQC, LS, LQS, and LSe function, respectively.

We show the best-fit curve in Fig.4.2 and the corresponding residuals in units of seconds in Fig. 4.3. As we obtained a large value of the χ^2 , we fitted the delays vs. time adding a cubic term to the previous parabolic function, i.e.:

$$y(t) = a + bt + ct^2 + dt^3$$

where a, b and c are above defined whilst the cubic term, d, is defined as $\ddot{P}/(6P_0)$, and $\ddot{P}$ indicates the temporal derivative of the orbital period derivative. Fitting with a cubic function, we obtained a $\chi^2(d.o.f.)$ of 92.4(23) with a $\Delta\chi^2$

of 101.2 and an F-test probability of chance improvement of 4.2×10^{-5} with respect to the quadratic form. The best-fit values are shown in the third column of Tab.4.4. The corresponding ephemeris (hereafter LQC ephemeris) is:

$$T_{dip}(N) = MJD(TDB)50123.00870^{0.00005}_{-0.00026} + \frac{3000.65239(3)}{86400}N + 2.97(12) \times 10^{-13}N^2 - 2.2(4) \times 10^{-22}N^3 \quad (4.2)$$

in this case we find an orbital period derivative of $1.71(7) \times 10^{-11}$s/s and its derivative is $\ddot{P} = -3.8(0.7) \times 10^{-20} s/s^2$. We also fitted the delays using a linear plus a sinusoidal function having the following terms:

$$y(t) = a + bt + Asin\left[\frac{2\pi}{P_{mod}}(t - t_\phi)\right]$$

where a and b are defined as above, A is the amplitude of the sinusoidal function in seconds, P_{mod} is the period of the sine function in days, and, finally, t is the time in days referred to T_0 at which the sinusoidal function is null. We obtained a value of $\chi^2(d.o.f.)$ of 63.7(22) with a $\Delta\chi^2$ of 131 with respect to the quadratic form. The best-fit parameters are shown in the fourth column of Tab.4.4. The best-fit function is indicated with a blue curve in Fig.4.2 and the corresponding residuals are shown in Fig.4.3. The residuals are flatter than those obtained in the previous case. Using the sinusoidal function, the dip time obtained from the OSO-8 observation is distant ~ 200 s from the expected value. The corresponding ephemeris (hereafter LS ephemeris) is:

$$T_{dip}(N) = MJD(TDB)50123.01549(18) + \frac{3000.6496(8)}{86400}N + Asin\left[\frac{2\pi}{N_{mod}}N - \phi\right] \quad (4.3)$$

where $N_{mod} = P_{mod}/P_0 = 587659.53 \pm 97351.67$ and $\phi = 2\pi t_\phi / P_{mod}$ with $P_{mod} = 55.9 \pm 9.3yr$. This functional form significantly improves the fit, even though it does not take the possible presence of an orbital period derivative into account. We added a quadratic term to take the possible presence of an orbital period derivative and fitted the delays into account, using the function:

$$y(t) = a + bt + ct^2 + Asin\left[\frac{2\pi}{P_{mod}}(t - t_\phi)\right]$$

We obtained a value of $\chi^2(d.o.f.)$ of 39.4(21) and a F-test probability of chance improvement with respect to the LS ephemeris of 1.7×10^{-3}. The best-fit parameters are shown in the fifth column of Tab.4.4. The best-fit function is indicated with a black curve in Fig.4.2 and the corresponding residuals are shown

in Fig.4.3. The corresponding linear+quadratic+sinusoidal ephemeris (hereafter LQS ephemeris) is:

$$T_{dip}(N) = MJD(TDB)50123.0089(3) + \frac{3000.65126(10)}{86400}N + \\ +2.50(12)\times 10^{-13}N^2 + Asin\left[\frac{2\pi}{N_{mod}}N - \phi\right] \tag{4.4}$$

with $N_{mod} = 267837.87 \pm 21652.90$ and $\phi = 0.92 \pm 0.16$. The corresponding orbital period derivative is $\dot{P} = 1.44(7)\times 10^{-11}$ s/s and the period od the modulation is $P_{mod} = 25.5 \pm 2.1$ yr. Our analysis of the delays suggests that a quadratic or a quadratic plus a cubic term do not fit the delays. A better fit is obtained using a sinusoidal function with a period close to 20000 d and, finally, adopting a sinusoidal plus a quadratic term, we obtain the best fit of the delays. In this latter case, the sinusoidal function has a period of 9300 d, about half of that obtained using only the sinusoidal function. Moreover, the orbital period derivative $\dot{P} = 1.44(7)\times 10^{-11}$ s/s (compatible with $\dot{P} = 1.5(3)\times 10^{-11}$ s/s obtained by Hu et al. 2008 [91]) is extremely high to be explained by a conservative mass transfer and loss of angular momentum from the binary system for gravitational radiation (see section 4.5 and paragraph 2.4.2.1). This awkward result can be bypassed if the quadratic term is merely an approximation of a further sinusoidal function with a larger orbital period with respect to 9300 d. Under this assumption, the best fit obtained using the LQS ephemeris could be explained using a different scenario, where the quadratic term mimics the fundamental harmonic of a series expansion whilst the sinusoidal term is the first harmonic. This seems also suggested by the best fit obtained using the LS function (eq. 4.3), since we obtain a modulation period, which is almost twice that obtained using the LQS function (eq.4.4). If we assume that XB 1916-053 is part of a hierarchical triple system then the measured delays are also affected by the influence of a third body. If the orbits of the third body and of the X-ray binary system around the common centre of mass are slightly elliptical then the delay $\Delta_{DS}(t)$ associated with the Doppler shift can be expressed as:

$$\Delta_{DS}(t) = A\left\{sin(m_t + \varpi) + \frac{e}{2}\left[sin(2m_t + \varpi) - 3sin\varpi\right]\right\} + \\ +A\left\{\frac{e^2}{4}\left[2sin(3m_t + \varpi) - sin(m_t + \varpi)cos(2m_t + 1) - 2sin(m_t)cos\varpi\right]\right\} \tag{4.5}$$

where

$$m_t = \frac{2\pi}{P_{mod}}(t - t_\phi)$$

is the mean anomaly; e is the eccentricity of the orbit; P_{mod} is the orbital period of both the X-ray binary system and the third body around the common centre of mass; ϖ denotes the periastron angle; t_ϕ is the passage time at the periastron; and $A = asini/c$ is the projected semi-major axis of the orbit, described by the centre of mass of the X-ray binary system around the centre of mass of the triple system. We neglect third and higher order terms in Eq.4.5. Limiting Eq.4.5 to the first-order terms, it becomes the expression shown by van der Klis & Bonnet-Bidaud (1984)[95]. Then, we fitted the delays using:

$$y(t) = a + bt + \Delta_{DS}(t)$$

Because the 27 available points do not cover a whole period, we arbitrarily fixed the value of P_{mod} at 18600, 17100 and 20100 d, which are the best, lower, and upper value of the period obtained from the LQS ephemeris multiplied by a factor of two. The best-fit parameters are shown in Tab.4.4 (columns 6, 7, and 8). The $\chi^2 d.o.f.$ are similar for the three adopted periods and the F-test probability of chance improvement with respect to LS function is $4.1 \times 10^{?2}$, $1.7 \times 10^{?2}$ and $0.9 \times 10^{?2}$ for a P_{mod} value of 17100, 18600 and 20100 d, respectively. In the following, we discuss the case of $P_{mod} = 18600$ d. The best-fit function is indicated with a green curve in Fig.4.2. The corresponding residuals are shown in Fig.4.3. The corresponding ephemeris (hereafter LSe ephemeris) is:

$$T_{dip}(N) = MJD(TDB)50123.010(3) + \frac{3000.6512(6)}{86400}N + \Delta_{DS}(N). \qquad (4.6)$$

To verify the robustness of our results, we produced the folded light curves in the 3-5 and 5-12.2 keV energy bands of XB 1916-053 obtained from the All Sky Monitor (ASM) on board RXTE using the ephemeris shown above. We inferred those ephemeris using only pointing observations from which we obtained 27 points spanning from 1978 to 2014, whilst the RXTE/ASM light curves cover from 1996 Sep 01 to 2011 Oct 31. We applied the barycentre corrections to the RXTE/ASM events. As a first step, we folded the RXTE/ASM light curves of XB 1916-053 using the LQ ephemeris reported by Hu et al., (2008)[91] and by us (Eq. 4.1), adopting 60 phase-bins per period corresponding to ~ 50 s per bin.

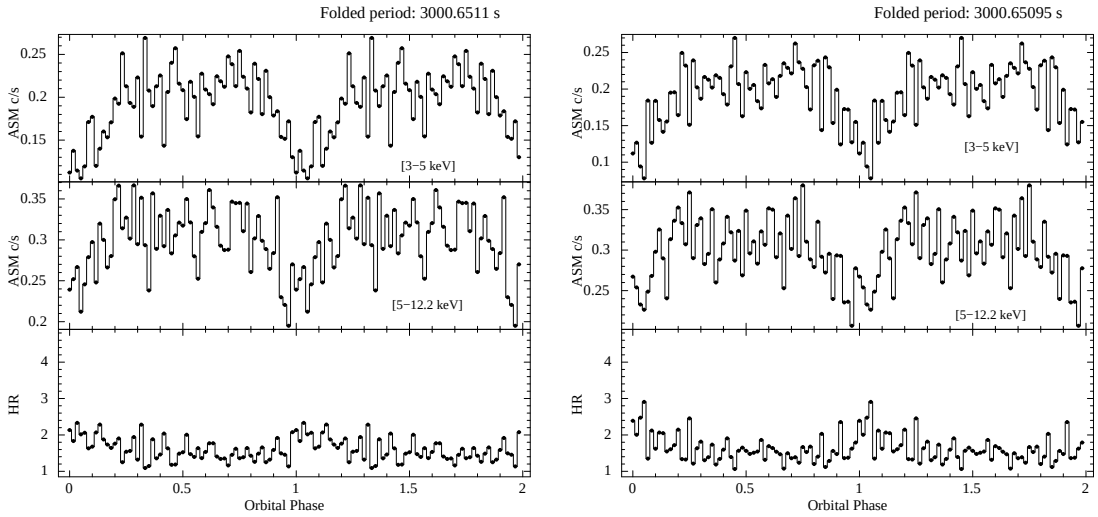

Figure 4.4: Folded RXTE/ASM light curve of XB 1916-053 in the 3-5 and 5-12.2 keV energy range (top and middle panels). The corresponding hardness ratios (HRs) are plotted in the bottom panels. The left and right plots show the folded RXTE/ASM light curve using the ephemeris discussed by Hu et al. (2008) and LQ ephemeris (eq. 4.1) shown in the Sect.4.4, respectively. Each phase-bin is about 50 s.

The folded light curves and the corresponding hardness ratios (HRs) are shown in Fig.4.4.

None of the HR show an evident increase at phase zero as we would expect if the ephemerides well define the dip arrival times. This implies that those ephemerides do not correctly predict the dip arrival times contained in the RXTE/ASM light curve. Adopting the LQC ephemeris (eq. 4.2), the maximum value of HR (that is 2.8) is reached at phase 0.1 (see Fig. 4.5, left panels).

Also in this case, the LQC ephemeris does not predict the dip arrival times in the ASM light curves of XB 1916-053. Using the LS ephemeris (Eq. 4.4) to fold the light curves, we obtained that the maximum value of HR is reached at phase zero and is close to 3.4 (see Fig. 4.5, right panels). In contrast, with the LQS ephemeris (Eq. 4.6) the maximum value of the HR falls in two phase-bins close to phase zero (see Fig. 6, left panels) and the maximum value of HR is 3.2, which is smaller than the value obtained with the LS ephemeris. Finally, we folded the RXTE/ASM light curves using the LSe ephemeris (eq. 4.6). We show the folded light curves and the corresponding HR in Fig. 4.6 (right panel).

In this last case the maximum value of the HR falls in only one phase bin at phase zero and the maximum value of the HR is about 4.5. We also folded

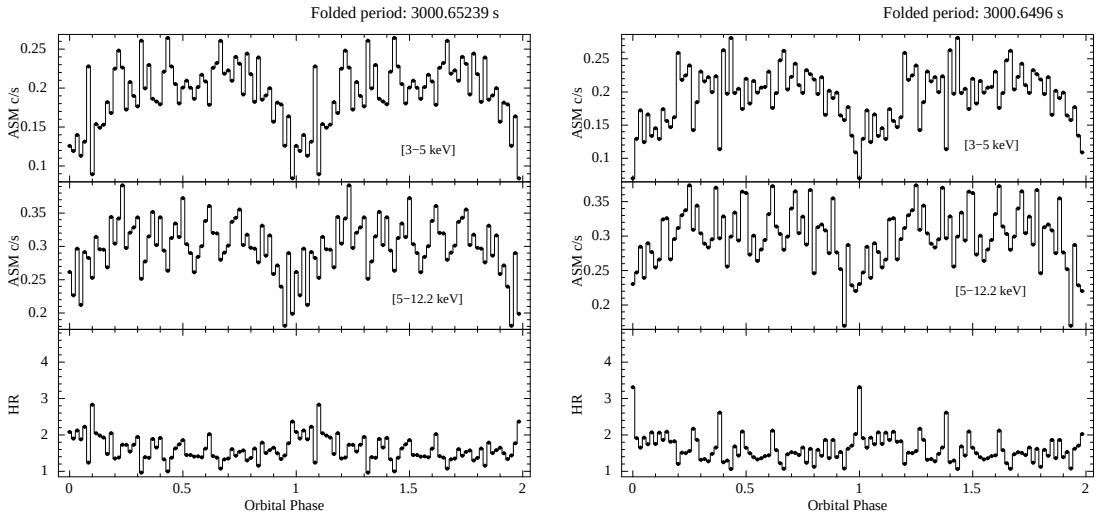

Figure 4.5: Left and right plots show the folded RXTE/ASM light curve using LQC ephemeris (eq. 4.2) and LS ephemeris (eq. 4.4), respectively. Each phase-bin is about 50 s.

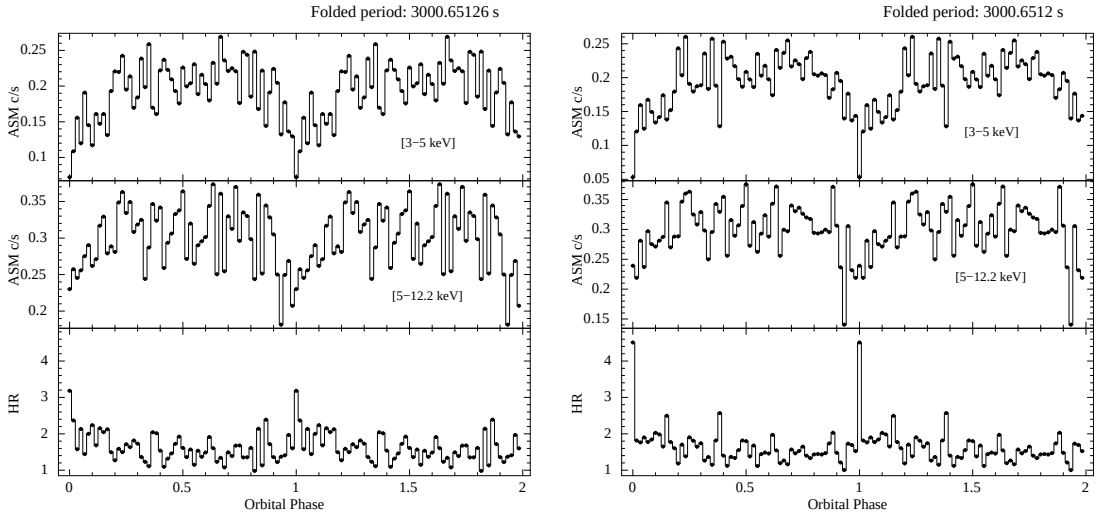

Figure 4.6: Left and right plots show the folded RXTE/ASM light curve using LQS ephemeris (eq. 4.4) and LSe ephemeris (eq. 4.6) with P_{mod} = 18600 d, respectively. Each phase-bin is about 50 s.

the RXTE/ASM light curve (not filtered in energy) using the LQS and LSe ephemerides once we selected the events from the Scanning Shadow Cameras (SSCs) 1 and 2. Adopting 40 phase-bins per period (that is each bin is 75 s), the folded light curves are very similar (see Fig. 4.7), indicating that the two ephemerides are statistically equivalent. The dip is clearly observed at phase

zero, the ASM count rate is reduced during the dip of 60% with respect to the persistent emission. Finally, the goodness of the two ephemerides allows us to observe the presence of a secondary dip at phase 0.55, which is typically observed in several dipping sources (see Grindlay 1989 [78], for XB 1916-053).

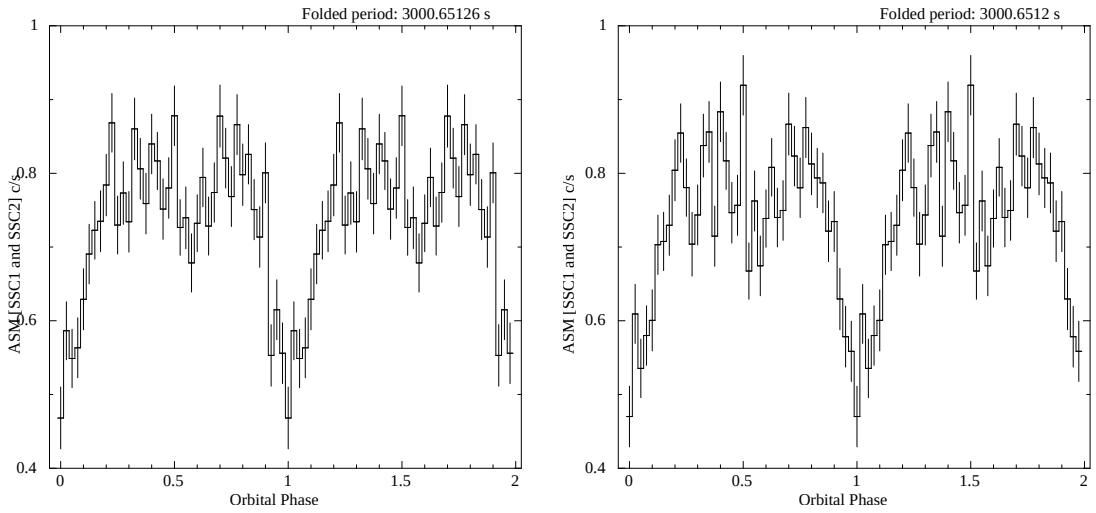

Figure 4.7: Folded RXTE/ASM light curve of XB 1916-053 selecting the events from SSC1 and SSC2. No energy filter is applied. Each phase-bin correspond to 75 s. Left panel: folded light curve using the LQS ephemeris (see 4.4). Right panel: folded light curve usig the LSe ephemeris (see 4.6)

4.5 Discussion

From the study of the 27 dip arrival times obtained from the pointed observations of XB 1916-053 and of the RXTE/ASM light curves, we find that the quadratic and cubic ephemerides do not correctly predict the dip arrival times on a long time span; whilst to well fit the delays, we need to use a function that contains at least linear and sinusoidal terms (LS ephemeris, see Eq. 4.3). The addition of a quadratic term to the LS ephemeris (Eq. 4.4) gives a probability of chance improvement obtained with a F-test of 1.7×10^{-3} with respect to the LS ephemeris. Finally, using the ephemeris shown in Eq. 4.6, the probability of chance improvement, also with respect to the LS ephemeris, is 1.7×10^{-2}. The LQS and LSe ephemerides paint two different physical scenarios for XB 1916-053. In the first case the orbital period derivative of the X-ray binary system is $\dot{P} = 1.44(7) \times 10^{-11}$ s/s and the observed delays associated with the dip arrival

times are affected by a relatively low-amplitude ($\sim$ 130 s) sinusoidal modulation with a period close to 26 yr. In the second case the orbital period derivative is fixed to zero and the modulation of the delays is solely sinusoidal with an amplitude of $\sim$ 550 s and an orbital period close to 51 yr. We explain in the following the sinusoidal modulation for both the scenarios, assuming the presence of a third body forming a hierarchical triple system with XB 1916-053, which alters the observed dip arrival times.

We start by discussing the plausible values of the companion star mass M_2. We know that the companion star is a degenerate star and its radius R_2 has to be equal to its Roche lobe radius R_L2 since the binary system is in the Roche lobe overflow (RLOF) regime. Rearranging the Eq. 3.3.15 in Shapiro & Teukolsky (1983) [96] the mass-radius relation for a degenerate star can be written as:

$$\frac{R_2}{R_\odot} = 0.04 \left(\frac{Z}{A}\right)^{5/3} \left(\frac{M_2}{M_\odot}\right)^{-1/3} = 0.0126(1+X)^{5/3} m_2^{-1/3}$$

where Z and A are the atomic number and the atomic weight of the matter composing the star and where we assumed that the matter is only composed of hydrogen and helium. The factor is the average of Z/A for matter composed of hydrogen and helium, X is the fraction of hydrogen in the star and, finally, m_2 is the companion star mass in units of solar mass. This equation has to be corrected for the thermal bloating factor f; which is the ratio of the companion star radius to the radius of a star with the same mass and composition, that is completely degenerate and supported only by the Fermi pressure of the electrons; then the factor f is 1. The Roche lobe radius of the companion star can be written as:

$$R_L2 = 0.46224a \left(\frac{m_2}{m_1 + m_2}\right)^{13}$$

where a is the orbital separation of the binary system and m_1 is the neutron star (NS) mass in unit of solar mass. We can write a in terms of the orbital period P, m_1 and m_2, using Kepler's third law. Combining the last two equations and Kepler's third law, we obtain:

$$m_2 = 0.0151(1+X)^{5/2} f^{3/2} \tag{4.7}$$

Nelemans et al. (2006)[97], analysing the optical spectrum with the European Southern Observatory Very Large Telescope, detected a He-dominated accretion

disc spectrum and suggested direct evidence for a helium donor. The authors found a good match with an LTE model consisting of pure helium plus overabundant nitrogen. For this reason, we assume X = 0 in the rest of the discussion.
The bolometric X-ray flux of XB 1916-053 was estimated by several authors. Galloway et al. (2008)[90], analysing a RXTE/PCA observation of XB 1916-053, determined a persistent flux in the 2.5-25 keV of $(3.82 \pm 0.04) \times 10^{-10} erg\, s^{-1} cm^{-2}$. The authors corrected the flux for a bolometric factor $c_{bol} = 1.37 \pm 0.09$ to estimate the bolometric flux in the 0.1-200 keV energy range, obtaining a bolometric flux of $(5.2 \pm 0.3) \times 10^{-10} erg\, s^{-1} cm^{-2}$. Recently, Zhang et al. (2014)[94], analysing a Suzaku observation of XB 1916-053, found a value of F_{bol} in the 0.1-200 keV energy range between $5.5 \times 10^{-10} erg\, s^{-1} cm^{-2}$ and $6.1 \times 10^{-10} erg\, s^{-1} cm^{-2}$. Finally, analysing the persistent emission of the source during a BeppoSAX observation, Church et al. (1998)[77] estimated a value of F_{bol} in the 0.5-200 keV energy range of $6.2 \times 10^{-10} erg\, s^{-1} cm^{-2}$. Since the RXTE/ASM light curve of XB 1916-053 shows that the count rate of the source is almost constant over more than ten years, we adopt a conservative value for the bolometric flux of $(5.5 \pm 0.5) \times 10^{-10} erg\, s^{-1} cm^{-2}$.
The distance d to the source was estimated by Galloway et al.(2008)[90] measuring the peak flux during the photospheric radius expansion (PRE) in type-I X-ray bursts. Equation 8 in Galloway et al.(2008)[90] can be rewritten as:

$$d = 8.32 \left(\frac{F_{pk,PRE}}{3 \times 10^{-8} erg\, s^{-1} cm^{-2}} \right)^{-1/2} m_1^{1/2} \left(1 - 0.296 \frac{m_1}{r_{PRE}} \right)^{1/4} (1+X)^{-1/2} kpc \tag{4.8}$$

where r_{PRE} is the photospheric radius of the neutron star in units of 10 km and $F_{pk,PRE}$ is the flux at the peak of the type-I X-ray burst during the PRE. The authors measured $F_{pk,PRE} = (2.9 \pm 0.4) \times 10^{-8} erg\, s^{-1} cm^{-2}$ and $r_{PRE} \simeq 1.1$ for XB 1916-053 and concluded that the distance to the source is $d = 8.9 \pm 1.3 kpc$ (adopting X = 0) for a NS mass of $1.4 M_\odot$.
The X-ray luminosity can be expressed as $L_x = 4\pi d^2 F_{bol}$, where we roughly assume that the emitted flux is isotropic. We obtain $L_x \simeq 5.2 \times 10^{36} erg\, s^{-1}$ for a NS mass of $1.4 M_\odot$, whilst we find $L_x \simeq 6.6 \times 10^{36} erg\, s^{-1}$ for a NS mass of $2.2 M_\odot$.
Rappaport et al. (1987)[98] predicted the X-ray luminosity for highly compact binary systems under the reasonable hypothesis that the main mechanism to lose angular momentum is gravitational radiation. Combining the Eqs. 8 and 13 in

their work, we obtain:

$$L_x \simeq \frac{5.2 \times 10^{42}}{1 - 1.5\alpha(1-\beta)} m_1^{5/3} P_m^{-14/3} (1+X)^5 \beta \eta f^3 erg\, s^{-1} \tag{4.9}$$

where P_m is the orbital period in units of minutes, β is the fraction of matter yielded by the companion star and accreted onto the NS, η is the efficiency for converting gravitational potential energy into X-ray emission, and α is the specific angular momentum carried away by the mass lost from the system, in units of $2\pi a^2/P_{orb}$, where a is the orbital separation (see Rappaport et al. (1987)[99]). In Eq.4.9 we assume that the NS radius is 10 km. Using the orbital period value of 3000.65 s, assuming $\eta = 1$ and a conservative mass transfer scenario ($\beta = 1$) (see chapter 2), we find that $L_x \simeq 1.1 \times 10^{35} f^3 ergs^{-1}$ and $L_x \simeq 2.3 \times 10^{35} f^3 ergs^{-1}$ for a NS mass of $1.4 M_\odot$ and $2.2 M_\odot$, respectively. Comparing the observed luminosity and the predicted luminosity, we estimate that $f = 3.6 \pm 0.4$ and $f = 3.0 \pm 0.3$ for a NS mass of $1.4 M_\odot$ and $2.2 M_\odot$, respectively. Substituting the obtained values of f in eq. 4.7, we obtain that the companion star mass is $M_2 = 0.10 \pm 0.02 M_\odot$ and $M_2 = 0.078 \pm 0.012 M_\odot$ for a NS mass of $1.4 M_\odot$ and $2.2 M_\odot$, respectively. The mass ratio $q = M_2/M_1$ of XB 1916-053 is between 0.036 ± 0.009 and 0.071 ± 0.009. Hu et al. (2008)[91] inferred the mass ratio of XB 1916-053 from the negative super-hump period and found $q \simeq 0.045$, which is compatible with our estimated range of values of q. Chou et al. (2001)[85] estimated a value of $q \simeq 0.022$ using the period of the apsidal precession of the accretion disc of $P_{prec} = 3.9087(8)$ d. The value of q obtained by Chou et al. (2001)[85] is outside the range that we find.

To estimate the orbital period derivative we use the eq. 11 shown in Rappaport et al. (1987)[98] that we rewrite as:

$$\dot{P} \simeq \frac{1.54 \times 10^{-9}}{1 - 1.5\alpha(1-\beta)} m_1^{2/3} P_m^{-8/3} (1+X)^{5/2} f^{3/2} s\, s^{-1} \tag{4.10}$$

Using the value of $\dot{P} \simeq 1.44 \times 10^{-11} s\, s^{-1}$ (LQS ephemeris) and the orbital period value of 3000.65 s, we find that the thermal bloating factor f is 40 and 32 for a NS mass of $1.4 M_\odot$ and $2.2 M_\odot$. These values of f are not physically plausible and suggest that, in a conservative mass transfer scenario, the value of the orbital period derivative cannot be that obtained from the LQS ephemeris. On the other hand, adopting an orbital period of 3000.65 s and a factor f of 3.6 and 3.0 for a NS mass of $1.4 M_\odot$ and $2.2 M_\odot$ we find $\dot{P} = (3.9 \pm 0.2) \times 10^{-13} s\, s^{-1}$ and $\dot{P} = (3.98 \pm$

$0.15) \times 10^{-13} s\, s^{-1}$ for a NS mass of $1.4 M_{\odot}$ and $2.2 M_{\odot}$, respectively. The orbital period derivative normalised to the orbital period is $\dot{P}/P \simeq 4.2 \times 10^{-9} yr^{-1}$ and weakly depends on the NS mass. We conclude that the conservative mass transfer scenario with a thermal bloating factor of the companion star between three and four allows us to explain the discrepancy between the predicted and observed X-ray luminosity, but it does not solve the discrepancy between the predicted and measured orbital period derivative obtained from the LQS ephemeris. For this reason, we investigate the non-conservative mass transfer scenario. Combining the eqs. 4.9 and 4.10, we obtain:

$$\frac{L_x}{\dot{P}} \simeq 3.38 \times 10^{51} m_1 P_m^{-2} \beta \eta f^{3/2} erg\, s^{-1} \tag{4.11}$$

Adopting $L_x \simeq 5.2 \times 10^{36} erg\, s^{-1}$, $\dot{P} = 1.44 \times 10^{-11} s\, s^{-1}$, P =3000.65 s and fixing $\eta = 1$, we find that $\beta f^{3/2} = 0.191$ for a NS mass of $1.4 M_{\odot}$. Since f 1, we expect that more than 81% of the mass yielded by the companion star leaves the system. Furthermore, since the measured values of L_x and $\dot{P}$ are positive, the term $1 - 1.5\alpha(1-\beta)$ in eqs. 4.9 and 4.10 should be positive. Solving for α while taking $\beta < 0.191$, we obtain that $\alpha < 0.823$. Because α is in units of $2\pi a^2/P_{orb}$, we find that the matter should leave the binary system from a distance d from the neutron star of $d \leqslant \alpha^{1/2} a$; the point of ejection in unit of orbital separation is $\overline{x} = d/a < \alpha^{1/2}$. In the rest of the discussion, we assume that the matter is ejected at the inner Lagrangian point x_{L1} of the binary system. We rewrite the eq. 4.9 as function of f using the condition $\beta f^{3/2} = 0.191$. We find:

$$L_x \simeq \frac{5.2 \times 10^{42}}{1 - 1.5\overline{x}_{L1}(1 - 0.191 f^{-3/2})} m_1^{5/3} P_m^{-14/3} 0.191 f^{3/2} erg\, s^{-1} \tag{4.12}$$

where $\overline{x}_{L1}$ is the position of the inner Lagrangian point in units of orbital separation. Using eq. 4.7 and a NS mass of $1.4 M_{\odot}$, $\overline{x}_{L1}$ can be written as a cubic function of f for values of the thermal bloating factor between 1 and 10. We find:

$$\overline{x}_{L1} = 0.915 - 6.87 \times 10^{-2} f + 6.61 \times 10^{-3} f^2 - 2.88 \times 10^{-4} f^3$$

with an accuracy of 2×10^{-3}. Combining the last equation and eq. 4.12, we infer the luminosity as function of f. We show L_x in units of $10^{36} erg\, s^{-1}$ versus f for a NS mass of $1.4 M_{\odot}$ (purple colour) in Fig. 4.8.

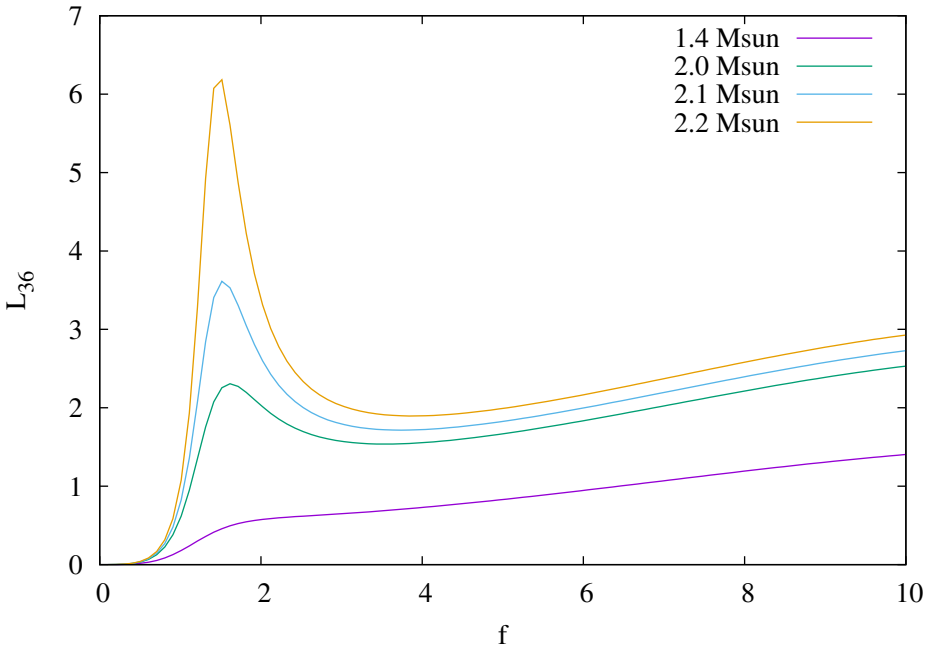

Figure 4.8: X-ray luminosity of XB 1916-053 in units of $10^{36} erg\, s^{-1}$ versus the thermal bloating factor f of the companion star. The four curves correspond to different values of the NS mass: purple, green, light blue, and gold colours correspond to a NS mass of 1.4, 2, 2.1, and 2.2 $M_{\odot}$, respectively. The peaks in the curves are at $f \simeq 1.5$.

Since the observed luminosity for a NS mass of $1.4M_{\odot}$ is larger than the predicted one for each value of f, also taking the corresponding error into account, we conclude that **this specific** non-conservative mass transfer scenario fails for a NS mass of $1.4M_{\odot}$. We repeat the same procedure for NS masses of 2, 2.1, 2.2 $M_{\odot}$, finding that the predicted and observed luminosities are only compatible in the case in which the NS mass is $\geqslant 2.2M_{\odot}$. In this case, we find that $\beta f^{3/2} = 0.154$, $\alpha < 0.784$ and:

$$\overline{x}_{L1} = 0.927 - 6.02 \times 10^{-2} f + 5.66 \times 10^{-3} f^2 - 2.88 \times 10^{-4} f^3$$

with an accuracy of 2×10^{-3}. The luminosity for a NS mass of $2.2M_{\odot}$ (gold colour) is shown in Fig.4.8. Furthermore, we plot the orbital period derivative as function of f for a NS mass of $2.1M_{\odot}$ (brown colour) and $2.2M_{\odot}$ (purple colour) in Fig.4.9.

We note that that only for a NS mass of $2.2M_{\odot}$ the predicted and measured $\dot{P}$ are compatible for $f \simeq 1.5$. We conclude that this non-conservative mass transfer scenario predicts the observed values of luminosity and orbital period

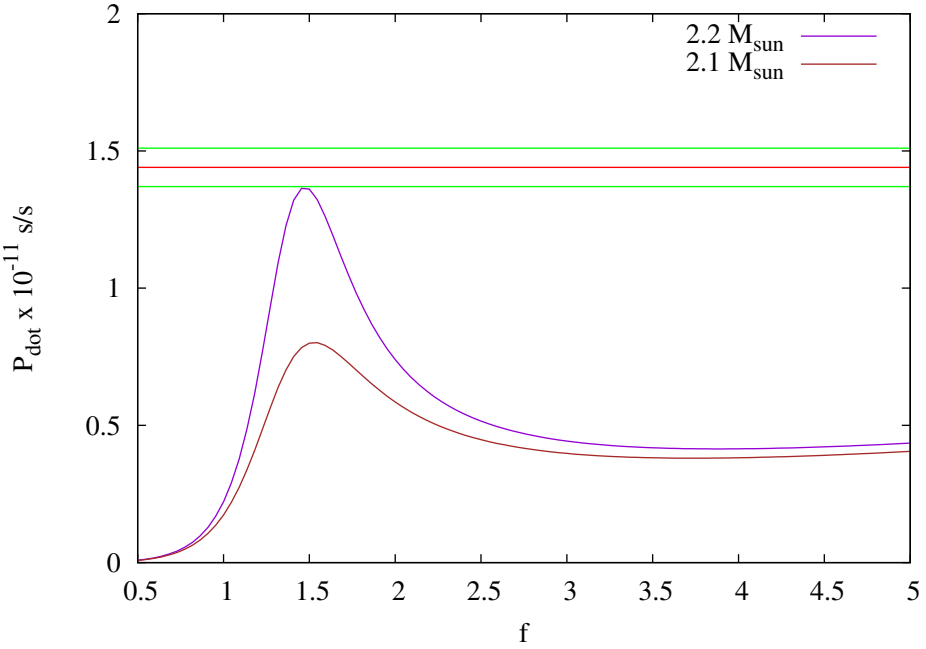

Figure 4.9: Orbital period derivative of XB 1916-053 in units of $10^{-11} s\, s^{-1}$ versus the thermal bloating factor f of the companion star. The brown and purple curves are obtained using a NS mass of 2.1 and 2.2 $M_\odot$. The red and green lines indicate the best-fit value and the values at 68% confidence level of the orbital period derivative obtained from the LQS ephemeris. The purple curve is compatible at 1σ with the measured orbital period derivative for $f \simeq 1.5$.

derivative only for NS masses larger than 2.2 $M_\odot$. For a NS mass of $2.2 M_\odot$, the companion star has a mass of $0.028 M_\odot$ and β is close to 0.084, which is more than 90% of the matter, yielded from the companion star, that leaves the binary system. In this scenario, we suggest that XB 1916-053 could be considered as a possible progenitor of the ultra-compact "Black Widow" pulsars with very low-mass companions.

Benvenuto et al. (2012)[100] proposed that a binary system with an initial orbital period of 0.8 d, composed of a $1.4 M_\odot$ NS and a companion star mass of $2 M_\odot$, evolves in $\sim$ 6.5 Gyr forming a binary system that well fits the known orbital parameters of the black widow millisecond pulsar PSR J1719-1438. We note that the same evolutive path fits the orbital parameters of XB 1916-053 at $\sim$ 5 Gyr from the initial time. At 5 Gyr, the predicted orbital period is 0.035 d, the predicted companion star mass is $0.03 M_\odot$, the NS mass is slightly larger than 2.2 $M_\odot$ (Benvenuto, private communication) and the companion star is helium

dominated. These values are very similar to those of XB 1916-053 shown in this work for a non-conservative mass transfer scenario, although a discrepancy between our estimation of $\dot{M}_2 \sim 4.1 \times 10^{-9} M_{\odot} yr^{-1}$ and the value suggested by Benvenuto et al. (2012)[100] at 5 Gyr ($\sim 10^{-10} M_{\odot} yr^{-1}$) is present. Furthermore, we note that as the spin period of PSR J1719-1438 is 5.7 ms (see Bailes et al. 2011, and references therein)[101] the spin period of the NS in XB 1916-053 could also be extremely short. Indeed, Galloway et al. (2001)[90] interpreted the asymptotic frequency of the coherent burst oscillations in terms of a decoupled surface burning layer and suggested that the NS could have a spin period around 3.7 ms. Nevertheless, we note that our solution for a non-conservative mass transfer scenario is not supported by a robust physical mechanism to explain the large quantity of matter ejected from the inner Lagrangian point. To date, only two physical mechanisms are known to be able to eject the transferred matter partially (or totally) . The first mechanism predicts that when a super-Eddington mass transfer occurs, the X-ray luminosity has to be at the Eddington limit. Then, the radiation pressure from the compact object pushes away part of the transferred matter from the binary system. This mechanism was recently invoked to explain the large orbital period derivative measured in the accretion disc corona (ADC) source X1822-371 by Burderi et al. (2010)[32], Iaria et al. (2013)[38], and Iaria et al. (2015) [26]. However, this mechanism cannot be applied in the case of XB 1916-053 because type-I X-ray bursts are observed in the light curve of the source (see e.g. Fig.4.10), whilst the stable burning sets in at high accretion rate values that are comparable to the Eddington limit (see Bildsten 2000, and references therein)[102].

Consequently, the mass transfer rate cannot be super-Eddington and this mechanism cannot justify a non-conservative mass transfer scenario. The second mechanism supposes that the X-ray binary system is a transient source and during the X-ray quiescence it is ejecting the transferred matter from the inner Lagrangian point due to the radiation pressure of the magneto-dipole rotator emission. This mechanism, which we call radio ejection after Burderi et al. (2001)[103], was proposed by Di Salvo et al. (2008)[104] to explain the large orbital period derivative measured in SAXJ1808.4-3658. However, this mechanism also fails to explain our results because XB 1916-053 is a persistent X-ray source.

Finally, we discuss the sinusoidal modulation observed in the LQS and LSe ephemerides. If we assume a conservative mass transfer scenario, the predicted

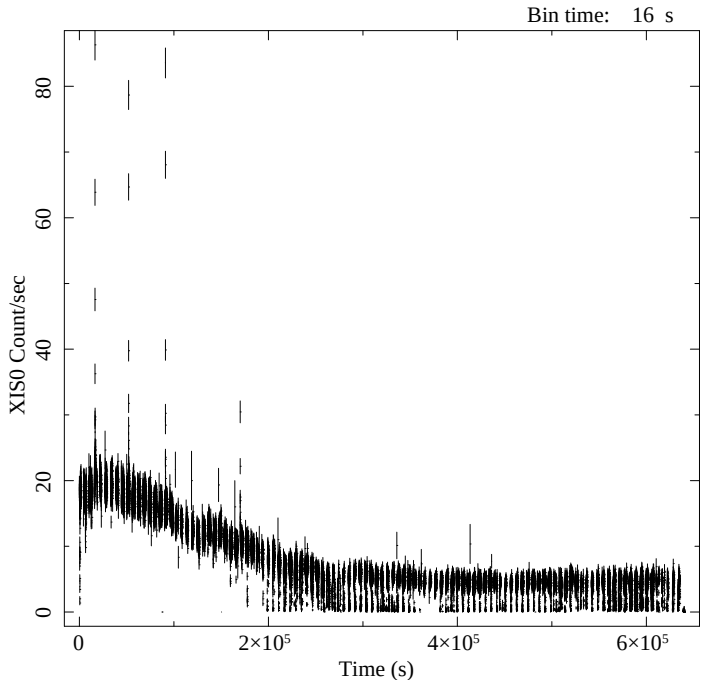

Figure 4.10: Suzaku XIS0 light curve of XB 1916-053 during the long observation on 2014 Oct.

orbital period derivative is close to $4 \times 10^{-13} s\, s^{-1}$ independent of the NS mass. Then we added a quadratic term to the LSe ephemeris to take the predicted value into account. We fitted again the delays using the relation:

$$y(t) = a + bt + ct^2 + \Delta_{DS}(t)$$

where the term c is fixed to $5 \times 10^{-7} s/d^2$. The fit parameters are reported in Tab. 4.5.

We note that the addition of the quadratic term does not significantly change the best-fit parameters. An explanation of the sinusoidal modulation obtained from the LSe ephemeris could be the presence of a third body gravitationally bound to the X-ray binary system. Assuming the existence of a third body of mass M_3, the binary system XB 1916-053 orbits around the new centre of mass (CM) of the triple system. The distance of XB 1916-053 from the new CM is given by $a_x = a_{bin} sini = Ac$, where i is the inclination angle of the orbit with respect to the line of sight, A is the amplitude of the sinusoidal function obtained from the ephemeris of eq. 4.9, and c is the light speed. We obtained $a_x = (1.60 \pm 0.13) \times 10^{13}$ cm for $P_{mod} = 18600$ d. We can write the mass function of the triple system as:

$$\frac{M_3 sin\, i}{(M_3 + M_{bin})^{2/3}} = \left(\frac{4\pi^2}{G}\right)^{1/3} \frac{a_x}{P_{mod}^{2/3}}$$

where M_3 is the third body mass, M_{bin} the binary system mass, and finally, P_{mod} is the orbital period of XB 1916-053 around the CM of the triple system. Substituting the values of M_{bin}, P_{mod} , a_x and assuming an inclination angle for the source of 70°, we find that M_3 is $\sim 0.10 M_\odot$ and $\sim 0.14 M_\odot$ for a NS mass of $1.4 M_\odot$ and $2.2 M_\odot$, respectively. We used also P_{mod} of 17100 d and 20100 d finding that the values of M_3 are substantially independent of the value of P_{mod}. For a non-conservative mass transfer scenario, we discuss the sinusoidal modulation obtained from the LQS ephemeris assuming a NS mass of $2.2 M_\odot$. In this case we find that $a_x = (3.9 \pm 0.5) \times 10^{12}$ cm and $M_3 \sim 0.055 M_\odot$ for an inclination angle of 70°.

4.6 Conclusions

We have systematically analysed all the historically reported X-ray light curves of XB 1916-053, which span 37 years. We find that the previously suggested quadratic ephemeris for this source no longer fits the dip arrival times.
We studied the conservative mass transfer scenario of the system, finding that the thermal bloating factor of the degenerate companion star is 3.6 and 3 for a NS mass of 1.4 and $2.2 M_\odot$. In this scenario, the predicted and observed luminosity are compatible ($\sim 5 - 7 \times 10^{36} erg\, s^{-1}$), although the orbital period derivative is a factor of 40 smaller than the value of $1.44 \times 10^{-11} s\, s^{-1}$ obtained fitting the delays with a quadratic plus a sinusoidal function (LQS ephemeris). If the conservative mass transfer scenario is correct, we conclude that the modulation of the delays associated with the dip arrivals time are solely due to a sinusoidal modulation caused by a third body orbiting around the binary system.
In this case we estimate the third body mass is 0.10 and 0.14 $M_\odot$ for NS masses of 1.4 and 2.2 $M_\odot$, respectively. The orbital period of the third body around XB 1916-053 is close to 55yr and the orbit shows an eccentricity $e = 0.28 \pm 0.15$.
In a non-conservative mass transfer scenario where the mass is ejected away from the inner Lagrangian point, we find that the observed luminosity and the orbital period derivative from the LQS ephemeris are possible only from a NS mass $\geqslant 2.2 M_\odot$. In this case we obtain that the thermal bloating factor of the degenerate companion star is $f \simeq 1.5$, the companion star mass is $0.028 M_\odot$, and

the fraction of matter yielded by the companion star and accreting onto the NS is $\beta = 0.084$. In this scenario, the sinusoidal modulation of the delays can be explained by the presence of a third body orbiting around XB 1916-053 with an period of 26 yr. We find that the third body mass is $0.055 M_{\odot}$. Finally, if the non-conservative mass transfer scenario is valid, we suggest that XB 1916-053 and the ultra-compact black widow system PSR J1719-1438 could be two different stages of the same evolutive path discussed by Benvenuto et al. (2012)[100]. If it is true, then the age of XB 1916-053 is close to 5 Gyr, whilst PSR J1719-1438 is ~ 6.5 Gyr old.

Point	Phase interval	$C_1(count\,s^{-1})$	$C_2(counts^{-1})$	$C_3(counts^{-1})$	ϕ_1	ϕ_2	ϕ_3	ϕ_4	$\chi^2_{red} d.o.f.$
1	0.7-1.7	7.23 ± 0.06	6.01 ± 0.09	7.59 ± 0.06	1.086 ± 0.012	1.113 ± 0.012	1.290 ± 0.012	1.388 ± 0.015	1.64(193)
2	0.7-1.7	5.74 ± 0.06	2.94 ± 0.13	5.75 ± 0.11	1.133 ± 0.004	1.170 ± 0.004	1.217 ± 0.005	1.263 ± 0.006	1.44(152)
3	0.1-1	11.24 ± 0.08	8.48 ± 0.12	11.14 ± 0.09	0.416 ± 0.006	0.450 ± 0.005	0.574 ± 0.006	0.603 ± 0.008	1.90(194)
4	0.8-1.8	23.02 ± 0.12	13.7 ± 0.4	23.73 ± 0.11	1.203 ± 0.003	1.239 ± 0.004	1.277 ± 0.003	1.321 ± 0.003	1.91(194)
5	0.095-0.8	14.6 ± 0.4	8.9 ± 0.3	17.7 ± 0.3	0.251 ± 0.015	0.329 ± 0.015	0.500 ± 0.008	0.576 ± 0.008	4.70(114)
6	0.1-0.8	25.6 ± 0.2	20.3 ± 0.4	27.1 ± 0.2	0.454 ± 0.007	0.487 ± 0.008	0.561 ± 0.007	0.605 ± 0.007	3.03(133)
7	0.5-1.1	72.9 ± 1.1	42.8 ± 1.0	75.6 ± 1.0	0.658 ± 0.004	0.680 ± 0.004	0.840 ± 0.009	0.940 ± 0.010	16.9(84)
8	0.5-1.2	107.1 ± 1.0	60.6 ± 1.3	106.3 ± 0.8	0.657 ± 0.007	0.805 ± 0.008	0.903 ± 0.004	0.954 ± 0.005	47.8(138)
9	0-1	6.05 ± 0.07	1.60 ± 0.06	6.15 ± 0.07	0.340 ± 0.008	0.535 ± 0.006	0.640 ± 0.004	0.752 ± 0.005	4.77(294)
10	0.6-1.4	9.3 ± 0.3	0.85 ± 0.05	9.3 ± 0.3	0.765 ± 0.004	0.809 ± 0.002	1.022 ± 0.003	1.100 ± 0.006	12.08(234)
11	0-1	41.00 ± 0.11	31.35 ± 0.11	45.06 ± 0.08	0.207 ± 0.004	0.323 ± 0.004	0.499 ± 0.002	0.611 ± 0.003	12.61(506)
12	0.1-1.1	36.60 ± 0.10	21.69 ± 0.13	37.45 ± 0.11	0.443 ± 0.003	0.569 ± 0.003	0.710 ± 0.002	0.808 ± 0.002	11.33(505)
13	0.95-1.95	0.986 ± 0.013	0.035 ± 0.003	0.982 ± 0.014	1.238 ± 0.004	1.340 ± 0.002	1.537 ± 0.002	1.647 ± 0.005	2.14(249)
14	0.24-0.75	27.6 ± 0.2	14.55 ± 0.10	27.7 ± 0.2	0.313 ± 0.003	0.433 ± 0.002	0.582 ± 0.002	0.705 ± 0.003	11.10(255)
15	0.15-1	36.51 ± 0.10	25.3 ± 0.2	38.31 ± 0.08	0.381 ± 0.004	0.566 ± 0.005	0.598 ± 0.003	0.738 ± 0.003	10.43(420)
16	0.35-0.9	25.4 ± 0.2	17.52 ± 0.10	26.9 ± 0.2	0.419 ± 0.004	0.489 ± 0.004	0.697 ± 0.003	0.763 ± 0.003	1.90(274)
17	0.9-1.9	1.030 ± 0.009	0.31 ± 0.02	1.016 ± 0.007	1.045 ± 0.004	1.160 ± 0.004	1.178 ± 0.004	1.272 ± 0.004	1.11(249)
18	0-1	23.75 ± 0.14	11.4 ± 0.3	24.40 ± 0.13	1.092 ± 0.002	1.113 ± 0.002	1.168 ± 0.005	1.281 ± 0.005	1.57(505)
19	0.6-1.6	28.8 ± 0.2	20.1 ± 0.2	29.8 ± 0.2	0.953 ± 0.004	0.985 ± 0.004	1.171 ± 0.006	1.249 ± 0.006	3.06(505)
20	0.1-1.1	69.9 ± 0.5	30.4 ± 0.5	72.4 ± 0.5	0.406 ± 0.004	0.506 ± 0.003	0.671 ± 0.003	0.730 ± 0.003	17.84(505)
21	0.2-1.2	0.0284 ± 0.0002	0.0256 ± 0.0004	0.0284 ± 0.0002	0.57 ± 0.02	0.63 ± 0.02	0.708 ± 0.014	0.733 ± 0.011	0.766(144)
22	0.3-1.3	9.92 ± 0.03	8.5 ± 0.2	10.04 ± 0.03	0.796 ± 0.005	0.835 ± 0.007	0.844 ± 0.013	0.923 ± 0.007	1.71(144)
23	0.9-1.9	15.10 ± 0.05	11.4 (fixed)	15.61 ± 0.05	1.263 ± 0.006	1.38 (fixed)	1.38 (fixed)	1.521 ± 0.006	2.41(505)
24	0.9-1.9	30.18 ± 0.13	23.1 ± 0.3	20.49 ± 0.15	1.322 ± 0.003	1.344 ± 0.003	1.499 ± 0.002	1.451 ± 0.002	1.22(505)
25	0.09-0.65	2.52 ± 0.03	0.759 ± 0.010	2.69 ± 0.04	0.194 ± 0.003	0.314 ± 0.002	0.525 ± 0.002	0.598 ± 0.003	2.39(567)
26	0.6-1.6	12.61 ± 0.11	4.4 ± 0.6	12.5 ± 0.2	1.025 ± 0.010	1.27 ± 0.02	1.295 ± 0.004	1.307 ± 0.004	4.08(171)
27	0.84-1.6	5.08 ± 0.04	1.607 ± 0.015	5.18 ± 0.02	0.909 ± 0.003	1.089 ± 0.002	1.2080 ± 0.0011	1.2904 ± 0.0014	3.29(382)

Table 4.2: Best-fit parameters obtained fitting the dips in the folded light curves.

Point	Dip Time (MJD;TDB)	Cycle	Delay (s)
1	43609.4168(12)	-187551	772 ± 74
2	44168.2535(5)	-171460	792 ± 28
3	44523.2941(5)	-161237	641 ± 42
4	45594.7744(3)	-130385	449 ± 18
5	46209.6271(13)	-112681	193 ± 112
6	46351.7778(9)	-108588	352 ± 52
7	47414.193(2)	-77997	162 ± 132
8	48146.539(3)	-56910	47 ± 182
9	48913.6127(10)	-34823	-140 ± 59
10	49109.1148(12)	-29165	-48 ± 76
11	50174.7555(5)	1490	-50 ± 46
12	50310.6187(4)	5402	-17 ± 37
13	50566.3680(4)	12766	-69 ± 39
14	51001.3241(5)	25290	-15 ± 40
15	51043.7292(5)	26511	-9 ± 45
16	52074.0935(3)	56179	151 ± 29
17	52183.7349(3)	59336	107 ± 28
18	52183.7008(2)	59335	162 ± 19
19	52542.2168(4)	69658	227 ± 39
20	52542.2860(11)	69660	202 ± 98
21	52957.9679(8)	81629	327 ± 69
22	53224.6246(4)	89307	467 ± 34
23	54048.3791(5)	113026	411 ± 39
24	55367.45218(15)	151007	593 ± 13
25	56459.9129(3)	182463	721 ± 20
26	56853.6454(8)	193800	821 ± 67
27	56949.84670(10)	196570	814 ± 8

Table 4.3: Journal of the X-ray dip arrival times of XB 1916-053. Epoch of reference 50 123:00873 MJD, orbital period 3000.6511 s.

Parameters	LQ	LQC	LS	LQS	LSe		
a (s)	78 ± 23	$-2.7^{+2.1}_{11.2}$	584 ± 157	16 ± 22	229 ± 336 56 ± 322	1.1 ± 299.2	
b ($\times 10^{-3} sd^{-1}$)	-4 ± 4	37.1 ± 0.4	-43 ± 23	-4 ± 3	3 ± 20	3 ± 19	5 ± 22
c ($\times 10^{-5} sd^{-2}$)	1.70 ± 0.09	2.13 ± 0.03	-	1.79 ± 0.09	-	-	-
d ($\times 10^{-9} sd^{-3}$)	-	-1.35 ± 0.12	-	-	-	-	-
A (s)	-	-	658 ± 206	130 ± 15	519 ± 47	548 ± 43	577 ± 43
t_ϕ (d)	-	-	3897 ± 332	1356 ± 203	-3723 ± 1100	-3150 ± 1116	-2923 ± 1034
P_{mod} (d)	-	-	20409 ± 3381	9302 ± 752	17100 (fixed)	18600 (fixed)	20100 (fixed)
ϖ(deg)	-	-	-	-	195 ± 26	210 ± 28	217 ± 27
e	-	-	-	-	0.26 ± 0.20	0.28 ± 0.15	0.32 ± 0.13
χ^2 (d.o.f.)	194.6(24)	92.4(23)	63.7(22)	39.4(21)	51.8(21)	48.2(21)	45.8(21)

Table 4.4: Best-fit values of the parameters of the functions used to fit the delays.The reported errors are at 68% confidence level. The fit parameters of the delays are obtained using LQ (column 2), LQC (column 3), LS (column 4), LQS function (column 5), and LSe (columns 6, 7, and 8), respectively.

Parameters	$P_{mod} = 17100$ d	$P_{mod} = 18600$ d	$P_{mod} = 20100$ d
a (s)	180 ± 332	21 ± 307	-27 ± 285
b ($\times 10^{-3}$ s/d)	2 ± 20	2 ± 19	4 ± 21
A (s)	506 ± 46	534 ± 43	562 ± 43
e	0.26 ± 0.20	0.28 ± 0.15	0.32 ± 0.13
ϖ(deg)	198 ± 27	213 ± 28	219 ± 27
t_ϕ (d)	-3594 ± 1129	-3036 ± 1131	-2825 ± 1042
$\chi^2(d.o.f.)$	51.3(21)	47.9(21)	45.5(21)
F-test prob.	3.5×10^{-2}	1.5×10^{-2}	0.8×10^{-2}

Table 4.5: Best-fit parameters of the delays assuming the presence of the third body in eccentric orbit and taking a quadratic term c=$5 \times 10^{-7} s/d^2$ into account. The reported errors are at 68% confidence level. The F-test probability is estimated with respect to the value of the LS ephemeris (the fourth column of Tab.4.4).

Chapter 5

Final conclusions

In this work we analyzed two low-mass binary systems containing neutron stars viewed at high inclination angle (an eclipsing source and a dipping source). These are X1822-371 and XB 1916-053, respectively. The study of high-inclination systems is very important to gain information on LMXBs in general, since their light curve show periodic signals, such as dips or eclipses, at the orbital period of the system. These periodic signals can be used infer the orbital period of the system and eventually to study its evolution or, more in general, to infer changes of the orbital period, which have a physical origin. The two sources of our sample are very interesting LMXBs. 4U 1822-371 is an eclipsing source, which also shows dips in the light curve, and is observed at a high inclination angle, more than 80 degree. It also shows coherent X-ray pulsations at the spin period of the neutron star, at about 0.5 s, and probably has an intermediate magnetic field. It is therefore a not yet recycled neutron star, and few sources like this are known in literature to date. The other source, XB 1916-053, is a dipper, with a less extreme inclination angle with respect to the previous one. It, however, belongs to the class of ultra-compact LMXB, with an orbital period of less than 1 h. This gives us the possibility to accurately study its orbital period changes, since relatively short observations can catch many orbital cycles and the statistics in the orbital light curve can be increased using folding techniques. In the following I describe in detail the conclusions of our study for both these sources.

5.0.1 X1822-371

We analysed the broadband X-ray spectrum of X1822-371, using all the presently available data sets, to understand the nature of the residuals between 0.6 and 0.8 keV previously observed in the XMM/EPIC-pn data by Iaria et al.,(2013) [38]. To fit the residuals between 0.6 and 0.8 keV, we added an absorption feature with Gaussian profile (`gabs` in XSPEC). We interpret the Gaussian feature in absorption as a cyclotron resonant scattering feature (CRSF) produced close to the neutron star surface and derive the magnetic field strength at the surface of the neutron star, $(8.8 \pm 0.3) \times 10^{10} G$ for a radius of 10 km. This is the first direct measurement of the magnetic field strength in this source and clearly indicates that the magnetic field in this source has an intermediate value between the very weak magnetic field of LMXBs, about $10^8 - 10^9$G, and the strong field of HMXBs, typically above 10^12G. These intermediate-magnetic field systems are quite rare in nature. Also, this is up to that the lowest magnetic field that has been directly measured through the detection of a cyclotron line, since cyclotron line are produced for magnetic field above 10^11G.

We also detected the spin period of X1822-371 and we obtained the value of 0.5928850(6) s. Using all the measurements known of the spin period of X1822-371, we estimated that the spin period derivative of the source, that is $-2.55(3) \times 10^{-12} s/s$, and this confirms that the neutron star is spinning up.

We constrain the neutron star (NS) mass assuming that the CRSF is produced at the NS surface. We find that the NS mass is between $1.61 \pm 0.15 M_\odot$ and $1.70 \pm 0.13 M_\odot$. The companion star mass is constrained between $0.44 \pm 0.03 M_\odot$ and $0.46 \pm 0.02 M_\odot$.

Finally, we note that our conclusions contrast with the recent results reported by Sasano et al. (2014)[39], who report a CRSF at 33 keV (and a corresponding NS-B field of $3 \times 10^{12} G$) in the Suzaku data also used in this work.

To address this point, we have analized the INTEGRAL spectrum combined with the XMM, Suzaku, and Chandra spectra. These do not show significant evidence of a CRSF at 33 keV. Furthermore, we also show from theoretical arguments that a CRSF at 33 keV is not consistent with the evidence that the NS in X1822-371 is spinning up.

5.0.2 XB1916-053

In this work we have analysed all the historically reported X-ray light curves of XB 1916-053, which span 37 years, and we find that the previously suggested quadratic ephemeris for this source no longer fits the dip arrival times. We conclude that the modulation of the delays associated with the dip arrival times are probably due to a sinusoidal modulation caused by a third body orbiting around the binary system. We estimate the third body mass is 0.10 and 0.14 $M_{\odot}$ for NS masses of 1.4 and 2.2 $M_{\odot}$, respectively. The orbital period of the third body around XB 1916-053 is close to 55yr and the orbit shows an eccentricity $e = 0.28 \pm 0.15$.

Appendix A

Orbital timing method

To analyze the periodic signatures in the light curve of the X-Ray sources it is to use the "Orbital timing method". The method consists to extract the dip (or eclipse) arrival times, calculate the number of cycles and the delays, construct a diagram of delays vs. cycles and then fit it to obtain the parameters that allow to understand the orbital period variation of binary systems.
Analysing the steps in details we have:

1- **Extracting the dip (or eclipse) arrival times** From light curves we isolate a dip (or eclipse) we fit the dips with a simple model consisting of a "step and ramp" function, where the count rates before, during, and after the dip are constant and the intensity changes linearly during the dip transitions. This model involves seven parameters: the count rate before, during, and after the dip, called C1 , C2 and C3 , respectively; the start and stop time of the ingress (t_1 and t_2) and, finally, the start and stop time of the egress (t_3 and t_4). The time of dip for each light curve was, therefore, calculated as the mean value of the two times t_2 e t_3, where the bottom of the dip strats and ends:

$$T_{dip} = \frac{t_2 + t_3}{2}$$

2- **Calculating the number of cycles and the delay** Suppose to have an estimate of the orbital period of the source, we denote this value with P_{Trial}, or trial period; we also choose an arbitrary instant of time, T_{Trial}, in which, for istance, a minimum is observed, that can be a dip (or an eclipse) in

the light curve. Since the dip (or eclipse) occurs periodically, with a period that we supposed to be equal to P_{Trial},then we expect the dip (or eclipse) is observed again at a time:

$$T_{dip} = T_{Trial} + P_{Trial} \times N$$

where N is a number which can vary from 0 to ∞. The integer part of N corresponds to the number of cycles, elapsed at the time of the dip, while the decimal part of N represents the delay in phase. This decimal part, converted in time, is the correction time (delay) with respect to the expected arrival time of the dip that is an integer number N of orbital period P_{Trial} after the starting time T_{Trial}, and is due to the fact that P_{Trial} does not coincide with the actual period of the system; in this way we obtain the real arrival time of the dip and therefore the phase of the dip with respect to the trial ephemeris.

3- **Delay-cycles diagram, fit and determination of the actual orbital period** The delay-cycles diagram for a binary system without appreciable changes in period is a straight line. If P_{Trial} is compatible with the orbital period any delay would be around zero. Consequently, building a diagram of phase delays as a function of the number of cycles we would obtain all the points on an horizontal line, with a scattering caused by statistical uncertainties, around zero. If P_{Trial} is not compatible with the orbital period, but differs from it of a costant quantity, the straight line in the delay-cycles plot will be downward or upward and the angular coefficient of the linear trend is the correction to the trial period in order to get the real period.

Performing a linear fit, you can get the values of the slope and the intercept of the straight line that interpolates points. These values represent, respectively, the correction to the orbital trial period, ΔP, and correction to the test time of the first dip, ΔT. Hence the orbital period and the actual time of the first dip can be calculated through the following simple relationships:

$$P_{real} = P_{Trial} + \Delta P \quad T_{real} = T_{Trial} + \Delta T$$

If you repeat the procedure using T_{real} and P_{real} as new reference time and period, iterating the process, the slope of the line gradually decreases, until all points will follow a constant trend close to zero.

In systems in which a mass transfer takes place, as we have seen in preceding paragraphs (see chapter 2), the orbital period is not constant, its time derivatives will be different from zero and the plot will not be a straight line. If the delay-cycles plot can be represented by a second-order polynomial, then the period of the binary system is changing linearly, that is with a costant first derivative. If the plot is a parabola with a concavity facing up, the period would be increasing, conversely, if the concavity is face down the period is decreasing and the quadratic term is proportional to the orbital period derivative; in this case the actual time of the first dip can be calculated through the following relationship:

$$T_{dip} = T_{Trial} + P_{Trial} \times N + \frac{1}{2} P_{Trial} \dot{P}_{Trial} \times N^2$$

A sinusoidal curve in the phase delays versus cycles would instead indicate a sinusoidal modulation of the orbital period which may be an indication of an other body orbiting the binary system and the actual arrival time of the dip will be:

$$T_{dip} = T_{Trial} + P_{Trial} \times N + \frac{1}{2} P_{Trial} \dot{P}_{Trial} \times N^2 + A sin \left[\frac{2\pi}{N_{mod}} N - \phi \right]$$

where $N_{mod} = P_{mod}/P_{Trial}$ and P_{mod} is the period of the sine function, while $\phi = 2\pi t_\phi / P_{mod}$ and t_ϕ is the time referred to T_{Trial} at which the sinusoidal function is null.

Appendix B

Folding method

Suppose to have a light curve, or counts versus time. The counts in each bin time δT in which the light curve is divided follow the Poisson statistic. In the bin δT_i we have therefore N_i counts with a standard deviation $\sigma = \sqrt{N_i}$. Assume that the source has a periodicity superimposed to a stable signal, for example, a peak that is repeated every period P. If the source is weak (or the period P is very small, so that few counts are present) the peak may be indistinguishable from statistical fluctuations associated with the counts. One way to highlight a periodic signal is significantly reduce statistical fluctuations. If it is known the period P of the signal, just divide the light curve in intervals of length P which can then be added together coherently. In making the average, the standard deviation associated with the single channel is reduced by a factor $\sqrt{N}$ in order to obtain $\sigma_{i,new} = \sigma_i/\sqrt{N}$. If the exact period it is not known and it is wrong by an amount δt, where Δt is a bin in the folded light curve, then at every period the signal is moved by the amount δt with respect to the previous one, that is, the signal is completely spreaded across all channels of folded light curve. The more we reduce the error on the determination of the period ($\delta P \ll \delta t$) the more the different signals will be added together coherently. Then you will see the signal go from a situation in which it is scattered in all channels to a situation in which it is correctly found in the right channel. In practice, we see how you make an operation of folding. We take a reference time T_0, called *epoch*, and such that, for example, it is near the beginning of the observation. For each channel we can calculate the phase:

$$I.\alpha = \frac{t_i - T_0}{P}$$

where t_i is the arrival time of the i-th signal, I is an integer and corresponds to the integer number of periods with respect to the beginning of the observation (not important) and α is the decimal part that represents the phase of the i-th channel in the signal profile (for t ranging from 0 to P, the phase will go from 0 to 1). Doing this for all channels and coherently summing those that fall in the same phase bin the folded light curve is obtained which corresponds, if the assumed period is the correct one, to the signal profile. We estimate the step δP with which it is appropriate to vary the trial period. Suppose we have an observation of total duration T and ask ourselves what is the maximum variation of the period δP which does not have any effect on the folded light curve. This should be such that the last channel of the last period (the one that suffers the most the error δP since these will sum up at every period) falls in the last channel of the folded light curve. So we find δP such that the last channel of the last period is shifted by one channel in the folded light curve. In the folded light curve we have n channels: $n = \dfrac{P}{\delta T}$, where δT is the width of the channel in the folded light curve. In our observation we have a number of periods given by: $N = T/P$. If we make a mistake δP on the period, the total error on the last period will be $N\delta P$. We impose that $N\delta P = \delta T$ (the final error is equal to the shift of one channel in the folded light curve):

$$\delta P = \frac{\delta T}{N} = \frac{P}{nN} = \frac{P^2}{nT}$$

So the step values $\delta P < \dfrac{P^2}{nT}$ will shift the last interval by less than one channel in the folded light curve, which therefore does not produce appreciable changes in the shape of the profile. On the other hand a coarse step on the period search is the one that corresponds to a shift of one period of the folded light curve:

$$N\delta P = P$$

therefore:

$$\delta P = \frac{P}{N} = \frac{P^2}{T}$$

Usually the search starts with a coarse step and then be refined to improve the measurement.

Bibliography

[1] W. Forman, C. Jones, L. Cominsky, P. Julien, S. Murray, G. Peters, H. Tananbaum, and R. Giacconi. The fourth Uhuru catalog of X-ray sources. *ApJS*, 38:357–412, December 1978. Available from World Wide Web: http://adsabs.harvard.edu/abs/1978ApJS...38..357F.

[2] Riccardo Giacconi, Herbert Gursky, Frank R. Paolini, and Bruno B. Rossi. Evidence for x rays from sources outside the solar system. *Phys. Rev. Lett.*, 9:439–443, Dec 1962. Available from World Wide Web: http://link.aps.org/doi/10.1103/PhysRevLett.9.439.

[3] Q. Z. Liu, J. van Paradijs, and E. P. J. van den Heuvel. Catalogue of Galactic low-mass X-ray binaries (Liu+, 2007). *VizieR Online Data Catalog*, 3469:90807–+, June 2007. Available from World Wide Web: http://adsabs.harvard.edu/abs/2007A%26A...469..807L.

[4] I. S. Shklovsky. On the Nature of the Source of X-Ray Emission of SCO XR-1. *ApJL*, 148:L1, April 1967. Available from World Wide Web: http://adsabs.harvard.edu/abs/1967ApJ...148L...1S.

[5] Nagase F. White, N. E. and A. N. Parmar. The properties of X-ray binaries. *X-ray binaries*, 1995.

[6] S. E. Gibson. Global Solar Wind Structure from Solar Minimum to Solar Maximum: Sources and Evolution. *SSR*, 97:69–79, May 2001. Available from World Wide Web: http://adsabs.harvard.edu/abs/2001SSRv...97...69G.

[7] H. V. D. Bradt and J. E. McClintock. The optical counterparts of compact galactic X-ray sources. *ARAA*, 21:13–66, 1983. Available from World Wide Web: http://adsabs.harvard.edu/abs/1983ARA%26A..21...13B.

[8] R.Staubert. Accreting neutron stars. *The universe in X-Rays*, Trumper e Hasinger.

[9] N. E. White and S. S. Holt. Accretion disk coronae. *ApJ*, 257:318–337, June 1982. Available from World Wide Web: http://adsabs.harvard.edu/abs/1982ApJ...257..318W.

[10] J. Frank, A. R. King, and J.-P. Lasota. The light curves of low-mass X-ray binaries. *AA*, 178:137–142, May 1987. Available from World Wide Web: http://adsabs.harvard.edu/abs/1987A%26A...178..137F.

[11] M. Camenzind. Compact object in astrophysics. *White dwarfs, neutron stars and black holes*, Springer, 2007.

[12] B. Paczyński. Gravitational Waves and the Evolution of Close Binaries. *actaa*, 17:287, 1967. Available from World Wide Web: http://adsabs.harvard.edu/abs/1967AcA....17..287P.

[13] C. D. Garmany, P. S. Conti, and P. Massey. Spectroscopic studies of O type stars. IX - Binary frequency. *ApJ*, 242:1063–1076, December 1980. Available from World Wide Web: http://adsabs.harvard.edu/abs/1980ApJ...242.1063G.

[14] H. A. Abt. Normal and abnormal binary frequencies. *ARAA*, 21:343–372, 1983. Available from World Wide Web: http://adsabs.harvard.edu/abs/1983ARA%26A..21..343A.

[15] J. E. Tohline. The Origin of Binary Stars. *ARAA*, 40:349–385, 2002. Available from World Wide Web: http://adsabs.harvard.edu/abs/2002ARA%26A..40..349T.

[16] Z. Kopal. *Close binary systems*. 1959. Available from World Wide Web: http://adsabs.harvard.edu/abs/1959cbs..book.....K.

[17] K. A. Postnov and L. R. Yungelson. The Evolution of Compact Binary Star Systems. *Living Reviews in Relativity*, 17:3, December 2014. Available from World Wide Web: http://adsabs.harvard.edu/abs/2014LRR....17...3P.

[18] A. Blaauw. On the origin of the O- and B-type stars with high velocities (the "run-away" stars), and some related problems. *Bain*, 15:265, May 1961. Available from World Wide Web: http://adsabs.harvard.edu/abs/1961BAN....15..265B.

[19] D. Bhattacharya and E. P. J. van den Heuvel. Formation and evolution of binary and millisecond radio pulsars. *PhysRep*, 203:1–124, 1991. Available from World Wide Web: http://adsabs.harvard.edu/abs/1991PhR...203....1B.

[20] T. M. Tauris and E. P. J. van den Heuvel. *Formation and evolution of compact stellar X-ray sources*, pages 623–665. April 2006. Available from World Wide Web: http://adsabs.harvard.edu/abs/2006csxs.book..623T.

[21] V. Kalogera and R. F. Webbink. Formation of Low-Mass X-Ray Binaries. II. Common Envelope Evolution of Primordial Binaries with Extreme Mass Ratios. *ApJ*, 493:351–367, January 1998. Available from World Wide Web: http://adsabs.harvard.edu/abs/1998ApJ...493..351K.

[22] J. Whelan and I. Iben, Jr. Binaries and Supernovae of Type I. *ApJ*, 186:1007–1014, December 1973. Available from World Wide Web: http://adsabs.harvard.edu/abs/1973ApJ...186.1007W.

[23] F. Verbunt. Origin and evolution of X-ray binaries and binary radio pulsars. *Araa*, 31:93–127, 1993. Available from World Wide Web: http://adsabs.harvard.edu/abs/1993ARA%26A..31...93V.

[24] A. R. King. The evolution of compact binaries. *QJRAS*, 29:1–25, March 1988. Available from World Wide Web: http://adsabs.harvard.edu/abs/1988QJRAS..29....1K.

[25] F. Verbunt and C. Zwaan. Magnetic braking in low-mass X-ray binaries. *AA*, 100:L7–L9, July 1981. Available from World Wide Web: http://adsabs.harvard.edu/abs/1981A%26A...100L...7V.

[26] R. Iaria, T. Di Salvo, M. Matranga, C. G. Galiano, A. D'Aí, A. Riggio, L. Burderi, A. Sanna, C. Ferrigno, M. Del Santo, F. Pintore, and N. R. Robba. A possible cyclotron resonance scattering feature near 0.7 keV in

X1822-371. *AAp*, 577:A63, May 2015. Available from World Wide Web: http://adsabs.harvard.edu/abs/2015A%26A...577A..63I.

[27] A. Papitto, A. D'Aì, S. Motta, A. Riggio, L. Burderi, T. di Salvo, T. Belloni, and R. Iaria. The spin and orbit of the newly discovered pulsar IGR J17480-2446. *AA*, 526:L3, February 2011. Available from World Wide Web: http://adsabs.harvard.edu/abs/2011A%26A...526L...3P.

[28] W. Cui. Evidence for "Propeller" Effects in X-Ray Pulsars GX 1+4 and GRO J1744-28. *ApJ*, 482:L163–L166, June 1997. Available from World Wide Web: http://adsabs.harvard.edu/abs/1997ApJ...482L.163C.

[29] P. G. Jonker and M. van der Klis. Discovery of an X-Ray Pulsar in the Low-Mass X-Ray Binary 2A 1822-371. *ApJL*, 553:L43–L46, May 2001. Available from World Wide Web: http://adsabs.harvard.edu/abs/2001ApJ...553L..43J.

[30] C. Jain, B. Paul, and A. Dutta. New measurement of orbital and spin period evolution of the accretion disc corona source 4U 1822-37. *MNRAS*, 409:755–762, December 2010. Available from World Wide Web: http://adsabs.harvard.edu/abs/2010MNRAS.409..755J.

[31] R. Iaria, T. di Salvo, L. Burderi, A. D'Aí, A. Papitto, A. Riggio, and N. R. Robba. Detailed study of the X-ray and optical/UV orbital ephemeris of X1822-371. *AA*, 534:A85, October 2011. Available from World Wide Web: http://adsabs.harvard.edu/abs/2011A%26A...534A..85I.

[32] L. Burderi, T. di Salvo, A. Riggio, A. Papitto, R. Iaria, A. D'Aı, and M. T. Menna. New ephemeris of the ADC source 2A 1822-371: a stable orbital-period derivative over 30 years. *AA*, 515:A44, June 2010. Available from World Wide Web: http://adsabs.harvard.edu/abs/2010A%26A...515A..44B.

[33] A. J. Bayless, E. L. Robinson, R. I. Hynes, T. A. Ashcraft, and M. E. Cornell. The Structure of the Accretion Disk in the Accretion Disk Corona X-ray Binary 4U 1822-371 at Optical and Ultraviolet Wavelengths. *ApJ*, 709:251–262, January 2010. Available from World Wide Web: http://adsabs.harvard.edu/abs/2010ApJ...709..251B.

[34] C. Hellier and K. O. Mason. EXOSAT observations of X1822-371 - Modelling of the accretion disc rim. *MNRAS*, 239:715–732, August 1989. Available from World Wide Web: http://adsabs.harvard.edu/abs/1989MNRAS.239..715H.

[35] S. Heinz and M. A. Nowak. The Flared Disc Project: RXTE and ASCA observations of X 1822-371. *MNRAS*, 320:249–260, January 2001. Available from World Wide Web: http://adsabs.harvard.edu/abs/2001MNRAS.320..249H.

[36] A. N. Parmar, T. Oosterbroek, S. Del Sordo, A. Segreto, A. Santangelo, D. Dal Fiume, and M. Orlandini. Broad-band BeppoSAX observation of the low-mass X-ray binary X 1822-371. *AA*, 356:175–180, April 2000. Available from World Wide Web: http://adsabs.harvard.edu/abs/2000A%26A...356..175P.

[37] R. Iaria, T. Di Salvo, L. Burderi, and N. R. Robba. Partially Absorbed Comptonization Spectrum from the Nearly Edge-on Source X1822-371. *ApJ*, 557:24–29, August 2001. Available from World Wide Web: http://adsabs.harvard.edu/abs/2001ApJ...557...24I.

[38] R. Iaria, T. Di Salvo, A. D'Aì, L. Burderi, T. Mineo, A. Riggio, A. Papitto, and N. R. Robba. X-ray spectroscopy of the ADC source X1822-371 with Chandra and XMM-Newton. *AA*, 549:A33, January 2013. Available from World Wide Web: http://adsabs.harvard.edu/abs/2013A%26A...549A..33I.

[39] M. Sasano, K. Makishima, S. Sakurai, Z. Zhang, and T. Enoto. Suzaku view of the neutron star in the dipping source 4U 1822-37. *PASJ*, 66:35, April 2014. Available from World Wide Web: http://adsabs.harvard.edu/abs/2014PASJ...66...35S.

[40] K. Koyama, H. Tsunemi, T. Dotani, M. W. Bautz, K. Hayashida, T. G. Tsuru, H. Matsumoto, Y. Ogawara, G. R. Ricker, J. Doty, S. E. Kissel, R. Foster, H. Nakajima, H. Yamaguchi, H. Mori, M. Sakano, K. Hamaguchi, M. Nishiuchi, E. Miyata, K. Torii, M. Namiki, S. Katsuda, D. Matsuura, T. Miyauchi, N. Anabuki, N. Tawa, M. Ozaki, H. Murakami, Y. Maeda, Y. Ichikawa, G. Y. Prigozhin, E. A. Boughan, B. Lamarr, E. D. Miller,

B. E. Burke, J. A. Gregory, A. Pillsbury, A. Bamba, J. S. Hiraga, A. Senda, H. Katayama, S. Kitamoto, M. Tsujimoto, T. Kohmura, Y. Tsuboi, and H. Awaki. X-Ray Imaging Spectrometer (XIS) on Board Suzaku. *PASJ*, 59:23–33, January 2007. Available from World Wide Web: http://adsabs.harvard.edu/abs/2007PASJ...59S..23K.

[41] T. Takahashi, K. Abe, M. Endo, Y. Endo, Y. Ezoe, Y. Fukazawa, M. Hamaya, S. Hirakuri, S. Hong, M. Horii, H. Inoue, N. Isobe, T. Itoh, N. Iyomoto, T. Kamae, D. Kasama, J. Kataoka, H. Kato, M. Kawaharada, N. Kawano, K. Kawashima, S. Kawasoe, T. Kishishita, T. Kitaguchi, Y. Kobayashi, M. Kokubun, J. Kotoku, M. Kouda, A. Kubota, Y. Kuroda, G. Madejski, K. Makishima, K. Masukawa, Y. Matsumoto, T. Mitani, R. Miyawaki, T. Mizuno, K. Mori, M. Mori, M. Murashima, T. Murakami, K. Nakazawa, H. Niko, M. Nomachi, Y. Okada, M. Ohno, K. Oonuki, N. Ota, H. Ozawa, G. Sato, S. Shinoda, M. Sugiho, M. Suzuki, K. Taguchi, H. Takahashi, I. Takahashi, S. Takeda, K.-I. Tamura, T. Tamura, T. Tanaka, C. Tanihata, M. Tashiro, Y. Terada, S. Tominaga, Y. Uchiyama, S. Watanabe, K. Yamaoka, T. Yanagida, and D. Yonetoku. Hard X-Ray Detector (HXD) on Board Suzaku. *PASJ*, 59:35–51, January 2007. Available from World Wide Web: http://adsabs.harvard.edu/abs/2007PASJ...59S..35T.

[42] E. Boldt. The cosmic X-ray background. In A. Hewitt, G. Burbidge, and L. Z. Fang, editors, *Observational Cosmology*, volume 124 of *IAU Symposium*, pages 611–615, 1987. Available from World Wide Web: http://adsabs.harvard.edu/abs/1987IAUS..124..611B.

[43] L. Strüder, U. Briel, K. Dennerl, R. Hartmann, E. Kendziorra, N. Meidinger, E. Pfeffermann, C. Reppin, B. Aschenbach, W. Bornemann, H. Bräuninger, W. Burkert, M. Elender, M. Freyberg, F. Haberl, G. Hartner, F. Heuschmann, H. Hippmann, E. Kastelic, S. Kemmer, G. Kettenring, W. Kink, N. Krause, S. Müller, A. Oppitz, W. Pietsch, M. Popp, P. Predehl, A. Read, K. H. Stephan, D. Stötter, J. Trümper, P. Holl, J. Kemmer, H. Soltau, R. Stötter, U. Weber, U. Weichert, C. von Zanthier, D. Carathanassis, G. Lutz, R. H. Richter, P. Solc, H. Böttcher, M. Kuster, R. Staubert, A. Abbey, A. Holland, M. Turner, M. Balasini, G. F. Bignami,

N. La Palombara, G. Villa, W. Buttler, F. Gianini, R. Lainé, D. Lumb, and P. Dhez. The European Photon Imaging Camera on XMM-Newton: The pn-CCD camera. *AA*, 365:L18–L26, January 2001. Available from World Wide Web: http://adsabs.harvard.edu/abs/2001A%26A...365L..18S.

[44] A. Brinkman, H. Aarts, A. den Boggende, T. Bootsma, L. Dubbeldam, J. den Herder, J. Kaastra, P. de Korte, B. van Leeuwen, R. Mewe, F. Paerels, C. de Vries, J. Cottam, T. Decker, S. Kahn, A. Rasmussen, J. Spodek, G. Branduardi-Raymont, P. Guttridge, K. Thomsen, A. Zehnder, and M. Guedel. The Reflection Grating Spectrometer onboard XMM. In *Science with XMM*, 1998. Available from World Wide Web: http://adsabs.harvard.edu/abs/1998sxmm.confE...2B.

[45] C. Winkler, T. J.-L. Courvoisier, G. Di Cocco, N. Gehrels, A. Giménez, S. Grebenev, W. Hermsen, J. M. Mas-Hesse, F. Lebrun, N. Lund, G. G. C. Palumbo, J. Paul, J.-P. Roques, H. Schnopper, V. Schönfelder, R. Sunyaev, B. Teegarden, P. Ubertini, G. Vedrenne, and A. J. Dean. The INTEGRAL mission. *AA*, 411:L1–L6, November 2003. Available from World Wide Web: http://cdsads.u-strasbg.fr/abs/2003A%26A...411L...1W.

[46] P. Ubertini, F. Lebrun, G. Di Cocco, A. Bazzano, A. J. Bird, K. Broenstad, A. Goldwurm, G. La Rosa, C. Labanti, P. Laurent, I. F. Mirabel, E. M. Quadrini, B. Ramsey, V. Reglero, L. Sabau, B. Sacco, R. Staubert, L. Vigroux, M. C. Weisskopf, and A. A. Zdziarski. IBIS: The Imager on-board INTEGRAL. *AA*, 411:L131–L139, November 2003. Available from World Wide Web: http://cdsads.u-strasbg.fr/abs/2003A%26A...411L.131U.

[47] N. Lund, C. Budtz-Jørgensen, N. J. Westergaard, S. Brandt, I. L. Rasmussen, A. Hornstrup, C. A. Oxborrow, J. Chenevez, P. A. Jensen, S. Laursen, K. H. Andersen, P. B. Mogensen, I. Rasmussen, K. Omø, S. M. Pedersen, J. Polny, H. Andersson, T. Andersson, V. Kämäräinen, O. Vilhu, J. Huovelin, S. Maisala, M. Morawski, G. Juchnikowski, E. Costa, M. Feroci, A. Rubini, M. Rapisarda, E. Morelli, V. Carassiti, F. Frontera, C. Pelliciari, G. Loffredo, S. Martínez Núñez, V. Reglero, T. Velasco, S. Larsson, R. Svensson, A. A. Zdziarski, A. Castro-Tirado, P. Attina, M. Goria, G. Giulianelli, F. Cordero, M. Rezazad, M. Schmidt, R. Carli, C. Gomez,

P. L. Jensen, G. Sarri, A. Tiemon, A. Orr, R. Much, P. Kretschmar, and H. W. Schnopper. JEM-X: The X-ray monitor aboard INTEGRAL. *AA*, 411:L231–L238, November 2003. Available from World Wide Web: http://cdsads.u-strasbg.fr/abs/2003A%26A...411L.231L.

[48] F. Lebrun, J. P. Leray, P. Lavocat, J. Crétolle, M. Arquès, C. Blondel, C. Bonnin, A. Bouère, C. Cara, T. Chaleil, F. Daly, F. Desages, H. Dzitko, B. Horeau, P. Laurent, O. Limousin, F. Mathy, V. Mauguen, F. Meignier, F. Molinié, E. Poindron, M. Rouger, A. Sauvageon, and T. Tourrette. ISGRI: The INTEGRAL Soft Gamma-Ray Imager. *AA*, 411:L141–L148, November 2003. Available from World Wide Web: http://cdsads.u-strasbg.fr/abs/2003A%26A...411L.141L.

[49] T. J.-L. Courvoisier, R. Walter, V. Beckmann, A. J. Dean, P. Dubath, R. Hudec, P. Kretschmar, S. Mereghetti, T. Montmerle, N. Mowlavi, S. Paltani, A. Preite Martinez, N. Produit, R. Staubert, A. W. Strong, J.-P. Swings, N. J. Westergaard, N. White, C. Winkler, and A. A. Zdziarski. The INTEGRAL Science Data Centre (ISDC). *AA*, 411:L53–L57, November 2003. Available from World Wide Web: http://cdsads.u-strasbg.fr/abs/2003A%26A...411L..53C.

[50] L. Titarchuk. Generalized Comptonization models and application to the recent high-energy observations. *ApJ*, 434:570–586, October 1994. Available from World Wide Web: http://cdsads.u-strasbg.fr/abs/1994ApJ...434..570T.

[51] K. A. Arnaud. XSPEC: The First Ten Years. In G. H. Jacoby and J. Barnes, editors, *Astronomical Data Analysis Software and Systems V*, volume 101 of *Astronomical Society of the Pacific Conference Series*, page 17, 1996. Available from World Wide Web: http://adsabs.harvard.edu/abs/1996ASPC..101...17A.

[52] M. Asplund, N. Grevesse, A. J. Sauval, and P. Scott. The Chemical Composition of the Sun. *ARAA*, 47:481–522, September 2009. Available from World Wide Web: http://adsabs.harvard.edu/abs/2009ARA%26A..47..481A.

[53] D. A. Verner, G. J. Ferland, K. T. Korista, and D. G. Yakovlev. Atomic Data for Astrophysics. II. New Analytic FITS for Photoionization Cross Sections of Atoms and Ions. *ApJ*, 465:487, July 1996. Available from World Wide Web: http://adsabs.harvard.edu/abs/1996ApJ...465..487V.

[54] T. Mihara, K. Makishima, T. Ohashi, T. Sakao, and M. Tashiro. New observations of the cyclotron absorption feature in Hercules X-1. *Nature*, 346:250–252, July 1990. Available from World Wide Web: http://adsabs.harvard.edu/abs/1990Natur.346..250M.

[55] T. Muñoz-Darias, J. Casares, and I. G. Martínez-Pais. The "K-Correction" for Irradiated Emission Lines in LMXBs: Evidence for a Massive Neutron Star in X1822-371 (V691 CrA). *ApJ*, 635:502–507, December 2005. Available from World Wide Web: http://adsabs.harvard.edu/abs/2005ApJ...635..502M.

[56] P. Ghosh and F. K. Lamb. Plasma physics of accreting neutron stars. In J. Ventura and D. Pines, editors, *NATO Advanced Science Institutes (ASI) Series C*, volume 344 of *NATO Advanced Science Institutes (ASI) Series C*, page 363, 1991. Available from World Wide Web: http://adsabs.harvard.edu/abs/1991ASIC..344..363G.

[57] L. Burderi, T. Di Salvo, N. R. Robba, S. Del Sordo, A. Santangelo, and A. Segreto. Temporal Analysis of EXO 0531-66 in Outburst. *ApJ*, 498:831–836, May 1998. Available from World Wide Web: http://adsabs.harvard.edu/abs/1998ApJ...498..831B.

[58] P. Ghosh and F. K. Lamb. Accretion by rotating magnetic neutron stars. III - Accretion torques and period changes in pulsating X-ray sources. *ApJ*, 234:296–316, November 1979. Available from World Wide Web: http://adsabs.harvard.edu/abs/1979ApJ...234..296G.

[59] J. M. Lattimer and B. F. Schutz. Constraining the Equation of State with Moment of Inertia Measurements. *ApJ*, 629:979–984, August 2005. Available from World Wide Web: http://adsabs.harvard.edu/abs/2005ApJ...629..979L.

[60] P. G. Jonker, M. van der Klis, and P. J. Groot. The mass of the neutron star in the low-mass X-ray binary 2A 1822 - 371. *MNRAS*, 339:663–668, March 2003.

[61] A. Somero, P. Hakala, P. Muhli, P. Charles, and O. Vilhu. Phase-resolved optical and X-ray spectroscopy of low-mass X-ray binary X1822-371. *AA*, 539:A111, March 2012. Available from World Wide Web: http://adsabs.harvard.edu/abs/2012A%26A...539A.111S.

[62] A. W. Steiner, J. M. Lattimer, and E. F. Brown. The Equation of State from Observed Masses and Radii of Neutron Stars. *ApJ*, 722:33–54, October 2010. Available from World Wide Web: http://adsabs.harvard.edu/abs/2010ApJ...722...33S.

[63] P. Meszaros. Books-Received - High Energy Radiation from Magnetized Neutron Stars. *Journal of the British Astronomical Association*, 102:287, October 1992. Available from World Wide Web: http://adsabs.harvard.edu/abs/1992JBAA..102..287M.

[64] A. Manousakis, R. Walter, M. Audard, and T. Lanz. Pulsed thermal emission from the accreting pulsar XMMU J054134.7-682550. *AA*, 498:217–222, April 2009. Available from World Wide Web: http://adsabs.harvard.edu/abs/2009A%26A...498..217M.

[65] M. E. DeCesar, P. T. Boyd, K. Pottschmidt, J. Wilms, S. Suchy, and M. C. Miller. The Be/X-Ray Binary Swift J1626.6-5156 as a Variable Cyclotron Line Source. *ApJ*, 762:61, January 2013. Available from World Wide Web: http://adsabs.harvard.edu/abs/2013ApJ...762...61D.

[66] F. Fürst, K. Pottschmidt, J. Wilms, J. Kennea, M. Bachetti, E. Bellm, S. E. Boggs, D. Chakrabarty, F. E. Christensen, W. W. Craig, C. J. Hailey, F. Harrison, D. Stern, J. A. Tomsick, D. J. Walton, and W. Zhang. NuSTAR Discovery of a Cyclotron Line in KS 1947+300. *ApJ*, 784:L40, April 2014. Available from World Wide Web: http://adsabs.harvard.edu/abs/2014ApJ...784L..40F.

[67] A. Tiengo, P. Esposito, S. Mereghetti, R. Turolla, L. Nobili, F. Gastaldello, D. Götz, G. L. Israel, N. Rea, L. Stella, S. Zane, and G. F. Bignami. A

variable absorption feature in the X-ray spectrum of a magnetar. *Nature*, 500:312–314, August 2013. Available from World Wide Web: http://adsabs.harvard.edu/abs/2013Natur.500..312T.

[68] D. Sanwal, G. G. Pavlov, V. E. Zavlin, and M. A. Teter. Discovery of Absorption Features in the X-Ray Spectrum of an Isolated Neutron Star. *ApJ*, 574:L61–L64, July 2002. Available from World Wide Web: http://adsabs.harvard.edu/abs/2002ApJ...574L..61S.

[69] S. Mereghetti, A. De Luca, P. A. Caraveo, W. Becker, R. Mignani, and G. F. Bignami. Pulse Phase Variations of the X-Ray Spectral Features in the Radio-quiet Neutron Star 1E 1207-5209. *ApJ*, 581:1280–1285, December 2002. Available from World Wide Web: http://adsabs.harvard.edu/abs/2002ApJ...581.1280M.

[70] R. Iaria, T. Di Salvo, A. F. Gambino, M. Del Santo, P. Romano, M. Matranga, C. G. Galiano, F. Scarano, A. Riggio, A. Sanna, F. Pintore, and L. Burderi. Signature of the presence of a third body orbiting around XB 1916-053. *AA*, 582:A32, October 2015. Available from World Wide Web: http://adsabs.harvard.edu/abs/2015A%26A...582A..32I.

[71] R. H. Becker, B. W. Smith, J. H. Swank, E. A. Boldt, S. S. Holt, P. J. Serlemitsos, and S. H. Pravdo. Spectral characteristics of 3U 1915-05, a burst source candidate. *ApJl*, 216:L101–L104, September 1977. Available from World Wide Web: http://adsabs.harvard.edu/abs/1977ApJ...216L.101B.

[72] A. P. Smale, K. O. Mason, N. E. White, and M. Gottwald. X-ray observations of the 50-min dipping source XB1916-053. *MNRAS*, 232:647–660, June 1988. Available from World Wide Web: http://adsabs.harvard.edu/abs/1988MNRAS.232..647S.

[73] K. Yoshida. PhD thesis, Thesis, Tokyo University, (1993), 1993. Available from World Wide Web: http://adsabs.harvard.edu/abs/1993PhDT.....80Y.

[74] D. Barret, J. E. Grindlay, M. Strickman, and G. Vedrenne. CGRO/OSSE observations of the X-ray burster 4U 1915-05 (XB 1916-053). *AAps*,

120:269–273, December 1996. Available from World Wide Web: http://adsabs.harvard.edu/abs/1996A%26AS..120C.269B.

[75] F. M. Walter, K. O. Mason, J. T. Clarke, J. Halpern, J. E. Grindlay, S. Bowyer, and J. P. Henry. Discovery of a 50 minute binary period and a likely 22 magnitude optical counterpart for the X-ray burster 4U 1915-05. *ApJl*, 253:L67–L71, February 1982. Available from World Wide Web: http://adsabs.harvard.edu/abs/1982ApJ...253L..67W.

[76] N. E. White and J. H. Swank. The discovery of 50 minute periodic absorption events from 4U 1915-05. *ApJl*, 253:L61–L66, February 1982. Available from World Wide Web: http://adsabs.harvard.edu/abs/1982ApJ...253L..61W.

[77] M. J. Church, T. Dotani, M. BaŁuciŃska-Church, K. Mitsuda, T. Takahashi, H. Inoue, and K. Yoshida. Simple Photoelectric Absorption during Dipping in the ASCA Observation of XB 1916-053. *ApJ*, 491:388–394, December 1997. Available from World Wide Web: http://adsabs.harvard.edu/abs/1997ApJ...491..388C.

[78] J. E. Grindlay. Studies of the possible X ray triple 4U1915-05. In J. Hunt and B. Battrick, editors, *Two Topics in X-Ray Astronomy, Volume 1: X Ray Binaries. Volume 2: AGN and the X Ray Background*, volume 296 of *ESA Special Publication*, November 1989. Available from World Wide Web: http://adsabs.harvard.edu/abs/1989ESASP.296..121G.

[79] J. E. Grindlay, H. Cohn, and P. Schmidtke. Optical Counterpart of 4U 1915-05. *IAUcirc*, 4393, May 1987. Available from World Wide Web: http://adsabs.harvard.edu/abs/1987IAUC.4393....1G.

[80] J. H. Swank, R. E. Taam, and N. E. White. MXB 1916-053/4U 1915-05 - Burst properties and constraints on a 50 minute binary secondary. *ApJ*, 277:274–285, February 1984. Available from World Wide Web: http://adsabs.harvard.edu/abs/1984ApJ...277..274S.

[81] B. Paczynski and R. Sienkiewicz. Gravitational radiation and the evolution of cataclysmic binaries. *ApJl*, 248:L27–L30, August 1981. Available from World Wide Web: http://adsabs.harvard.edu/abs/1981ApJ...248L..27P.

[82] J. E. Grindlay, C. D. Bailyn, H. Cohn, P. M. Lugger, J. R. Thorstensen, and G. Wegner. Discovery of a possible X-ray triple - 4U 1915-05. *ApJl*, 334:L25–L29, November 1988. Available from World Wide Web: http://adsabs.harvard.edu/abs/1988ApJ...334L..25G.

[83] N. E. White. X-ray binaries. *AApr*, 1:85–110, April 1989. Available from World Wide Web: http://adsabs.harvard.edu/abs/1989A%26ARv...1...85W.

[84] P. J. Callanan, J. E. Grindlay, and A. M. Cool. Optical Observations of 4U 1915-05, and the Stability of the Long Term Ephemeris. *PASJ*, 47:153–162, April 1995. Available from World Wide Web: http://adsabs.harvard.edu/abs/1995PASJ...47..153C.

[85] Y. Chou, J. E. Grindlay, and P. F. Bloser. Timing Analysis of the Light Curve of the Dipping-Bursting X-Ray Binary X1916-053. *ApJ*, 549:1135–1144, March 2001. Available from World Wide Web: http://adsabs.harvard.edu/abs/2001ApJ...549.1135C.

[86] J. E. Grindlay. The Bursting, Dipping, Precessing Ultra-Compact X-ray Binary X1916-05. In *Frontiers of X-ray Astronomy (Y. Tanaka and K. Koyama, eds.) Universal Academy Press (Tokyo), 69.*, 1992. Available from World Wide Web: http://adsabs.harvard.edu/abs/1992fxa..proc...69G.

[87] K. Yoshida, H. Inoue, K. Mitsuda, T. Dotani, and F. Makino. The Dipping Low-Mass X-Ray Binary X1916-05 Observed with GINGA. *PASJ*, 47:141–152, April 1995. Available from World Wide Web: http://adsabs.harvard.edu/abs/1995PASJ...47..141Y.

[88] A. Retter, Y. Chou, T. R. Bedding, and T. Naylor. Detection of negative superhumps in a low-mass X-ray binary - an end to the long debate on the nature of V1405 Aql (X1916-053). *MNRAS*, 330:L37–L42, February 2002. Available from World Wide Web: http://adsabs.harvard.edu/abs/2002MNRAS.330L..37R.

[89] W. C. Priedhorsky and J. Terrell. Long-term observations of X-ray sources - The Aquila-Serpens-Scutum region. *ApJ*, 280:661–670, May 1984. Avail-

able from World Wide Web: http://adsabs.harvard.edu/abs/1984ApJ...280..661P.

[90] D. K. Galloway, D. Chakrabarty, M. P. Muno, and P. Savov. Discovery of a 270 Hertz X-Ray Burst Oscillation in the X-Ray Dipper 4U 1916-053. *ApJl*, 549:L85–L88, March 2001. Available from World Wide Web: http://adsabs.harvard.edu/abs/2001ApJ...549L..85G.

[91] C.-P. Hu, Y. Chou, and Y.-Y. Chung. A Parameterization Study of the Properties of the X-Ray Dips in the Low-Mass X-Ray Binary X1916-053. *ApJ*, 680:1405–1411, June 2008. Available from World Wide Web: http://adsabs.harvard.edu/abs/2008ApJ...680.1405H.

[92] R. Iaria, T. Di Salvo, G. Lavagetto, N. R. Robba, and L. Burderi. Chandra Observation of the Persistent Emission from the Dipping Source XB 1916-053. *ApJ*, 647:1341–1348, August 2006. Available from World Wide Web: http://adsabs.harvard.edu/abs/2006ApJ...647.1341I.

[93] L. Boirin, A. N. Parmar, D. Barret, S. Paltani, and J. E. Grindlay. Discovery of X-ray absorption features from the dipping low-mass X-ray binary XB 1916-053 with XMM-Newton. *AA*, 418:1061–1072, May 2004. Available from World Wide Web: http://adsabs.harvard.edu/abs/2004A%26A...418.1061B.

[94] Z. Zhang, K. Makishima, S. Sakurai, M. Sasano, and K. Ono. Probing the accretion scheme of the dipping X-ray binary 4U 1915-05 with Suzaku. *PASJ*, 66:120, December 2014. Available from World Wide Web: http://adsabs.harvard.edu/abs/2014PASJ...66..120Z.

[95] M. van der Klis and J. M. Bonnet-Bidaud. The orbital parameters and the X-ray pulsation of VELA X-1 (4U 0900 - 40). *AAp*, 135:155–170, June 1984. Available from World Wide Web: http://adsabs.harvard.edu/abs/1984A%26A...135..155V.

[96] S. L. Shapiro and S. A. Teukolsky. *Black holes, white dwarfs, and neutron stars: The physics of compact objects*. 1983. Available from World Wide Web: http://adsabs.harvard.edu/abs/1983bhwd.book.....S.

[97] G. Nelemans, P. G. Jonker, and D. Steeghs. Optical spectroscopy of (candidate) ultracompact X-ray binaries: constraints on the composition of the donor stars. *MNRAS*, 370:255–262, July 2006. Available from World Wide Web: http://adsabs.harvard.edu/abs/2006MNRAS.370..255N.

[98] S. Rappaport, C. P. Ma, P. C. Joss, and L. A. Nelson. The evolutionary status of 4U 1820-30. *ApJ*, 322:842–851, November 1987. Available from World Wide Web: http://adsabs.harvard.edu/abs/1987ApJ...322..842R.

[99] S. Rappaport, P. C. Joss, and R. F. Webbink. The evolution of highly compact binary stellar systems. *ApJ*, 254:616–640, March 1982. Available from World Wide Web: http://adsabs.harvard.edu/abs/1982ApJ...254..616R.

[100] O. G. Benvenuto, M. A. De Vito, and J. E. Horvath. Evolutionary Trajectories of Ultracompact "Black Widow" Pulsars with Very Low Mass Companions. *ApJl*, 753:L33, July 2012. Available from World Wide Web: http://adsabs.harvard.edu/abs/2012ApJ...753L..33B.

[101] M. Bailes, S. D. Bates, V. Bhalerao, N. D. R. Bhat, M. Burgay, S. Burke-Spolaor, N. D'Amico, S. Johnston, M. J. Keith, M. Kramer, S. R. Kulkarni, L. Levin, A. G. Lyne, S. Milia, A. Possenti, L. Spitler, B. Stappers, and W. van Straten. Transformation of a Star into a Planet in a Millisecond Pulsar Binary. *Science*, 333:1717, September 2011. Available from World Wide Web: http://adsabs.harvard.edu/abs/2011Sci...333.1717B.

[102] L. Bildsten. Theory and observations of Type I X-Ray bursts from neutron stars. In S. S. Holt and W. W. Zhang, editors, *American Institute of Physics Conference Series*, volume 522 of *American Institute of Physics Conference Series*, pages 359–369, June 2000. Available from World Wide Web: http://adsabs.harvard.edu/abs/2000AIPC..522..359B.

[103] L. Burderi, A. Possenti, F. D'Antona, T. Di Salvo, M. Burgay, L. Stella, M. T. Menna, R. Iaria, S. Campana, and N. d'Amico. Where May Ultrafast Rotating Neutron Stars Be Hidden? *ApJl*, 560:L71–L74, October 2001. Available from World Wide Web: http://adsabs.harvard.edu/abs/2001ApJ...560L..71B.

[104] T. di Salvo, L. Burderi, A. Riggio, A. Papitto, and M. T. Menna. Orbital evolution of an accreting millisecond pulsar: witnessing the banquet of a hidden black widow? *MNRAS*, 389:1851–1857, October 2008. Available from World Wide Web: http://adsabs.harvard.edu/abs/2008MNRAS.389.1851D.

List of Figures

List of Tables

Acknowledgments

I would like to express my sincere, deep and everlasting gratitude to my supervisors Prof. Tiziana Di Salvo and Prof. Rosario Iaria. I would like to thank Prof. Luciano Burderi and Dr. A. D'Aì for the advice they gave me during these three years and for the interesting conversations on various topics. I also thank Dr. M.Matranga, who shared this adventure with me, and all the people who over these years have enriched with their presence the High Energy Astrophysics Group of the Università Degli Studi di Palermo. And finally I am extremely thankfull to all the people that, in different way, allowed me to reach this goal.